2016-01-01

Flame Front Structures Studies Of Highly Turbulent Reacting Flow Over A Backward Facing Step Using Khz Oh-Ch Planar Laser Induced Fluorescence

Arturo Acosta-Zamora
University of Texas at El Paso, aacosta29@miners.utep.edu

FLAME FRONT STRUCTURES STUDIES OF HIGHLY TURBULENT REACTING FLOW OVER A BACKWARD FACING STEP USING kHz OH-CH PLANAR LASER INDUCED FLUORESCENCE

ARTURO ACOSTA-ZAMORA

Doctoral Program in Mechanical Engineering

APPROVED:

Ahsan Choudhuri, Ph.D., Chair

Normal Love, Ph.D., Co-Chair

Evgeny Shafirovich, Ph.D.

Chunqiang Li, Ph. D.

Charles Ambler, Ph.D.
Dean of the Graduate School

Dedication

This work is dedicated to my parents, family, and friends who have supported me throughout my entire education

FLAME FRONT STRUCTURES STUDIES OF HIGHLY TURBULENT REACTING FLOW OVER A BACKWARD FACING STEP USING kHz OH-CH PLANAR LASER INDUCED FLUORESCENCE

by

ARTURO ACOSTA-ZAMORA, B.S., M.S.

DISSERTATION

Presented to the Faculty of the Graduate School of

The University of Texas at El Paso

in Partial Fulfillment

of the Requirements

for the Degree of

DOCTOR OF PHILOSOPHY

Department of Mechanical Engineering

THE UNIVERSITY OF TEXAS AT EL PASO

December 2016

Acknowledgements

I would like to thank the Army Research Office, ARO, for the financial support under award No. W911NF 13-1-0156 to enable the completion of this project. I would also like to express my gratitude to my supervisor, Dr. Ahsan Choudhuri of The University of Texas at El Paso, whose guidance and academic experience have been very important in the completion of this work.

Special recognition is also given to Mr. Scott Hill for his support with technical and safety expertise and guidance, as well as Gloria Salas and the rest of the cSETR staff. I would like to acknowledge particularly the contributions of Marco Quiroz, Arif Hossain, and Martin de la Torre, as they were crucial in the completion of this project as well.

Abstract

In recent years, there has been a greater move in the scientific and political community to increase combustion efficiency and reduce emission levels; for this reason, it is crucial to gain a better understanding of combustion. Experimental work at relevant conditions and the data generated from these is needed in order to gain a better understanding of combustion; this data may also be used for validation and further refinement of computational models and simulations. The improvement of optical combustion diagnostics systems has opened new ways to explore these combustion processes. The testing of a high intensity turbulence combustion system is presented in this work. The primary research objective of the project hereby discussed, was to study the structures of backward-facing step stabilized premixed flames in high turbulence flow, with the aid of KHz-level optical laser diagnosis technology.

Planar induced fluorescence experiments were conducted to visualize the flame front characteristics of the reacting flows under highly turbulent conditions over a backward facing step combustor. Air-methane premixed turbulent flames were studied at varying Reynolds numbers and flow turbulence intensity levels. An optically accessible combustion chamber was used to house premixed air-methane combustion at atmospheric pressure and stoichiometric conditions. OH-CH Planar Laser Induced Fluorescence (PLIF) was used to track the flame front location for the flames at the different Re and turbulence level conditions. Flows were tested at atmospheric pressure and temperature, and a constant equivalence ratio of 1 with the variation of flow length scales (L_T) and turbulence velocity fluctuations (u'). Flow length scales were varied through the use of turbulence generating grids of blockage ratios of 46% and 63% and hole diameters of 1.5 and 3 mm. Velocity fluctuations were varied through the increase of bulk flow rate resulting in Reynolds numbers, based on step height, ranging from 15000, 32000, and

64000. Turbulence parameters were measured at the combustor step, using Particle Image Velocimetry. These parameters including velocity fluctuations (u') and integral flow length scales (L_T) along with estimated flame parameters resulted in flames that are located well within the thin reaction zones of the Peters-modified Borghi diagram for premixed turbulent combustion. In summary, flames with $0.8 < Da < 34$, $0.8 < Ka < 95$, $3 < u'/SL < 72$, and u' values ranging from 1-27 m/s were tested.

Grid and Re effects on flame front characteristics were studied. A 10 kHz tunable PLIF system was used to map the flame front characteristics with a high temporal resolution and a spatial resolution of ~100 um/pixel. The high temporal resolution enabled the detection of the flame front characteristics in steps as low as 0.1 ms. OH-PLIF images revealed highly turbulent flames under the flow conditions, which were more noticeable with increasing Reynolds numbers. In general, flame fronts exhibited pockets of burned gases within the unburned gases, and vice versa. These burned gas pockets were seen to go through different processes including development on their own, separation form the main flame front core or branches of it, and eventual reattachment to the flame front.

CH-PLIF at 5kHz was attempted by optimizing the dye laser system for detection of the CH C-X band at 314 nm. The CH detection was difficult due to low laser pulse power, UV light scattering, and other effects, which affected the CH signal quality.

OH-PLIF images were used to estimate burning velocity ratios S_T/S_L and results for S_T/S_L ratios vs u'/S_L are presented. These showed that the ratio of s_T/s_L increases with increasing u'/s_L ratios.

Table of Contents

List of Tables

List of Figures

Chapter 1: Introduction

According to the International Energy Agency, a high percentage of total world energy - roughly ~82%, is generated by combustion. Energy generation is responsible for two-thirds of the greenhouse gas emissions and 80% of CO_2 [1]. This is expected to continue unless alternative and competitive energy sources are developed in the future. Thus, combustion will continue to be important in the energy sector in upcoming years.

In recent years, there has been a greater move in the scientific and political community to increase combustion efficiency and reduce emission levels; for this reason, it is crucial to gain a better understanding of combustion mechanisms and problems [2]. Since most practical combustion devices, such as rockets, jet engines, and gas turbines involve turbulent combustion; there is a need for a better understanding of turbulence and combustion as well as the relationship between them. In an effort to predict the behavior of the turbulent combustion processes, efforts have concentrated on the development of computational models. Computational models must solve the complex processes involved in turbulent combustion; yet at the same time, these models must be simplified to match current limiting computing capabilities.

Experimental work at relevant conditions and the data generated from these is needed in order to gain a better understanding of combustion; this data may also be used for validation and further refinement of computational models. [3] The development and improvement of high speed imaging technology (i.e. high speed cameras and high repetition rate lasers) has enabled the measurements of new experimental data. These developments have assisted the scientific community in the studying the fast time scales of turbulent combustion processes. The design and optimization of combustion devices depends on a better understanding of the fundamental processes at the relevant turbulent conditions of such devices. Thus, the work to be discussed here is an effort to generate experimental data at highly turbulent flame conditions and visualize the flame front characteristics with the aid of kHz laser diagnostic tools.

1. 1 Objectives

As it was just mentioned, the overall scope of the project is to study the flame front characteristics of turbulent premixed flames under near-compressible and high Reynolds numbers conditions with the use of high-speed laser diagnostics tools. The Center for Space Exploration Technology Research at the University of Texas at El Paso with support from the Army Research Office (ARO) developed an optically accessible combustion system to study turbulent premixed flames. The combustor uses a backward-facing step as the flame anchoring mechanism; further details are described in the Experimental Section of this dissertation. Former students at the Center began the system development and this work represents the first test series of the facility, which is complemented by 10 kHz Laser Induced Fluorescence and Particle Image Velocimetry systems.

As summarized by Sick [3], turbulent combustion studies should focus on addressing the following questions:

- Which regimes can be identified and where are the boundaries for each of them
- What is the instantaneous flame structure at each regime
- Can we characterize local properties of an instantaneous flame, if so, by which variables
- What parameters of the instantaneous flame can be used for a computational model

For this particular part of the project, the efforts are placed in addressing the following objectives:

- Generate experimental data at near compressible (M~0.3) and high Reynolds Numbers (Re > 10^3) conditions
- Reach the “thickened flame” flame regime conditions
- Map flame front structure at these conditions using kHz-level OH and CH PLIF
- Evaluate the change in flame front characteristics in response to flow field variations (length scale and Re)

Chapter 2: Background Theory and Literature Review

The following chapter will introduce relevant background theory, terminology, and previous work pertinent to the study in discussion. First the flow over a backward-facing step is introduced, followed by turbulent flow theory, then relevant laminar and turbulent premixed combustion theory is introduced, and finally the use of laser diagnostics in combustion is discussed.

2.1 Flow over a backward-facing step

A backward-facing step was chosen as the stabilization method for the flame inside of the combustor. The flow dynamics over a step is a problem that has been extensively studied in the fluid mechanics field. This technique creates a sudden area increase in the fluid flow path, resulting in a low velocity recirculation zone in the flow field right next to the step area. In addition to the recirculation zone, a boundary layer forms towards the end of the step, from which a shear layer is formed due to vortices that form at the edge of the step. In this particular case, the recirculation of hot gases downstream of the step anchors the flame at the edge of the step. This anchoring mechanism has a very simple geometry, and is a proven flame stabilization technique under different flow conditions.

Armaly et al [4] did a significant amount of work on flow through backward facing step, where a detailed analysis of flow behavior inside a backward facing step channel was conducted; additionally, a significant amount of work has been done by numerous researchers on the topic [5-7]. Piirto et al [8] carried out experimental 2D and 3D PIV measurement work on a square-channel backward facing step for Re=12,000, 21000, 55000 using water flow. They compared their results with DNS and RSM data having similar Re, which agreed well with each other.

Additional relevant initial work with combustion over a step and the use of optical combustion imaging has been conducted by Pitz and Daily [9], who used laser velocimetry to determine mean and rms values for a turbulent velocity field on reacting and non reacting flow. They also visualized the reacting flow through the use of Schlieren photography. Cohen et al

[10-12] looked into the characterization of combustion instabilities in a lean, premixed backward facing step combustor. They looked at instabilities introduced when they reduced equivalence ratio close to the blowout limits, and also pulsating flow effects on the velocity flow field behavior behind the step using laser velocimetry. Savelnikov et al [13] reported on the thermo-acoustic instabilities in backward facing step premixed flames in turbulent flow using 4kHz PIV and low repetition (4Hz) OH-PLIF. The low repetition rate limited their use of the LIF imaging, forcing them instead to focus on chemiluminescence imaging for flame front tracing. Figure 2.1 shows a typical diagram highlighting the major components of the flow over a backward-facing step as provided by Cohen [10].

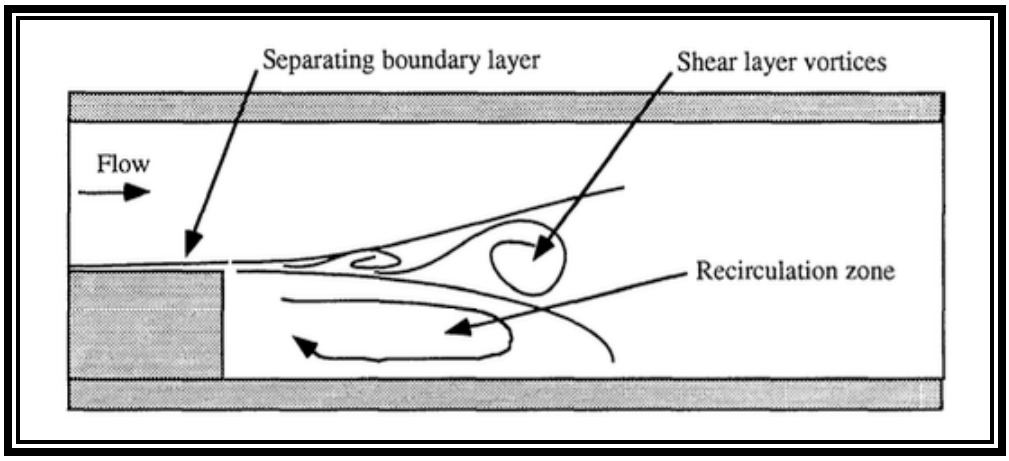

Figure 2.1: Flow over a backward facing step [10]

As seen in the diagram, a boundary layer forms as the flow approaches the step edge. Upon reaching the step edge, the flow encounters a sudden increase in area, which reduces the local flow velocity introducing a recirculation zone. A shear layer is then formed between the step boundary layer and the recirculation zone introduced by the step. This recirculation zone serves as the flame anchoring point at the step edge.

2.2 Turbulence

Turbulence in fluid mechanics is often referred to as “disorder” or “chaos” in a flow. Turbulent flow is often characterized by being “unsteady, irregular, chaotic and seemingly random” [14], to the point where even if boundary conditions are repeated, no identical flow may be reproduced. Nonetheless, averages of turbulent flow characteristics, such as mean flow velocity, are well defined. This means turbulent flows have a statistical description to them. It is important to understand some basic turbulence concepts as turbulence plays a part in combustion processes as well.

Osborne Reynolds first established the criteria to determine whether a flow is turbulent or laminar, by concluding that turbulence depended on the dimensionless Reynolds number. The Reynolds number is a ratio of the dynamic forces to the viscous forces in a flow and, for pipe flow, it is commonly described with the following equation:

$$\mathrm{Re} = \frac{VD}{\upsilon}$$

In the previous equation, V, D, and υ represent the flow speed, tube diameter, and kinematic viscosity respectively. The magnitude of the Reynolds number for a given flow condition and flow path geometry is used to determine whether a flow is turbulent or laminar. In general: for Re < 2000 flow is laminar, for 2000 < Re < 4000 the flow is considered to be in a transitional stage between laminar and turbulent flow, and lastly for Re > 4000 the flow is considered turbulent. A general representation of the flow field velocity at each of the flow classifications just mentioned is presented in Figure 2.2, where laminar is characterized by no velocity fluctuation, as the flow become turbulent these fluctuations become more evident. A lot of engineering applications involve turbulent flow conditions. In combustion, turbulence offers improved mixing which results in increased mass/heat transfer rates.

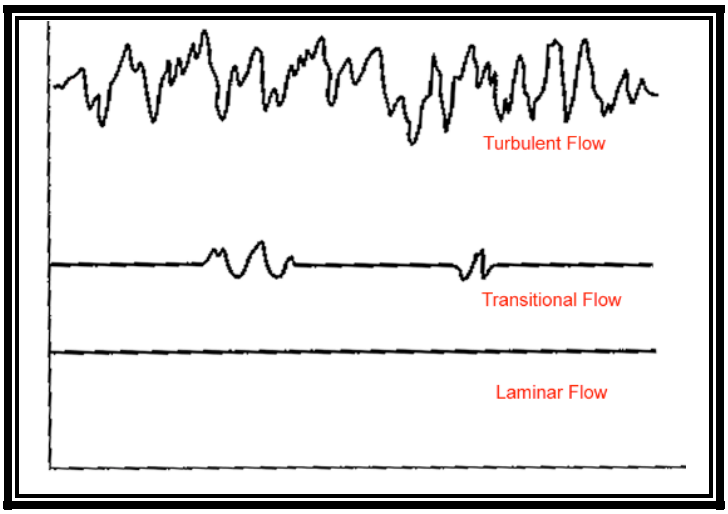

Figure 2.2: Velocity profiles for different flow conditions. Image: http://www.mit.edu/course/1/1.061/OldFiles/www/dream/SEVEN/SEVENTHEORY.PDF

2.2.1Turbulence Characterization

As mentioned before, even though there is a sense of chaotic behavior associated with turbulent flow, mean properties of turbulence are well defined. Thus, turbulence is often described using averaging techniques for flow parameters. When looking at Figure 2.1, one may notice the random variation of velocity at any given location in a flow; this velocity variation is caused by the turbulence eddies. Turbulent flow is characterized by a mean and fluctuating velocity components. If a specific point was selected within a turbulent flow, the velocity in the x – u(t) and y – v(t) directions would be described as follows:

$$u(t) = \overline{u} + u'(t)$$
$$v(t) = \overline{v} + v'(t)$$

where the barred u and v represent mean velocity values and u'(t) and v'(t) represent the velocity fluctuations around those mean values in the respective directions. This is illustrated in Figure 2.3.

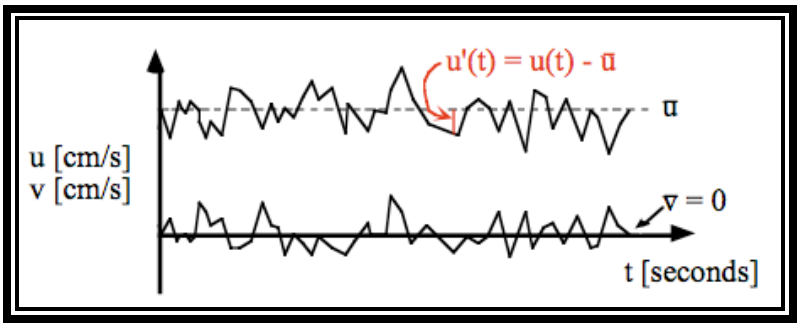

Figure 2.3: Reynolds decomposition of turbulent flow velocity. Image: http://www.mit.edu/course/1/1.061/OldFiles/www/dream/SEVEN/SEVENTHEORY.PDF

For turbulence studies, the parameter of interest is the velocity fluctuation term. The standard deviation of these fluctuations is known as root mean square (rms) of the velocity. This term is known as u_{rms} and represents the variation of the velocity at a specific point in a turbulent flow field. It may be described with the following formula:

$$u_{rms} = \left[\frac{1}{N} \sum_{i}^{N} (u'(t))^2 \right]^{1/2}$$

The magnitude of u_{rms} is indicative of the turbulence level in the flow field. This is illustrated in Figure 2.4, where two flow fields with the same mean flow velocity but different fluctuations are compared.

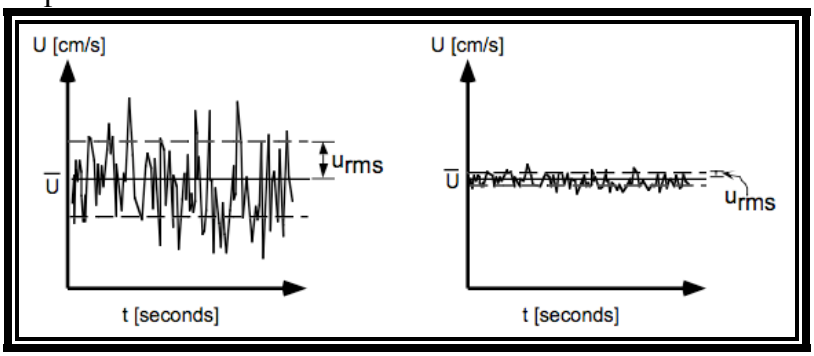

Figure 2.4: Comparison of u_{rms} for flow with identical flow velocities. Image: http://www.mit.edu/course/1/1.061/OldFiles/www/dream/SEVEN/SEVENTHEORY.PDF

The values of rms velocities along the three dimensions x, y, and z of any flow are a measure of the turbulent kinetic energy of a flow. If u_{rms}, v_{rms}, and w_{rms} represent the rms of the

velocity fluctuations in x, y, and z directions respectively, the relationship may be expressed as follows:

$$k = \frac{1}{2}(u_{rms}^2 + v_{rms}^2 + w_{rms}^2)$$

This relationship may be further derived by isotropic turbulence assumptions, where the fluctuating velocities are equal, or in the case where z direction fluctuations are considered to be equal to y fluctuations the equation then takes the following form:

$$k = \frac{3}{2}u'^2 = \frac{1}{2}(u_{rms}^2 + 2v_{rms}^2)$$

from which we can introduce the turbulence intensity term u' which represents the velocity variations in the flow field a given time:

$$u' = \sqrt{\frac{u_{rms}^2 + 2v_{rms}^2}{3}}$$

2.2.2 Turbulent Length Scales

A turbulent flow field is composed of eddies of varying sizes which correspond to different energy levels. Turbulence has several scales ranging from a macroscale (energy supply), to a microscale (energy dissipation). The energy possessed by eddies of different scales is passed from the larger ones to the smaller ones [14].

In general, three main length scales are used to describe turbulent flow (listed in order of largest to smallest turbulent scales: integral length scale (L_T), Taylor microscale (L_λ), and Kolmogorov scale (η). This means that eddies containing the most energy (i.e. largest eddies) in a flow are part of the integral length scale (L_T), while the smallest eddies correspond to the Kolmogorov scale (η).

The interaction between these scales is described according to Kolmogorov's energy cascade theory, which states that the energy is transferred from the larger eddies to smaller eddies in a process referred to as "energy cascade." Eventually the energy is dissipated by

viscosity and converted into heat. Flow behavior at the small-scale level is dependent on the energy dissipation rate (ε) and kinematic viscosity (*ν).* The Kolmogorov scale is then defined as:

$$\eta = \left(\frac{\nu^3}{\varepsilon}\right)^{\frac{1}{4}}$$

while the relationship between largest and smallest flow structures scales as:

$$\frac{L_T}{\eta} \sim \mathrm{Re}^{\frac{3}{4}}$$

2.2.3 Grid Generated Turbulence

In an experimental setup, there are different ways to influence the turbulence levels in the flow. One of the most common methods has been the use of a mesh, usually referred to as a grid, which can be used to induce turbulence in a flow. The grid creates homogenous turbulence, which decays over time [14]. Grid induced turbulence is known to have the following evolution: 1) transition stage into turbulent flow due to grid, 2) Fully developed turbulence (homogenous) and 3) finally the turbulence decay. Figure 2.5 shows the evolution of grid-induced turbulence, where the flow becomes hits the grid and achieves fully developed turbulence behind the grid. The main grid parameters influencing the turbulence level introduced in a flow include hole diameter and blockage ratio (ratio of blocked area to available flow area). For the study presented in this work, four different perforated plates of varying blockage ratio and hole diameters were used in order to increase the turbulence and the velocity fluctuation inside the combustion chamber.

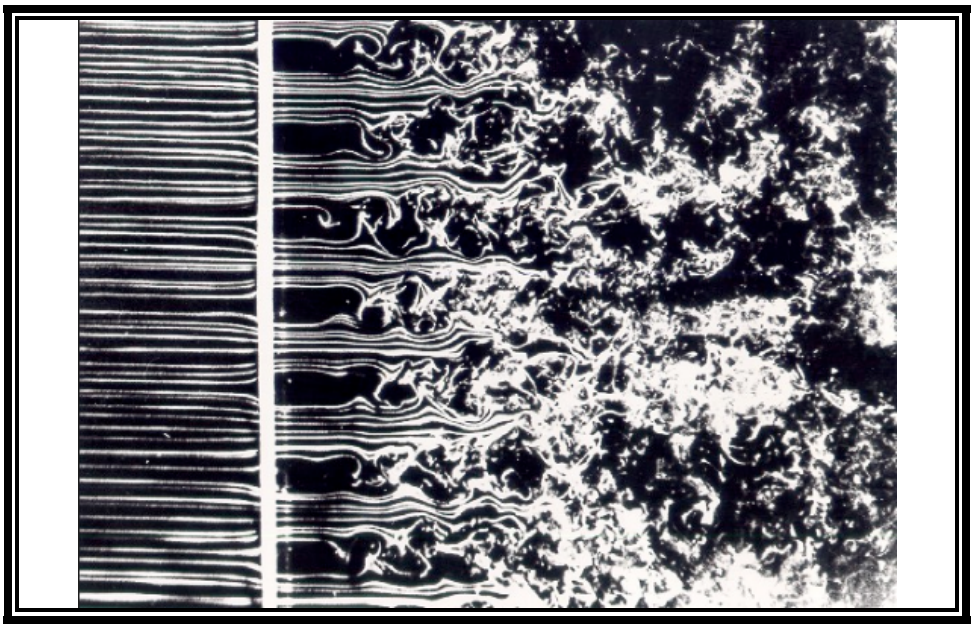

Figure 2.5: Instantaneous image of grid-induced turbulence (flow direction: left – right). Photograph: T. Corke and H. Nagib

2.3 Premixed Combustion

Combustion is generally described as the heat release that results from an exothermic reaction between an oxidizer and a fuel. A fuel can be considered as a resource of chemical energy that releases energy via chemical reactions. A flame on the other hand, is generally defined as a propagating combustion reaction process [15]. Once in existence, a flame releases heat, raising pressure and temperature of the surrounding mixture allowing the combustion to continue.

Flames are generally categorized as being premixed or non-premixed (diffusion) flames. When a fuel and oxidizer are mixed, partially or completely, prior to being ignited, the process is referred to as premixed combustion. In a diffusion flame, on the other hand, the reactants (fuel and oxidizer) are initially separated and reaction occurs at the interface between them [16]. The understanding of premixed combustion processes is important as engineering applications in practical devices work under these conditions.

2.3.1 Stoichiometry

The ratio of oxidizer and fuel quantities needed to have a complete reaction (completely burn the fuel) is referred to as stoichiometric ratio. In combustion processes occurring with an oxidizer amount greater than the stoichiometric amount, the mixture is referred to as lean. Similarly, is an oxidizer is present in a greater amount than the stoichiometric number; the mixture is referred to as fuel rich.

Stoichiometric ratios are determined by balancing idealized chemical reaction equations assuming complete combustion. Experiments for this study used premixed air-methane flames. For hydrocarbon fuels, such as the one used in this study –methane (CH_4), the equation for reaction with air may be expressed in the following form [16]:

$$C_xH_y + (x + \frac{y}{4})(O_2 + 3.76N_2) \rightarrow xCO_2 + (\frac{y}{2})H_2O + 3.76(x + \frac{y}{2})N_2$$

It is important to note that the general assumption for reactions with air, is an air composition of 79% oxygen and 21% nitrogen, hence the 3.76 factor. The chemical reaction of air +methane takes then the following form:

$$CH_4 + (O_2 + 3.76N_2) \rightarrow 2CO_2 + 2H_2O + 7.52N_2$$

The stoichiometric air to fuel ratio is defined as:

$$\left(\frac{A}{F}\right)_{stoic} = \frac{m_{air}}{m_{fuel}} = \frac{MW_{air}}{MW_{fuel}}$$

From the above formula air-methane stoichiometric ratio may be calculated to be 17.1. This ratio is useful when trying to determine whether a mixture is rich or lean. This is done through the estimation of the equivalence ratio, which is defined as follows:

$$\Phi = \frac{\left(\frac{A}{F}\right)_{stoic}}{\left(\frac{A}{F}\right)_{actual}}$$

This means, that an equivalence ratio of Φ=1 is indicative of stoichiometric conditions. For the study discussed in this dissertation, premixed air-methane flames at an equivalence ratio of 1 were used and this parameter was kept constant throughout all the experiments. However, it is important to note that interest also lies in the lean combustion ratios due to the potential emission reduction effects of working with these flames.

2.3.2 Laminar Premixed Combustion

The understanding of laminar-premixed flames is a requirement for the study and understanding of turbulent premixed flames as some turbulent combustion theories are derived from laminar theory. Laminar premixed flames have applications in devices such as heaters, burners, and other appliances.

A flame is typically divided into two zones: the preheat zone and the reaction zone. The former is an area where little heat release and consequently small temperature gradients occur; the latter is the area characterized by chemical energy release and high temperature gradients. A graphical representation of the laminar flame structure is presented in Figure 2.6. The reaction zone is divided into a narrow area of fast chemistry that is followed by a wider area of slow chemistry. It is the very thin area of fast chemistry that is of interest when studying flame structure. Fuel molecule breakdown and the creation of intermediate species occur in this fast-chemistry reaction zone. [16] In this thin zone, temperature and concentration gradients are large. This area is referred to as the laminar flame thickness (δ_L) and is of major interest for the study in flames. Laminar flame thicknesses for air-methane flames are typically in the order of <1mm.

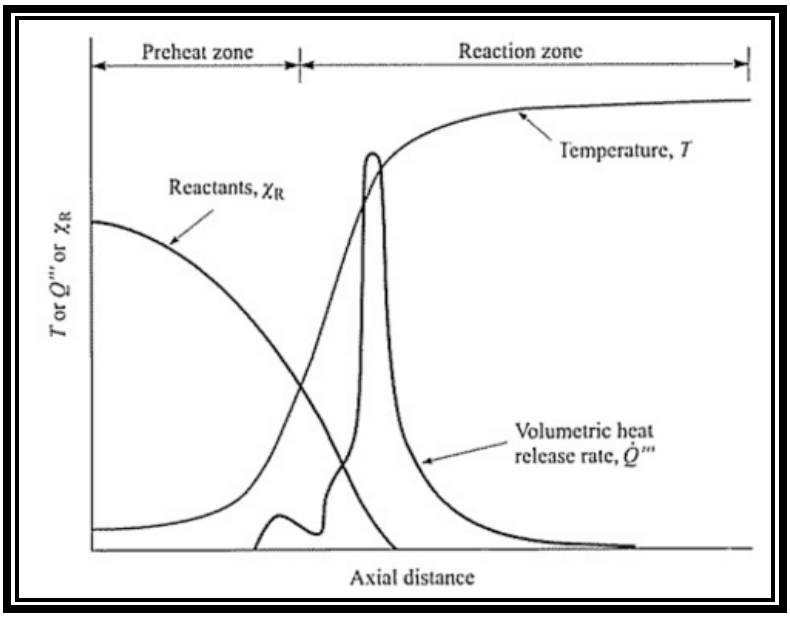

Figure 2.6: Laminar Flame Structure [61]

There are several ways of estimating the laminar flame thickness, mostly which use temperature gradients along the flame front. This however, requires a quantitative analysis of temperature profiles in the reaction zones. An alternative way to estimate laminar flame thickness was proposed by Zeldovich and may be used as reported by Siewert [18], which relates the thermal diffusivity of the mixture ($D_{mixture}$) and the flame speed (S_L) as follows:

$$\delta_L = \frac{D_{mixture}}{S_L}$$

This has introduced the second parameter of major importance when studying flames, the laminar flame speed or laminar burning velocity S_L. Both of these parameters δ_L and S_L have been shown to be a function of pressure, temperature, and fuel type/concentration. The current studies where conducted at atmospheric pressure and temperature, and mixture ratio was kept constant, thus laminar flame speed was taken to be 40 cm/s as reported by Law [19] at those conditions.

2.3.3 Combustion Radicals

As stated before, the reaction zone is characterized by the destruction of fuel molecules and the creation of many intermediate species. Methane (CH_4) and most hydrocarbons break down into OH, CH2O, HCO, and CH radicals. Figure 2.7 shows the concentration profiles for these radicals as a function of flame position and temperature rise.

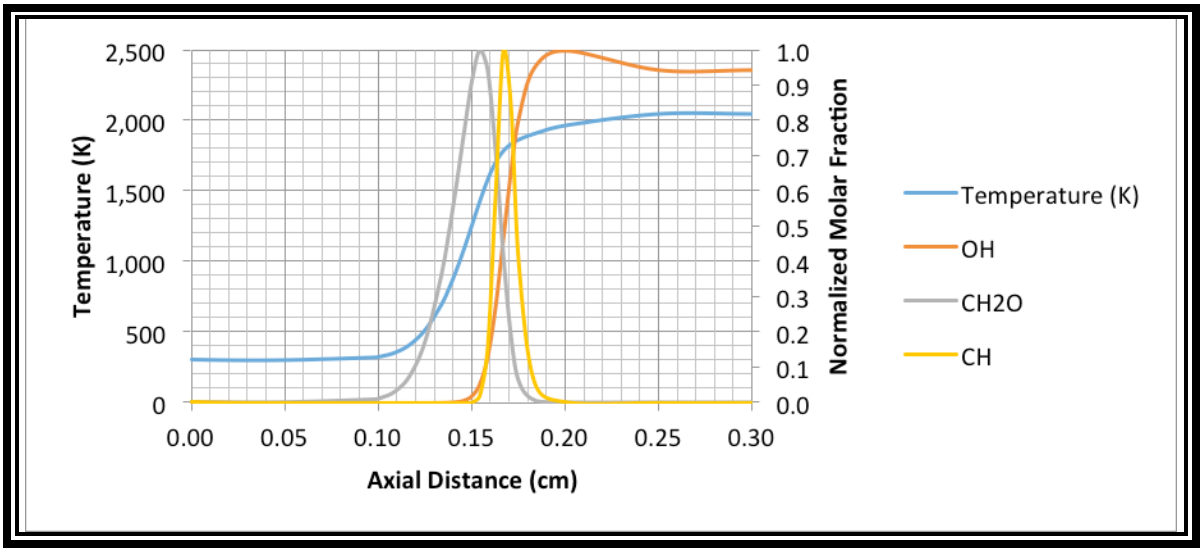

Figure 2.7: Combustion radical species concentration along laminar flame

HCO and CH are considered among the best flame front markers due to their presence in the high heat release rate zones of the flame. However, these radicals are have a short life as seen in Figure 2.7 and exist in very low concentrations. Out of these two CH would be considered the more common option, however the systems required for CH detection are not simple and have higher pulse power requirements. Vagelopoulos and Frank [20] conducted a numerical and experimental study to assess the adequacy of CH as a flame front tracer concluding experimentally that CH follows the heat release reasonably well for undiluted air/methane flames.

On the other hand, the OH and CH_2O radicals are more commonly used as flame front tracers due to their higher concentrations, which leads to a relatively simpler detection. OH shows high concentrations in the burned gas products; therefore it is a useful marker to separate

burned gases from the fresh unburned mixture. This does not imply that detection of these radicals is simple; in fact the systems required for the detection of these systems are sensitive and complicated, especially when talking about kHz levels, and will be discussed in following sections of this work. For now it is important to mention that OH and CH radicals were of interest for the current work.

2.3.4 Turbulent Premixed Combustion

Engineering applications of combustion processes are typically turbulent. Turbulence models are used to predict the behavior of turbulent premixed combustion processes. These models require experimental data for validation; hence the significance of experimental work in the area of turbulent premixed combustion. The laminar flame speed is mainly dependent on thermal/chemical properties of the gas mixture in use. On the other hand the turbulent flame speed depends on flow and mixture characteristics. [16]. In general turbulent flame speed is described by the following relationship, however there have been studies suggesting different relationships that attempt to fit experimental data.

$$S_T = \frac{\dot{m}}{A\rho_u}$$

2.3.5 Turbulent Combustion Dimensionless Parameters

The interactions between turbulence and the flame front are generally described by a set of dimensionless numbers, the most common being Damhkoler (Da), Karlovitz (Ka), and turbulent Reynolds number (Re_T). The Damkohler number represents whether a process is chemically or diffusively dominated. Da is generally described by the following equation:

$$Da = \frac{S_L L_T}{u' \delta_L}$$

For a given length scale, the Damkohler number should drop in value as turbulence intensity goes up. Karlovitz number relates the laminar flame thickness (δ_T) and the smallest turbulent length scale (η) of the flow and is described as follows:

$$Ka = \left(\frac{L_T}{\delta_L}\right)^{-1/2} \left(\frac{u'}{S_L}\right)^{3/2}$$

Lastly, the turbulent Reynolds number is a function of the pertinent length scale, in this case the integral length scale (L_T), velocity fluctuation (u'), laminar flame speed (S_L), and laminar flame thickness (δ_L) as follows:

$$\mathrm{Re}_T = \frac{u' L_T}{S_L \delta_L}$$

2.3.6 Classification of Turbulent Flames – Flame Regimes

These dimensionless turbulence parameters along with the flame parameters described before are used to classify flames. The most popular turbulent premixed flame classification system is known as the Borghi diagram. [21][22]. This diagram uses dimensionless ratios u'/ S_L and L_T / δ_L to classify flames; the Peters modified Borghi diagram is shown in Figure 2.8

Common flame regime classifications of interest are the corrugated flames, thin reaction zones, and well-stirred reactor regimes. The lines Re_T =1, Ka=1, u'/ S_L=1, and Ka=100 separate the different premixed combustion regimes. Laminar flame regimes fall below the line Re_T =1 (Re_T <1) and the turbulent flame regimes fall above the line at Re_T>1.

In the wrinkled flamelet regime the turbulence levels in are not representative of common engineering applications. The velocity fluctuation is not enough to have a significant effect on the flame front.

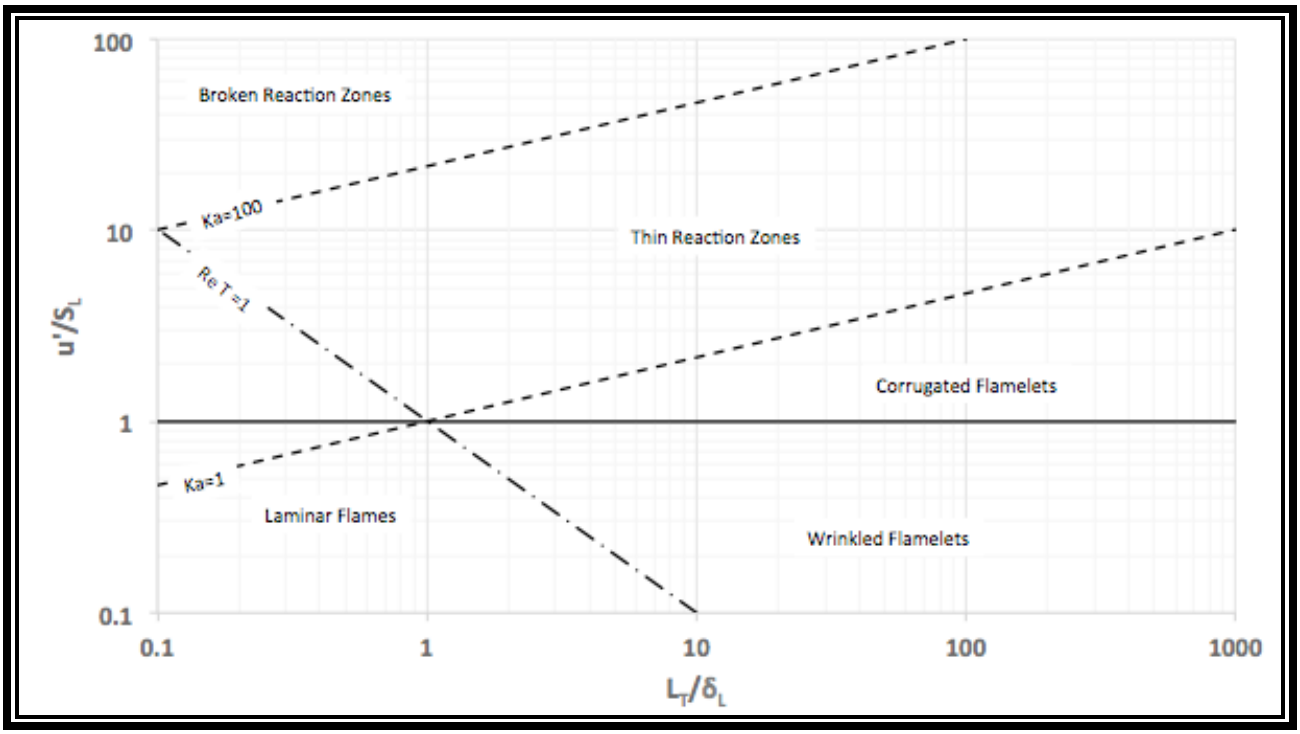

Figure 2.8: Peters-modified Borghi Diagram

The separation between the corrugated flames and thin reaction zones is determined by the Kilmov-Williams criterion which implies that the flame thickness is of the order or equal to the Kolmogorov scale. The thin reaction zone is believed to contain what some people refer to as the "thickened flames." When using the Borghi diagram to classify turbulent flames, the assumption is that premixed turbulent flames possess a similar structure to a stretched premixed flame [22]. The concept of thickened flames was first introduced by Zimont [23] suggesting small scale turbulence was capable of entering the flame front and, since then, researchers have not been able to validate or refute this theory through numerical simulations and experimental systems. In fact, there have been conflicting findings for flames reported to be approaching the thickened flame regime condition as Gulder noted [26]. Sankaran et al. [24] conducted a 3-D direct numerical simulation (DNS) of lean and turbulent methane/air flames in a Bunsen burner. They reported that at the mean thickness of the turbulent flame is greater than the corresponding laminar flame. Yuen and Gulder [25] used Rayleigh scattering and PIV to study methane-air and

propane-air flames in a Bunsen burner. Testing u'/S_L values from 3 to 24, corresponding to conditions of corrugated flamelets and thin reaction zones regimes, they reported that the flame front thickness increased with increasing turbulence rms velocity in both methane and propane flames. Tamadonfar and Gulder [26] again studied flame thickness of methane-air flames in a Bunsen burner at $0.6 < \phi < 1$and $4 < Ka < 21$. They reported thickening of the flame front with equivalence ratio increase. However they reported thinner thicknesses at increasing Ka. Other researchers have reported thinning of the flame front thickness as well, however at lower Ka number and turbulence intensity conditions than the current study [27]. As it may be seen from these results, the thickened flame regime is not well studied and experimental data at these flame conditions is lacking.

2.4 High Speed Imaging / Laser Diagnostics in Combustion

As it was stated in the introduction of the project, the recent developments in laser and camera technology enabled an increase in sampling rates by more than three orders of magnitude, enabling laser combustion diagnostics to help researchers around the world gain more knowledge of turbulent combustion processes. The work presented in references [3, 28, 29] provides an excellent overview of the evolution of the technology to as recently as 2013.

The need for high repetition rate measurements in turbulent flows stems from the time scales associated with combustion processes. [29] Reacting flows present an additional challenge as now you introduce the time scales associated with chemical reactions. Turbulence is characterized by variations in space ant time, simultaneous measurements of flow and flame properties will be needed. [28] The understanding of fundamental combustion processes must be improved in order to generate suitable models to predict turbulent flames behavior under different conditions.

For combustion studies, laser diagnostic techniques possess the advantage of being non-intrusive techniques, meaning that the flow is not disrupted. This is done by utilizing laser light to either track naturally occurring combustion species or seeding non-reacting “tracers” in your

flow. The most common combustion diagnostic techniques include Laser Doppler Velocimetry (LDV), Particle Image Velocimetry (PIV), Rayleigh scattering, Raman scattering, and Planar Laser Induced Fluorescence (PLIF). PIV and PLIF have benefited from these technology developments making them capable of reaching temporal resolutions of the kHz level, and are the methods utilized to study turbulent combustion processes in this work. It is important to note that both of these technologies require optical access to the combustion process being studied.

2.4.1 Particle Image Velocimetry (PIV)

PIV is one of the most common measurement techniques used in fluid dynamics. PIV tracks the displacement of seeding particles in the flow to determine the local fluid velocity. This is done by taking consecutive images and running cross-correlation algorithms. kHz level measurements allow for higher temporal resolution. This technique is limited by laser pulsing frequencies and high-speed camera resolution. In the future, MHz-level PIV measurements may be possible with new cameras being developed with higher resolutions at high frame rates [29].

A typical Particle Image Velocimetry system usually consists of three main components: 1) Flow tracer particles, 2) Light source, and 3) High speed imaging system. Flow tracer particles are introduced into a flow, the light source is formed into a sheet through the appropriate optics and shone at the flow, and finally a high-speed camera, placed in perpendicularly to the laser sheet, captures the light scattering of the laser on the particles.

PIV uses seeding particle displacement over a particular time lapse Δt, to determine the particle velocity inside the flow. The success of the PIV imaging is dependent on the particles following the fluid behavior accurately [30]. Thus, some people argue that PIV track particle velocity as opposed to flow velocity, but accurate velocity measurements have been obtained by numerous researchers used this technique. A graphical representation of the technique is presented in Figure 2.9 as provided in [30]

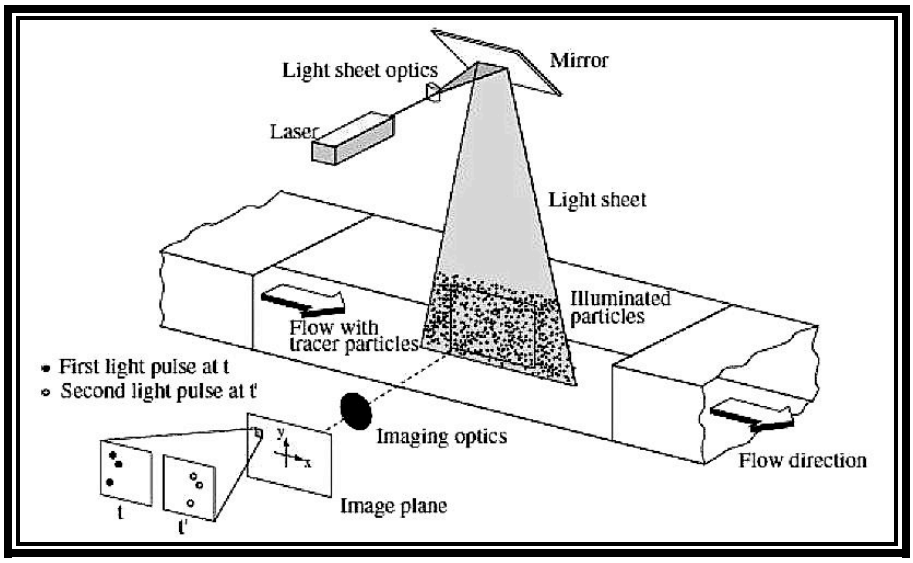

Figure 2.9: General PIV System Arrangement [30]

2.4.2 Laser Induced Fluorescence (LIF)

Laser Induced Fluorescence (LIF) is one of the most common spectroscopic techniques used for flame front detection. A light source, usually a laser, is used to excite a molecular species; this light source is resonant with a specific molecular transition state for a particular species. In other words, the molecules of combustion species are excited to a higher energy level due to the absorption of the laser light, upon relaxation a fluorescence emission results; this emission may be captured by a high-speed camera.

Figure 2.10 shows the molecular energy levels that are involved during LIF measurements. The light source (laser beam) is set to an energy level that is located between the ground state and the excited state of the species molecule. Once in the upper state, the excited species may relax to the lower states (identified by levels 1,2,3 in Figure 2.10) while emitting photons in the form of fluorescence [31]. Any given species may also give up the energy through dissociation or collisional quenching, in which case the molecules does not participate in the fluorescence process, as shown in the diagram. These losses become of major importance when interest lies in quantitative data gathering from the LIF signal (i.e. density, temperature, etc.) However, in the case of this study, qualitative LIF data describing the location and shape of the

flame front is the main interest. Once emitted, only a few photons can be captured for analysis by the detection system. A typical LIF detection system usually consists of a high-speed digital camera coupled with a gated light intensifier unit and a filter.

From the excited state, a molecule may return to its ground state while emitting a photon at the same wavelength as the excitation. These bands are generally referred to as diagonal bands. In this case, however, scattering processes interfere with detection. Bandpass filters are generally used such that a specific wavelength can be detected while the detection of the other transitions is blocked.

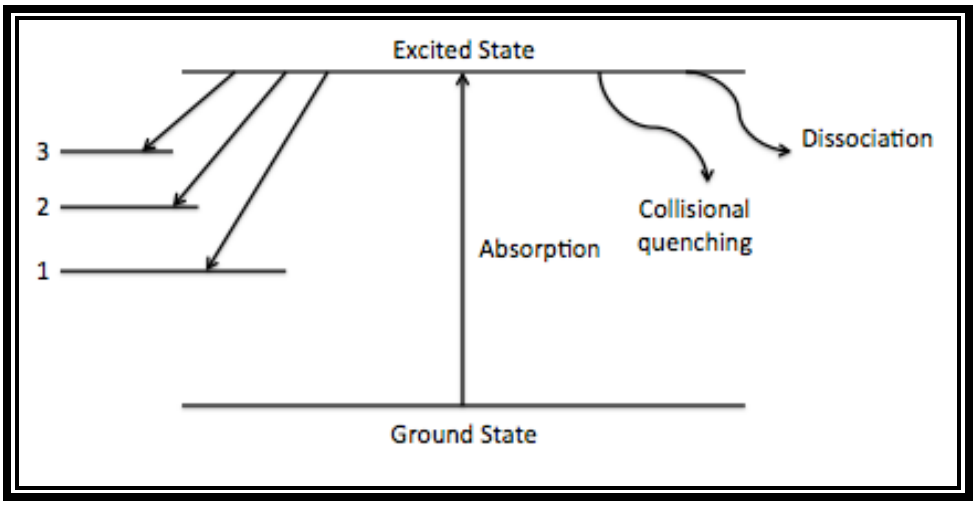

Figure 2.10: Energy transfer from an excited state [31]

LIF presents unique advantages when compared to other absorption spectroscopy techniques. Fluorescence may be collected for a user-selected volume, which translates into the possibility of having single-point or multiple-point measurements by using a laser point or a laser sheet respectively. This non-intrusive technique takes advantage of the naturally occurring combustion species described before such as O2, OH, NO, CH2O, and CH among others, making it a suitable diagnostics tool for the high temperature and high-speed flows associated with combustion. The most common species used for LIF measurements and their respective absorption wavelengths are presented in Table 2.1.

Table 2. 1: LIF detection wavelength of different species.

Molecule	Absolute wavelength (nm)
OH	306
CH	431
CN	388
NH	336
NO	226
CH_2O	320-360

There are downsides, however, to the use of this technology. Due to the selective nature of the excitation process, LIF measurements are limited to particular species measurements. This means that if multiple species are of interest, then multiple laser and camera systems must be used to make such measurements. Low pulse energies also become a major limiting factor, especially as the laser trigger rates reach the kHz level, such as in this experiments. Lower repetition rates will result in high pulse energy, but a drastically reduced time resolution for the measurement. Even when laser is not a limiting factor, fluorescence emission still remains a function of species concentration, which makes certain species detection a difficult task. Difficulties with the detection of the fluorescence continue with the addition of background noise and radiation. Even though band pass filters are used to mitigate noise, sometimes background radiation may be coincident with the LIF signal, thus making it through the filter. Since both the laser pulse and the LIF emission are fast processes, they must be correctly synchronized to happen simultaneously. Hence, the detection has to be gated and synchronized correctly with the laser pulse, especially when LIF signal is being detected from hot gases, as natural flame chemiluminescence may overwhelm the signal. At the same time though, the detection system itself may generate noise that interferes with the signal, especially when intensifying the emitted light. [31]

2.4.3 OH-PLIF

In combustion research, the LIF signal is used to trace the flame front, as it was mentioned before. Hydrocarbon breakdown occurs at the flame front, which is the area of maximum energy release. It was mentioned in previous sections of this work, that OH, CH2O, and CH are among the most widely used flame front tracers.

The OH radical is widely used for the flame front tracer as it provides the largest amount of fluorescence signal. Dyer and Crosley first reported OH detection method for 2D visualization of OH in a naturally occurring flame [32]. Typical OH PLIF detection systems use a high energy pump laser to pump a dye laser which may be tuned, through frequency doubling, to the most commonly used excitation band of 283nm UV output.

It was discussed in previous chapters that OH has a long life and is present in the burned gases. Therefore, this radical may be used to separate the unburned mixture and the burned gases. Most PLIF studies are conducted in burners, which reduces many complexities such as background scattering/noise and power losses through windows, etc. OH detection in enclosed setups has been demonstrated as shown in [13] and [33], where low repetition OH LIF was conducted in optically accessible combustors. OH PLIF has also been used more recently as a means for estimation of 3D flame surfaces for premixed flames as sown in [34] and [35].

Some researchers have considered OH an acceptable flame thickness tracer for flames at low Reynolds numbers; however for high Reynolds number conditions, it is possible that the edge of the OH radicals may not represent flame front locations accurately [36]. Therefore OH is not considered a reliable indicator of the heat release and “exact” flame front location.

2.4.4 CH-PLIF

In order to identify the actual location of the flame front, other radicals such as the CH radical have been used. It was mentioned before that Vagelopoulos and Frank [20] assessed the adequacy of CH as a flame front tracer concluding experimentally that the heat release zones coincide reasonably well with the CH concentration. CH tracing is much more difficult due to

the lower concentrations of the radical, however given the fact that it is produced in the flame front and has a narrow width, CH PLIF measurements have been used to investigate flame front characteristics. CH layer measurements of <1mm have been reported for turbulent flames [37].

CH PLIF measurements have been reported with different types of experimental setups. The most common detection schemes involve the use of the A-X ~430 nm and B-X ~390 nm excitation wavelengths. Lee et al. demonstrated the development and use of an Alexandrite laser system for single shot investigation of turbulent flames [38][39]. Yiang et al. and Miller et. Al have demonstrated the use of an optical parametric oscillator based system for CH detection [40][41]. Most recently, Jochi et al demonstrated the use of a single pump YAG laser used to pump separate dye lasers for multi species detection [42].

A recent approach taken for CH detection was that demonstrated by Carter et al [43][44], who demonstrated successful detection of CH using the C-X ~314 nm band. This band had been reported since 1959 by Gero and Moore [45], however it was not used in combustion research applications until now due to the overlapping with OH absorption bands at those wavelengths. In fact, the only reported groups to have used this band aside from the recently mentioned group of Carter, as far as the author knows where Chou and Dean [46] and Tsijishida et al. who visualized CH at this band with a single-shot laser [47]. Jeffries et al reported on the use of LIF for multiple species detection in flames, where they discuss the difficulties with this band. Since the diagonal bands are the strongest, most of the fluorescence returns at near the excitation wavelength. OH transitions overlap with non-diagonal bands, which have only 1% the intensity of diagonal bands. They claimed that the C-X band has a better efficiency even with its shorter lifetime when compared to A-X and B-X bands [48]. Table 2.2 summarizes the coincident excitation wavelengths for different species as reported in [48].

Table 2. 2: Coincident excitation wavelengths [48]

Excitation Wavelength	Radical Species	Transition			Energy[a] cm^{-1}
334.09	NH	A-X	(0,0)	$R_3(4)$	29932.71
	CN	B-X	unknown	$\Delta v=2$	—
315.10	OH	A-X	(0,0)	$P_1(13)$	31726.79
	NCO	B-X	000-000	unknown	—
314.85	OH	A-X	(1,1)	$Q_2(5)$	31752.72
	NH	A-X	(2,1)	$P(17)$	—
	NCO	B-X	000-000	R_1 head	—
314.66	OH	A-X	(1,1)	Q_2 head	—
	NH	A-X	(1,0)	$P(22)$	—
314.38	OH	A-X	(0,0)	$P_1(12)$	31799.49
	CH	C-X	(0,0)	$Q_2(10)$	31799.4
				$Q_1(11)$	31799.6
312.22	OH	A-X	(0,0)	$Q_2'(15)$[b]	32019.34
			(1,1)	$R_1(6)$	
	NH	A-X	(2,1)	$P_1(12)$	32019.38
	CH	C-X	(0,0)	$R_1(7)$	32019.32
	CN	B-X	unknown	$\Delta v=3$	—

2.4.5 Simultaneous detection and kHz applications

So far, the discussion of PIV and LIF as independent systems has been covered, and most of the referenced work was at low repetition rate (Hz level) especially for the LIF work. The technological advancements have also allowed the use of simultaneous detection. In combustion, this simultaneous use of these two laser technologies allows them to complement each other. PIV provides velocity vector maps of the flow field, while LIF can track the flame front development in response to flow behavior.

Tanahashi et al. reported the use of low repetition (Hz level) CH-OH and stereoscopic PIV measurements in methane-air turbulent premixed flames in the corrugated flame regime with $3 < u'/S_L < 5$ [49][50]. Filtayev et al reported the use of stereoscopic PIV and double pulse PLIF to study of stoichiometric-air flames at relatively high Reynolds numbers, where they saw a strong interaction between the flame front and vortex structures [51]. Simultaneous visualization of multiple species has also been conducted, as reported in [52].

High repetition studies, where “high repetition” is mostly considered to be of trigger rates >1kHz, are far scarcer. Even though technology development has enabled these types of studies, the equipment required (lasers, cameras, etc) is still expensive, making these studies more difficult to come by. Boxx et al. studied the feasibility of acquiring simultaneous PIV/OH-PLIF

measurements at multi-kHz rates (3kHz) in a turbulent swirl natural gas flame at pressures relevant to modern industrial gas turbine combustors [53]. Slabaugh reported the use of 5kHz PIV/OH-PLIF for the study of turbulent combustion in conditions relevant to combustion engines [54]. Elbaz and Roberts reported the use of 10 kHz OH/PLIF and stereo PIV for the analysis of inverse diffusion flames. [55].

In conclusion, studies with PIV and PLIF at kHz level are scarce, even scarcer at high turbulence intensity flames. The literature review shows that for the most part Bunsen burner or swirl-stabilized burners have been used with low repetition PLIF systems. The added temporal resolution of the 10kHz systems used in this work allow not only for the tracking/solving of velocity vectors inside the combustor, but also for the tracking of the flame front at much shorter intervals than those available in literature. The use of these technologies at the highly turbulent conditions in this study has not been demonstrated in optically accessible combustors or burners.

Chapter 3: Experimental Setup and Methodology

The following chapter will describe the experimental facilities and methodology utilized for the completion of the experimental runs at the Center for Space Exploration Technology Research's Goddard laboratory.

3.1 Experimental Setup Description

The work conducted during the design and development of the experimental setup used is described in thorough detail in the work of Quiroz [56] and Hossain [57]. For this discussion, only a description of the setup that was utilized, the relevant operating parameters, and methodology followed during the experimental runs is provided. For more detailed reference on the design of the facility refer to the sources previously mentioned.

Table 3.1 breaks down the facility into the primary subsystems listed on the first column. Each subsystem is briefly described in the corresponding row in the right hand column. As it has already been stated, the system was operated with air and methane as reactants for the turbulent premixed flames, in order to study combustion at compressible flow rates and high Reynolds numbers. The combustor, reactant delivery lines, pilot flame subsystem, exhaust cooling, high speed laser diagnostics, and the controls systems used to acquire data from instrumentation, control system valves, and trigger the laser systems will be discussed in the following sections of this chapter.

Table 3.1: Experimental setup subsystem breakdown.

Subsystem	Function
Combustor	Provides optical access in order to employ flow diagnostic techniques
Chamber cooling	Cools the combustor in order to prolong combustion run time for up to 13 minutes
Main air line	Provides cold/preheated air to the combustor for premixed flame combustion
Pilot flame	Ignition source for the air and methane reactants inside the combustion chamber
Methane line	Provides methane to the combustor for premixed flame combustion
Exhaust	An exhaust which serves as an escape which cools the hot combustion products to a safe and acceptable temperature
Control system	Provides control of system instrumentation
PIV system	Laser diagnostics system used in the present work to characterize the turbulence scales of air at compressible conditions
PLIF system	Laser diagnostics system that allows the analysis of flame front characteristics.

3.1.1 Combustor

The 304 SS combustion chamber housed the combustion processes during the experimental runs. The combustor has optical access through quartz windows located on the top and both lateral sides. The 1" quartz windows provide access for the high-speed laser diagnostics laser sheets and also provide viewing points for flame visualization through the use of high-speed cameras. These windows were designed with a factor of safety (FOS) =3.5 for combustor maximum operating conditions of: maximum chamber pressure of 6 bar (90 psi) and maximum temperature of 500K (440 F).

Prior to entering the combustor, air and methane flow through the mixing chamber, which consists of an axial air injection and tangential methane injection ports. The flammable mixture is then introduced to combustor through the inlet transition flange, which transitions the tubular flow path into the square cross-section flow path found inside of the combustor. Once

inside the combustor, the mixture encounters the backward-facing step, which provides a sudden flow path area expansion. This expansion ratio of 1:2 inside of the chamber results in a low-velocity recirculation zone and a shear layer formation at the edge of the step as described in the Background Theory section of this dissertation. The step height may be varied due to the fact that the step is part of a modular independent piece in the combustor assembly, which may be changed if step height effects are to be studied or if different reattachment lengths are desired.

The air-methane mixture ignition point is at the recirculation zone occurring downstream of the step. The pilot flame subsystem ignites a high flame speed hydrogen-air flame, which is used to ignite the flammable mixture inside the combustor. After ignition, the reaction products are routed to the exhaust cooling tower before being directed to the laboratory exhaust by the exhaust fan. An exploded view of the combustor assembly is presented in Figure 3.1. The cross-sectional view of the same assembly is shown in Figure 3.2. The combustor has cooling channels running along the length of the combustor, through which water is routed to cool the combustor at maximum operating conditions; hot water temperature is then reduced by a heat exchanger.

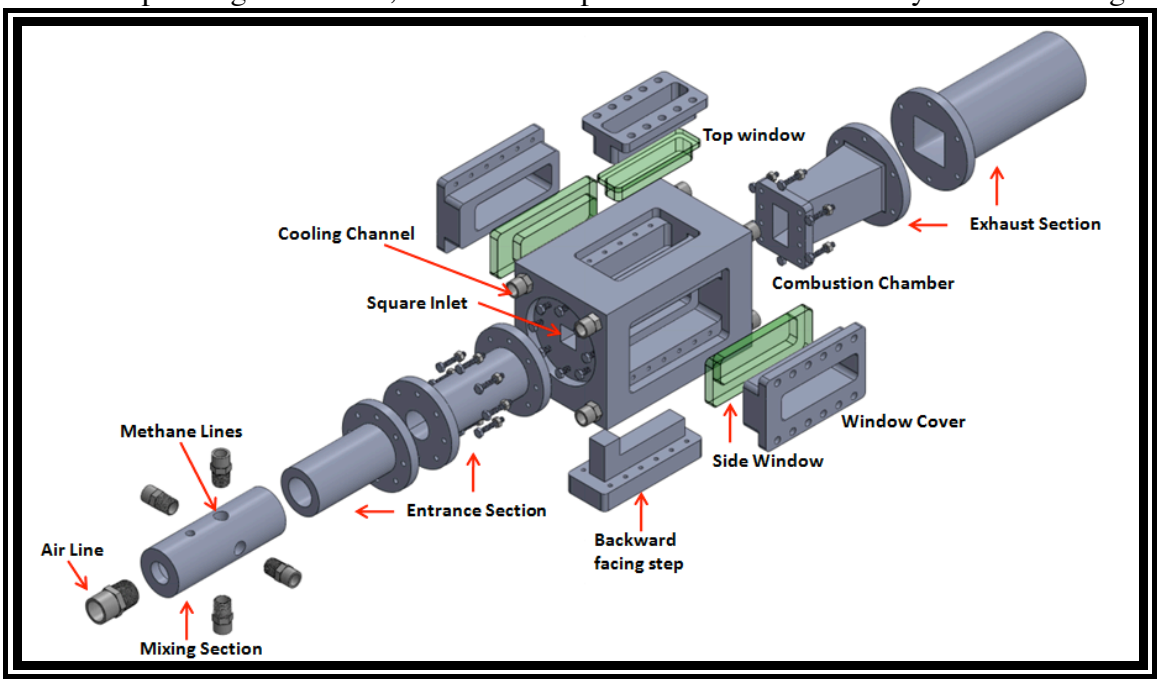

Figure 3.1: Exploded CAD model of combustor assembly (flow direction: left – right)

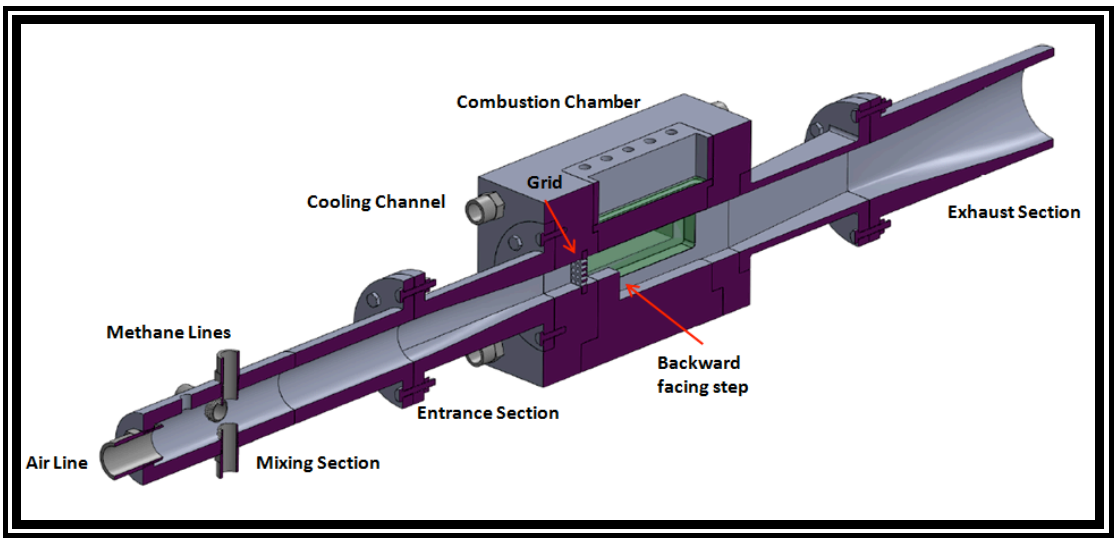

Figure 3.2: Cross-sectional view of the combustor assembly (flow direction: left – right)

From the cross-sectional view, one can note the flow path, as well as the turbulence generator (labeled as grid in the Figure) at the combustor entrance. Isotropic turbulence is generated through the use of a perforated plate, or grid. Different grids of different diameter and were used to change the length scale of the flow. Blockage ratios of 46% and 63% were selected, each with hole diameters of 1.5 mm and 3mm, thus a total of four different perforated plates were tested; these are summarized in Table 3.2.

Table 3. 2: Summary of grid blockage ratio and hole diameter.

Blockage ratio (BR)	**46%**	**63%**
Hole diameter 1 (mm)	1.5	1.5
Hole diameter 2 (mm)	3	3

These grids were machined from aluminum 6061, as they were not expected to be in contact with the flame or combusting gases during continuous operation, and placed ten maximum diameter lengths upstream of the combustor entrance to allow for fully developed turbulence at the edge of the step prior to ignition. These grids also serve the purpose of a

flashback arrestor due to the hole diameter sizes utilized. The following image shows the grids used for the experimental runs.

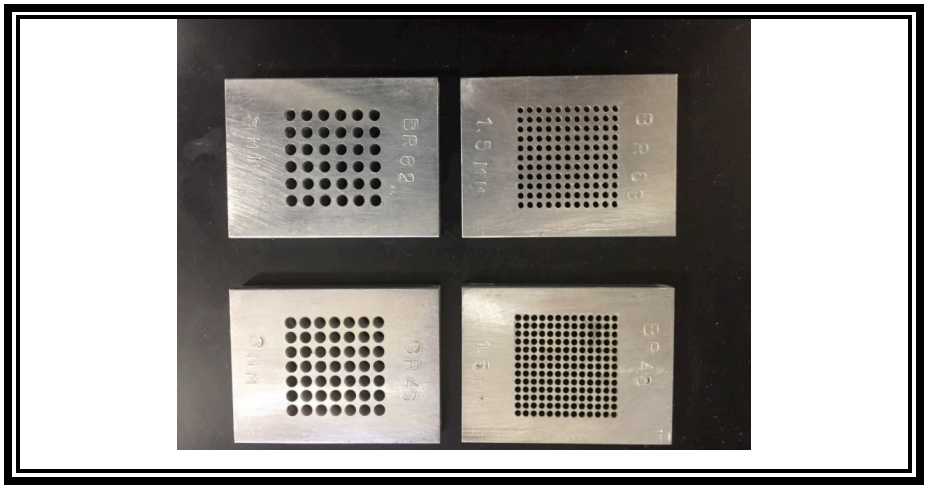

Figure 3.3: Turbulence generating grids

3.1.2 Air and Methane Delivery Lines

A designated compressor, with flow capacity of up to 190 cfm at 140 psig, supplies air to the delivery lines. The air goes through an industrial dryer followed by a filter to avoid particles, humidity, or compressor oil presence in the air. Air is set to the desired pressure through the use of a high flow regulator and a flow control valve. On the other hand, ultra high purity (UHP) methane is supplied through 4 laboratory k-bottles connected in to a single manifold. ½" and 1" 316 SS tubing lines deliver methane and air respectively to the mixing chamber. Each line is equipped with a set of control valves, pressure transducers to monitor pressure in the lines, thermocouples, and flow meters. Figure 3.3 and Figure 3.4 show the flow schematic for the experimental setup as well as the corresponding legend for the schematic respectively.

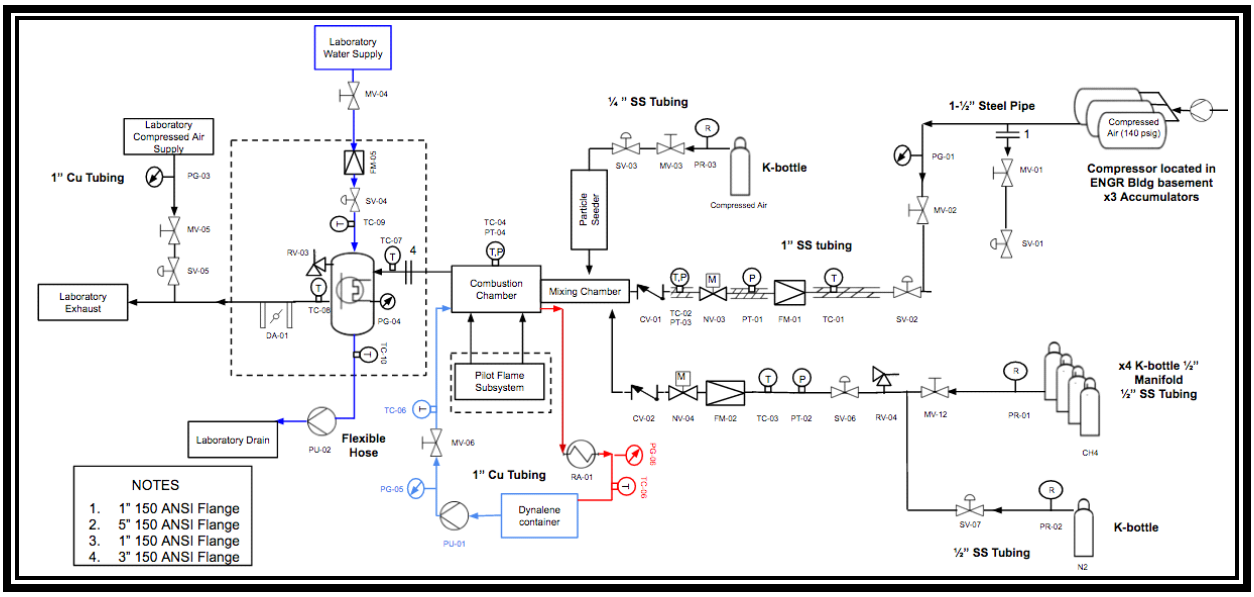

Figure 3.3: Experimental setup flow schematic

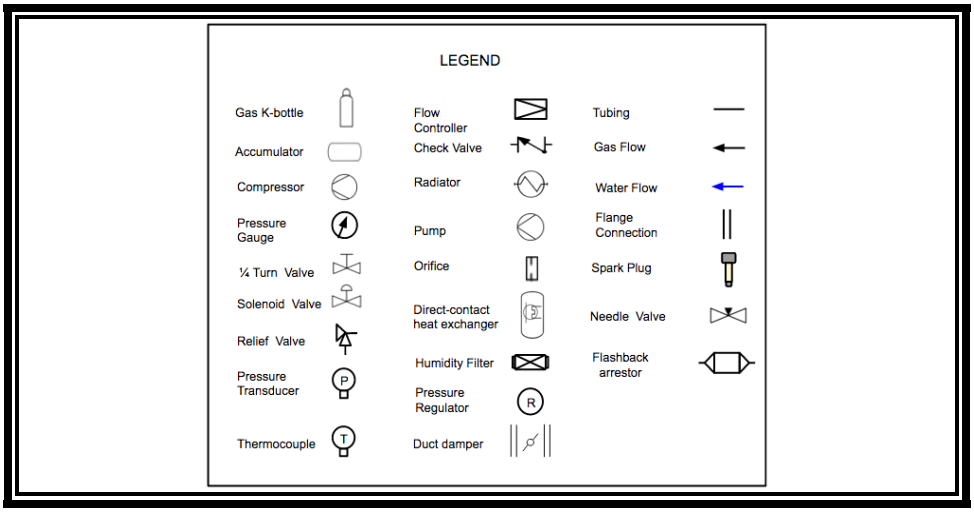

Figure 3.4: Flow schematic symbol legend

3.1.3 Pilot Flame

As stated before, a hydrogen-air premixed flame ignites the methane-air mixture inside the combustion chamber. This pilot flame reactants were chosen due to the high flame speed possessed by hydrogen premixed flames. The pilot flame is positioned within the recirculation zone right downstream of the step to take advantage of the low velocity flow. It is located perpendicular to the main flow, which is at least two orders of magnitude greater for the lowest

flow condition, hence the desirability for a pilot flame with a high flame speed to avoid pilot blowout by the main flow. The pilot flame flow rates are increased as bulk flow rates are increased with increasing Reynolds number conditions. The location of the pilot flame is presented in a 1-D cross-sectional view of the combustion chamber flow path in Figure 3.5.

The pilot flame gases are supplied through laboratory K-bottles, which provide UHP air and hydrogen. The delivery lines are made out of ¼" OD tubing equipped with control valves and pressure/temperature instrumentation. These delivery lines are routed/placed underneath the main flow delivery lines in a supporting stand. Air and hydrogen get introduced into a mixing chamber, which feeds the ignition chamber. The ignition chamber holds a common car spark plug, which serves as the ignition source. The spark plug electrode was extended such that the spark plug arcs to the combustor step wall. The ignition power comes from an LS2 MSD car ignition coil outputting 60 kV. The ignition coil and corresponding connection pin out is presented in Figure 3.6

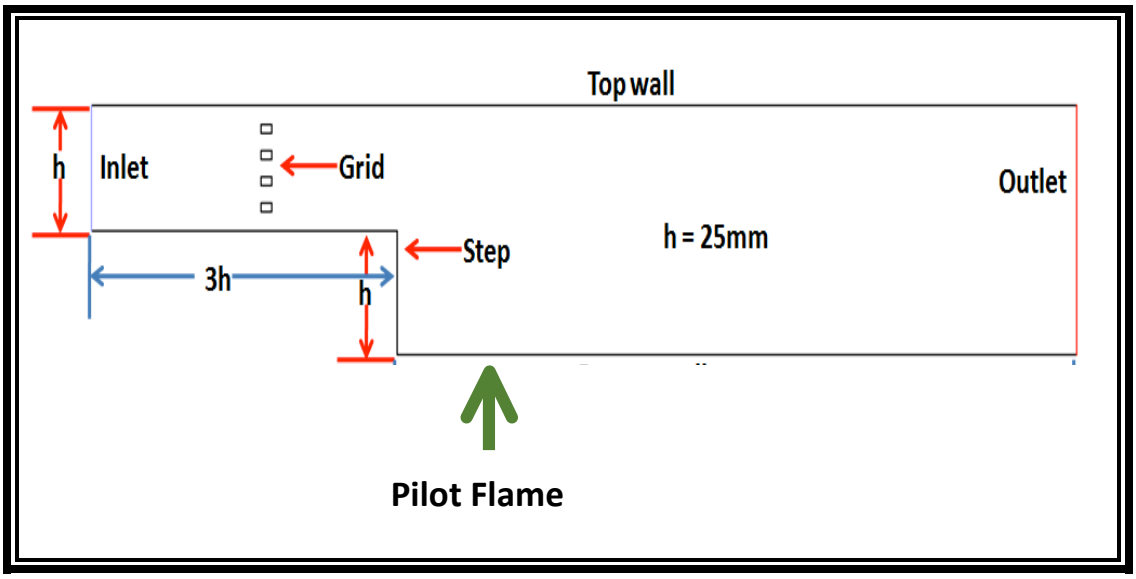

Figure 3.5: Combustor flow path cross-sectional view showing pilot flame location (flow direction: left – right)

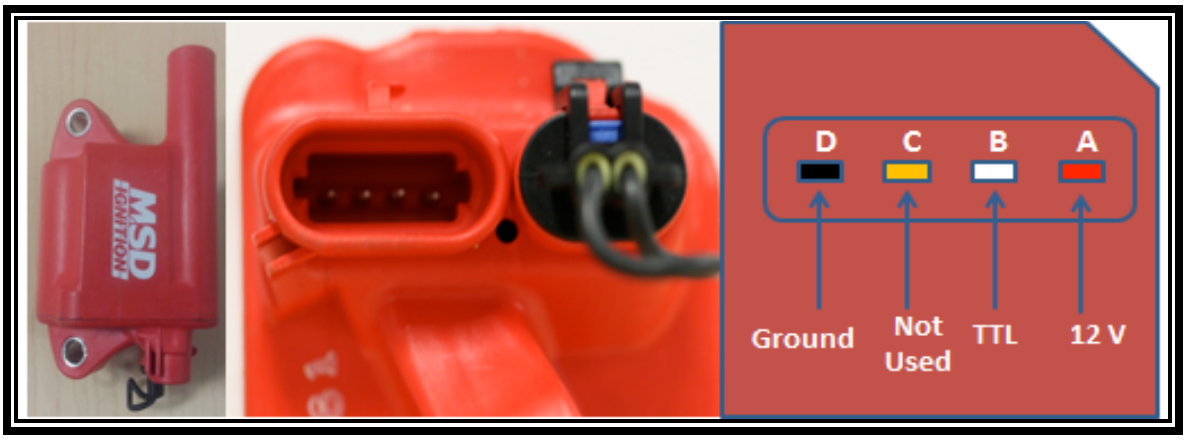

Figure 3.6: MSD ignition coil and pin-out

4.1.4 Flow control system

All of the solenoid valves and delivery line hardware/instrumentation is wired to a main switch panel housing the wiring/connections. This panel provides an interface of mechanical switches that control individual valves in the system. Instrumentation is powered though additional power supplies and wall outlets depending on the needed type of power. DC and AC power is supplied by internal connections on the control box through quick disconnect connections that are routed to the outside of the box. This allows for flexibility to switch out hardware if needed. Additional power connections are available in case more hardware is needed with both AC and DC power capabilities. The control panel allows the user to set the system to "manual" or "software controlled" control mechanisms. Manual control refers to being able to control each individual valve through the use of the mechanical switches available. There are two separate emergency switches, which cut power to the all valves in the gas delivery lines and the water supply for exhaust cooling respectively. The control panel is shown in Figure 3.7.

Figure 3.7: Mechanical switch control panel

When the system is under “software control” the user can no longer control the valves via the mechanical switches, instead it must be done through a LabVIEW software interface. The data acquisition system consists of PCI cards capable of acquiring voltage inputs from the instrumentation in the line, as well as PCI cards with mechanical relays for valve control. These may be seen in Figure 3.8.

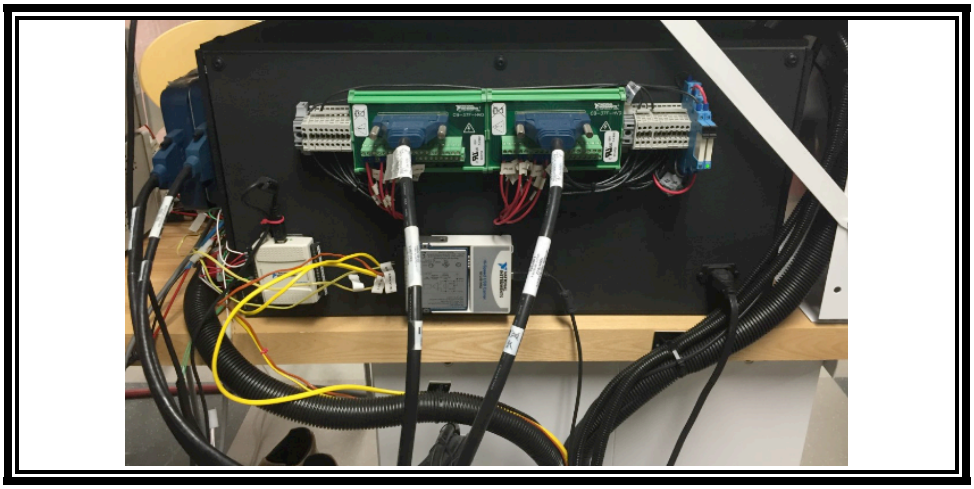

Figure 3.8: DAQ and solenoid valve control cards

Due to the fact that no valve control automation was required for these experiments, the LabVIEW software interface is relatively simple. It consists mainly of numeric indicators and boolean control operators for valve control. The user interface is shown in Figure 3.9 and the corresponding connection diagram is presented in Figure 3.10.

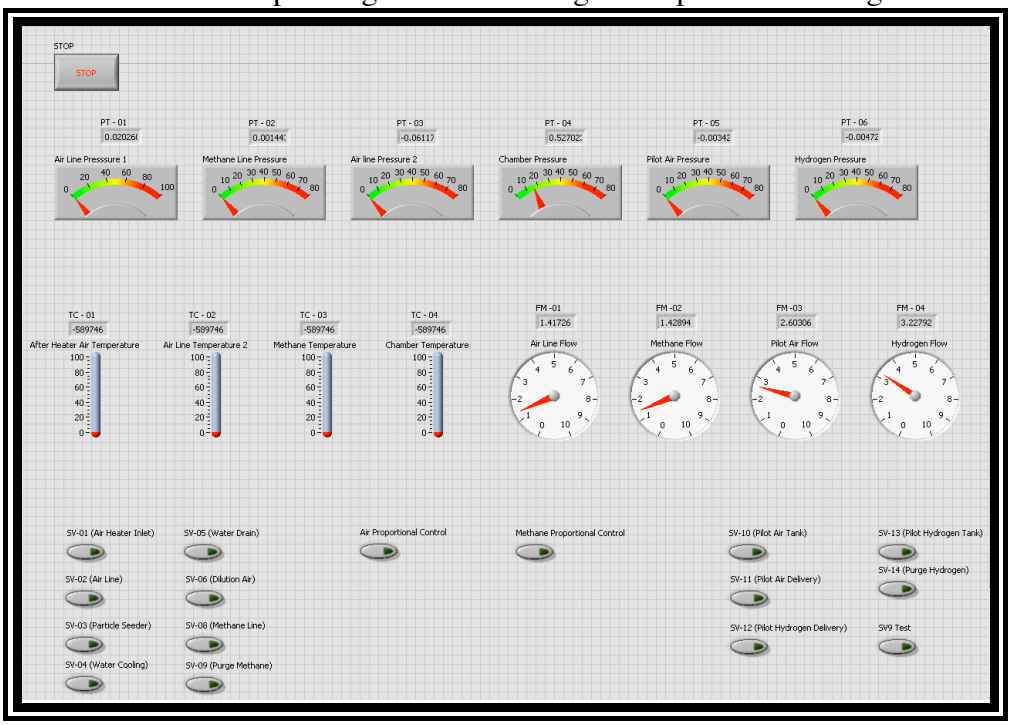

Figure 3.9: LabVIEW control user interface

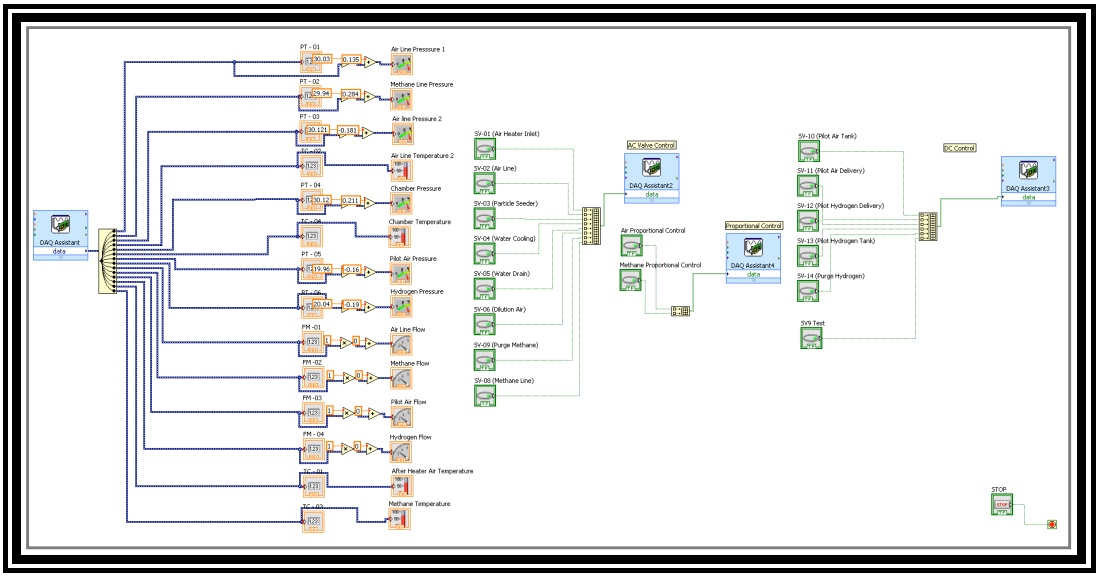

Figure 3.10: DAQ assist block diagram

3.1.5 Particle Image Velocimetry (PIV) System

The light plane was generated by a '*Litron LDY15-1000 Dual power*' 527nm Nd-YLF laser with a pulse energy of 15mJ/pulse. The maximum power output of the laser was 100W and the maximum trigger rate was up to 10 kHz with pulse duration of 150 ns. The laser system generated a 75mm wide 0.2 mm thick light sheet, which is guided by a 45^0 angle of attack mirror and a telescope optics. The laser head is water-cooled by a manufacturer provided chiller. Figure 3.11 shows the laser head, chiller, and particle seeder, along with the laser beam redirection to the top of the combustor.

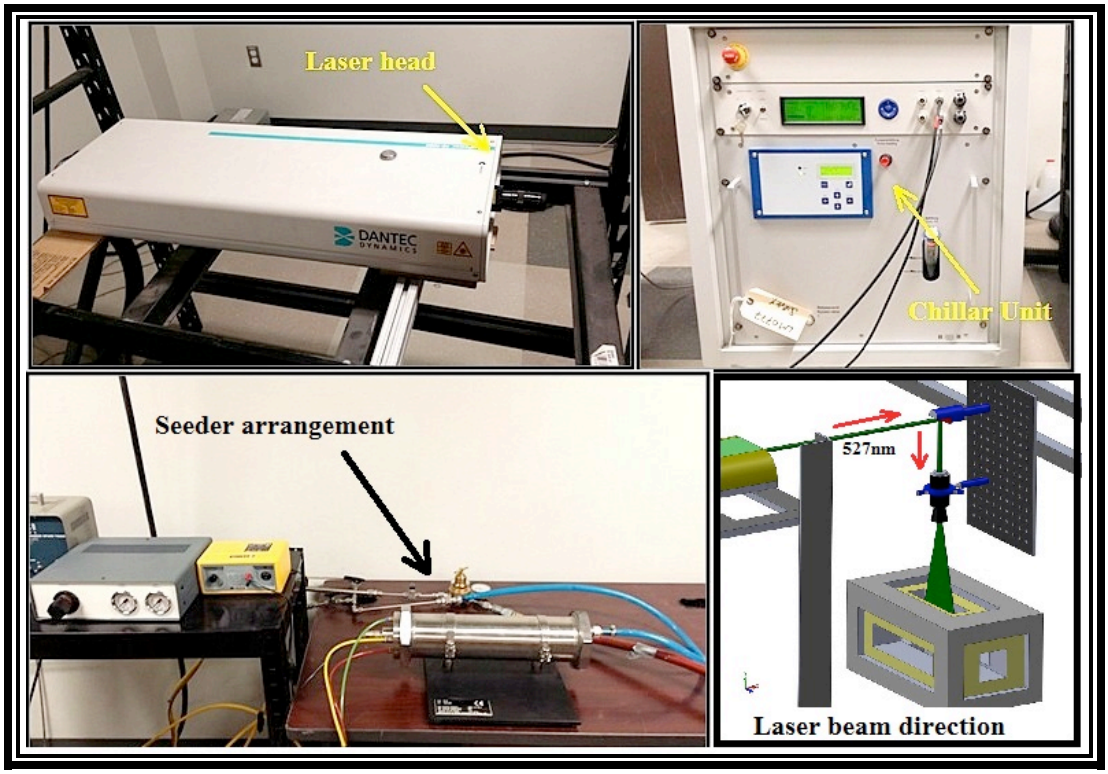

Figure 3. 11: Nd-YLF laser head and chiller, particle seeder, and laser beam direction.

The collection optics system was located perpendicular to the laser sheet, using one of the visual accesses provided by the combustor side windows. The high speed imaging system consists of a '*Speed sense 9070*' CCD camera with a maximum frame rate of 500 kHz and widescreen resolution of 1280x800. For this set of experiments, with a laser trigger rate of

10kHz, the image plane was 56mm x 42mm with a resolution of 720 x 480 pixels. A 532 nm filter was placed on the camera lens to reduce noise and background reflections other than the laser light reflected by the seeding particles. Alumina (Al_2O_3) particles with a mean diameter size centered on 1μm were used to seed the flow.

3.1.6 Laser Induced Fluorescence System

The PLIF system consists of a frequency doubled dye laser (Radiant Dyes NarrowScan HighRep Dye Laser) pumped by a Q-switched DPSS laser (Nd-YAG Edgewave IS series) and an intensified high frame rate CCD camera ('Speed sense 9070' with Hamamatsu C10880-01C).

The Nd:YAG laser pumps a 532 nm beam trough the tunable dye laser. The power output of the laser is 28W at 5kHz and 20 W at 10 kHz resulting in 5.6 mJ/pulse and 2 mJ/pulse respectively, entering the oscillator at the dye laser. The dye laser uses different dyes and an auto tracking BBO crystal assembly to tune the laser to the desired wavelength of interest. The instantaneous flame front structures were imaged by OH-PLIF and CH-PLIF at excitation wavelengths of 283.3 nm and 314.4 nm respectively. Table 3.3 summarizes the dye requirements and characteristics for detection at each of these wavelengths using this laser system. The tuning range of the LIF system is 367-769.

Table 3. 3: Summary of laser dye characteristics

Species	Dye	Tuning Range (nm)	Efficiency (%)	Peak (nm)	Pump (nm)
CH	DCM	607-663	30	640	532
OH	Rhodamine 6G	554-585	30	562	532

Rhodamine 6G in ethanol was used in the dye laser for OH radical detection, with the laser producing approximately 0.3 mJ/pluse of UV energy at 10 kHz. The laser was tuned to 283.28nm to excite A-X band of OH. DCM in ethanol at a concentration of 0.55 g/L was used for CH radical excitation, with the laser producing approximately 0.25 mJ/pluse at 5 kHz. The

laser was tuned to 314.4 nm to excite the C-X band of CH. Figure 3.12 shows the laser system assembly.

Figure 3. 12: PLIF assembly

Fluorescence was detected using an image intensifier equipped with a Cerco 100 mm f/2.8 lens coupled to a high-speed camera. The camera had a resolution of 640X480 pixels at 10kHz providing a resolution of 105.48 um/pixel. A UG-5 colored glass filter was placed on the camera lens to block visible light but allow UV fluorescence to pass through. The intensifier gate was set to 100 ns.

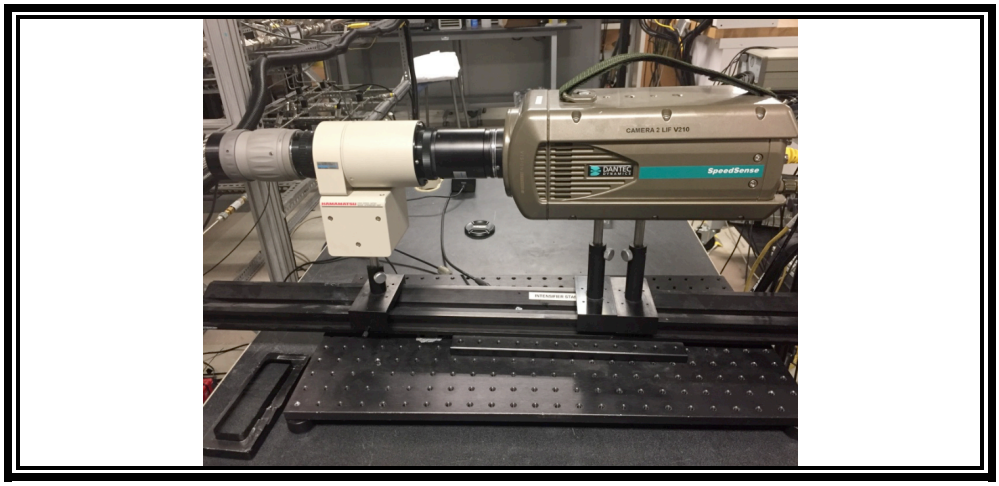

Figure 3. 13: Intensified camera assembly

The intensified camera assembly is presented in Figure 3.13. The electric connection diagram for the PLIF system is shown in Figure 3.14. The laser pulses were formed into an approximately 50mm wide sheet using a cylindrical telescope lens. The UV laser sheet may be overlapped with that of the PIV system using a 25 mm dichroic mirror as shown in Figure 3.15. Narrowband bandpass filters were placed in the camera lens to limit noise in the images centered around 283 nm and 314nm for OH and CH detection respectively. The use of an intensifier gate pulse of 100 ns was used to minimize background flame chemiluminescence. A timer box was used to synchronize laser, camera, and intensifier pulses. The system was ran at 10kHz, acquiring 1000 OH images per run at a resolution of 640x480 pixels, and at 5 kHz for CH detection.

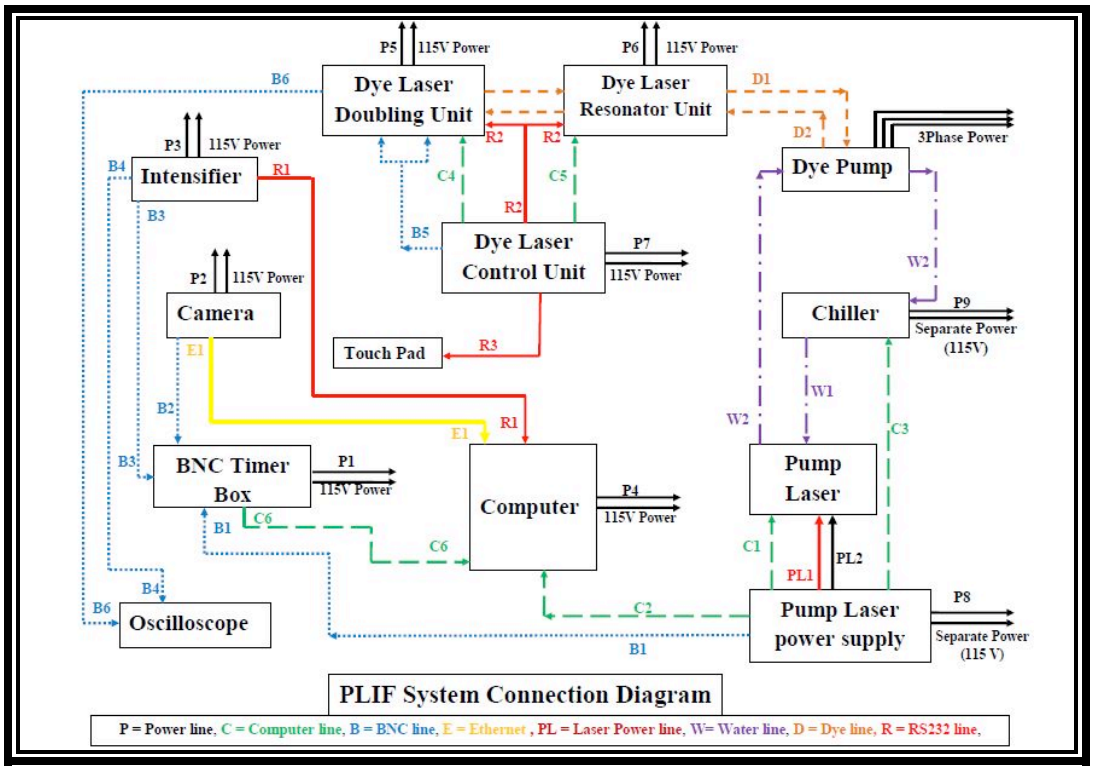

Figure 3. 14: PLIF system connection diagram.

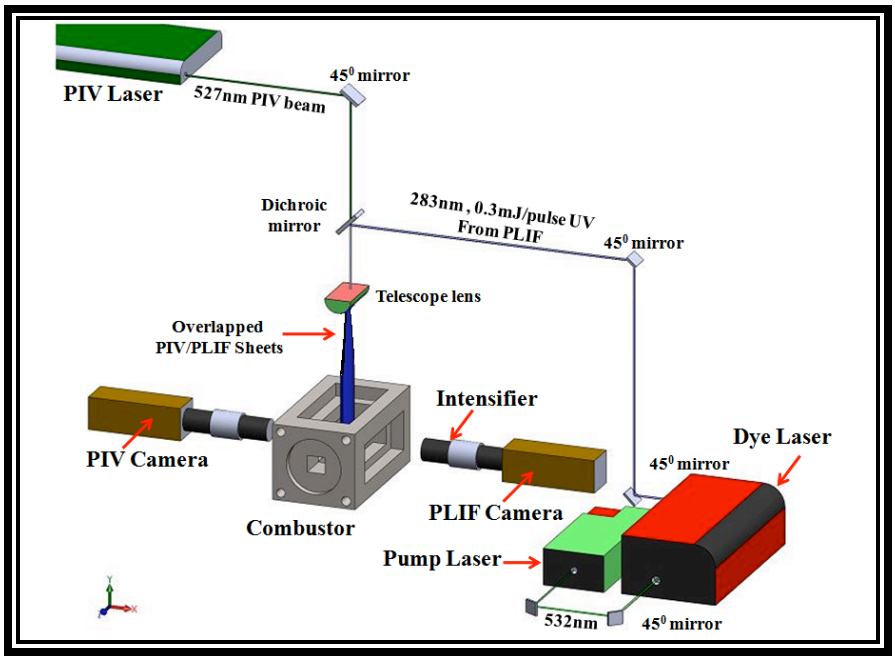

Figure 3. 15: PIV and PLIF integration with combustor

3.1.7 Laser System Control

A dedicated computer system loaded with the DynamicStudio laser optical measurement system software (Dantec Dynamics) was used to control the laser systems and acquire/process PIV and LIF images. DynamicStudio communicated with timer boxes controlling each laser system, which in turn sent trigger signals to the cameras, lasers, and intensifier unit. For the results presented in this work, the laser systems were ran independently. However, the system may be ran simultaneously with the appropriate timing/synchronization scheme by making one timer box a "slave" of the other. Figure 3.17 shows a sample user interface in DynamicStudio showing the connection diagram for the LIF system.

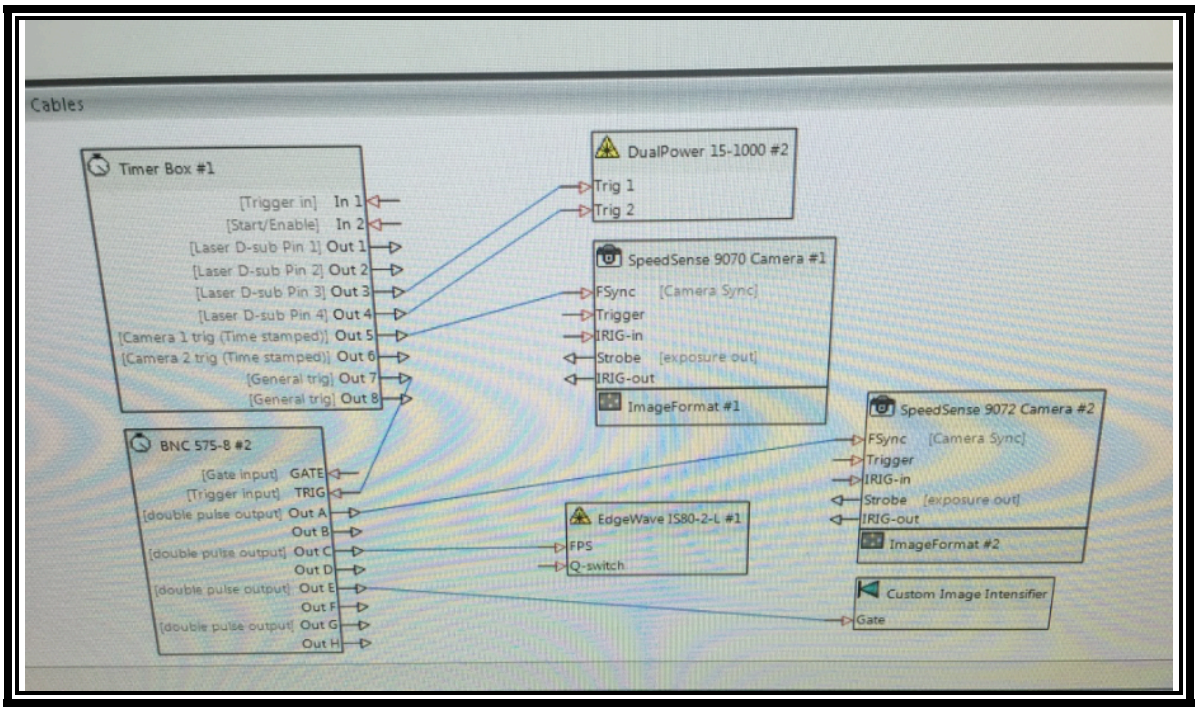

Figure 3.17: DynamicStudio control software connection diagram

Calibration procedures were also conducted with Dynamic Studio. These consisted of imaging a known distance inside the combustor at the approximate location where the laser sheet was to be placed; in this case, a metallic ruler was used. Once the image is obtained, the user can set the origin on the image and specify the scale for the images in the software; this is done by relating a known distance (i.e. one inch in the ruler markings) on the software to the resolution of the camera. Once this known distance is set, the software automatically correlates the distance each pixel represents in the picture. An instruction manual for the use of the PLIF system was developed, thus if further information is needed or for specific steps on how to complete a calibration on DynamicStudio please refer to the PLIF Manual developed for the cSETR.

3.1.8 Test Matrix

Figure 3.18 summarizes the test matrix for the experiments reported in this dissertation. The experimental runs used a total of four different grids with blockage ratios of 46% and 63%; each with hole diameters of 1.5 and 3mm. Each grid was tested at different bulk flow rates, meaning increasing Reynolds numbers of 15000, 32000, and 64000 based on step height. All

tests were conducted at an equivalence ratio of Φ=1 whereas the bulk flow velocity ranged from 10 – 45 m/s at the combustor entrance. The intent is to study the effect of change in length scale and turbulence intensity in the flame front characteristics of the air-methane flames inside of the combustor. The turbulence generated by the grid will be noticeable in the velocity fluctuations u' near the combustor entrance. This means that velocity fluctuations can be modified by varying the grid characteristics, in this case the hole diameter and blockage ratios. The turbulence properties are also a function of flow velocity at the combustor entrance. Hence these were the two parameters chosen for variation during these studies.

Blockage Ratio (%)	Hole Diameter (mm)	Flow Rate (scfm)	Re_H	U_{bulk} (m/s)
46	1.5	13	15000	10
		27	32000	20
	3	54	64000	39
61	1.5	13	15000	10
		27	32000	20
	3	54	64000	39

Figure 3.18: Combustion studies test matrix

Chapter 4: Results and Discussion

The following chapter will discuss the results obtained with the OH and CH PLIF flame front studies

4.1 PIV – Turbulence Parameters

The test matrix presented in Chapter 3 provided the test points for the experimental runs. Four grids (two of BR 46% with 1.5 mm and 3mm hole diameters; two of BR63% with 1.5 mm and 3 mm hole diameters) were tested at varying Reynolds numbers. Turbulence parameters including: turbulence intensity levels (u'/U), velocity fluctuations (u'), and integral flow length scales were obtained through the data gathered by the PIV system. Calculated flame parameters, through the use of the CHEMKIN software package, allowed for the determination of Damkholer (Da), Karlovitz (Ka), and turbulent Reynolds numbers (Re_t). This work is interested in the characterization of flame structure at these conditions. In summary, flames with $0.8 < Da < 34$, $0.8 < Ka < 95$, $3 < u'/S_L < 72$, and u' values ranging from 1-27 m/s were obtained. All tests were conducted at an equivalence ratio of $\Phi=1$ whereas the bulk flow velocity ranged from 10 – 45 m/s at the combustor entrance. Therefore, the geometric Reynolds number was varied through the modulation of bulk flow rate, and ranged from 15,000 – 64,000 based on step height at the combustor. Table 4.1 summarizes the values for turbulent combustion parameters found for each test condition.

Table 4. 1: Summary of test conditions

Grid	Re_H	Φ	U_{Bulk} (m/s)	u' (m/s)	Da	Ka	Re_T	u'/S_L	L_T
48% BR - 1.5 mm dia	15,400	1.0	10	1.1	21.3	0.8	147.5	3.0	0.0173
	32,100	1.0	25	3.5	18.8	7.0	458.4	9.3	0.0173
	64,200	1.0	45	23.4	0.9	70.3	3034.6	61.5	0.0173
46% BR - 3 mm dia	15,400	1.0	10	1.7	34.2	1.7	234.2	4.4	0.0186
	32,100	1.0	25	9.8	2.2	18.2	1364.7	25.7	0.0186
	64,200	1.0	45	18.9	1.3	50.2	2647.4	49.8	0.0186
63% BR - 1.5 mm dia	15400	1.0	10	5.5	5.1	10.3	604.5	14.5	0.0146
	32100	1.0	25	7.5	4.3	16.8	824.0	19.7	0.0146

62% BR - 3mm dia	64200	1.0	45	25.6	0.9	90.2	2814.1	67.4	0.0146
	15400	1.0	10	2.5	13.9	3.4	300.5	6.6	0.0160
	32100	1.0	25	11.0	1.8	24.6	1315.9	28.9	0.0160
	64200	1.0	45	27.7	0.8	95.9	3316.9	72.8	0.0160

It is important to note that for the purpose of summarizing the data, test points for each condition were averaged out to obtain the values presented in Table 4.1. The turbulence intensity, integral length scale, and bulk flow rate are the main parameters of importance in this study. These parameters allow for the calculation of parameters to determine flame regime location. Based on the measured turbulence parameters and calculated flame parameters, the flames tested in the experimental runs lie within the thin reaction zones (thickened flame regime) in the Peters modified Borghi diagram as shown in Figure 4.1. Flame points approaching the broken reaction zones are those with lower Da numbers and higher turbulence intensity. In this case, as the Reynolds number increased, the location of the flames in the flame regime diagram moved up towards the broken reaction zones. This led to difficulties in maintaining the flames stable at the higher turbulence intensity levels, as well as being unable to further increase the Reynolds number past 64000 as bulk flow velocity an turbulence levels resulted in non-ignition points past that level.

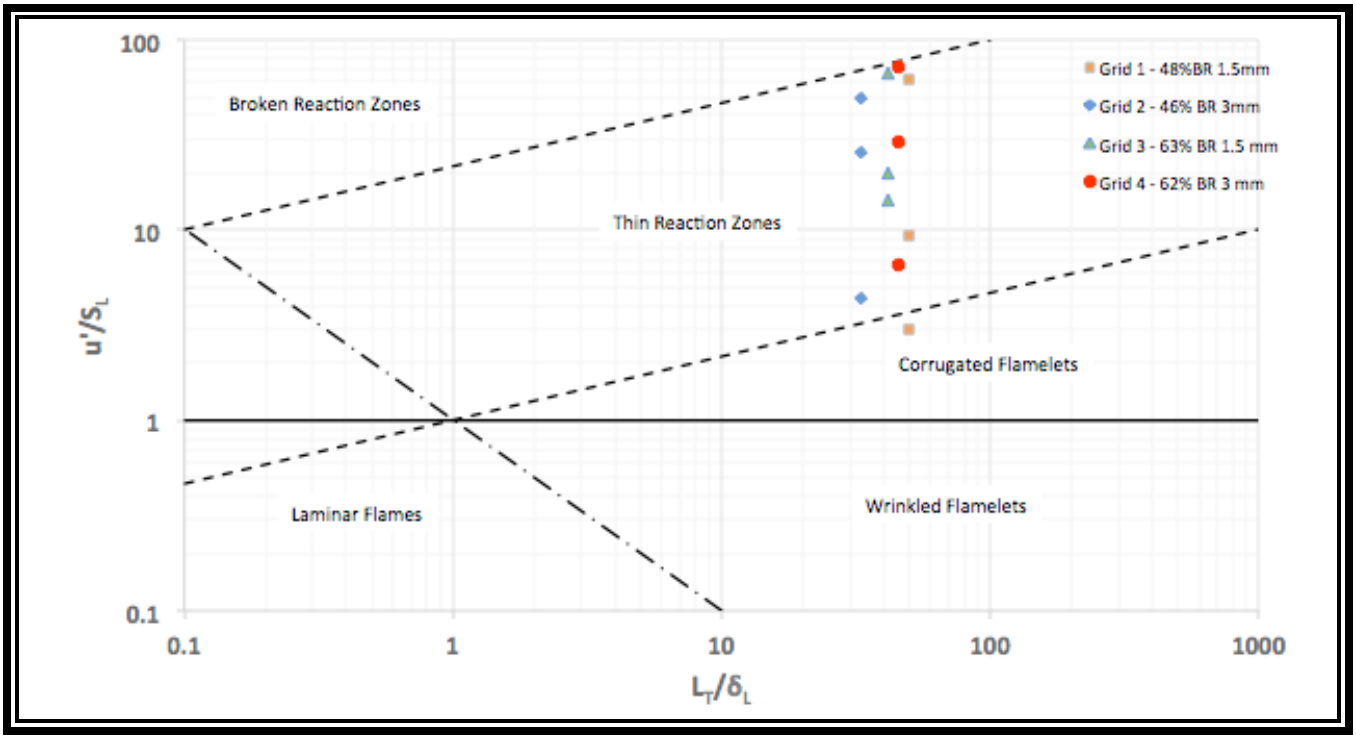

Figure 4.1: Experimental Conditions in the Peters-Borghi turbulent combustion diagram

4.2 OH LIF

OH-PLIF was conducted with a pulse energy of ~0.3 mJ/pulse by using Rhodamine 6G to tune the dye laser to the OH excitation wavelength at 283.28 nm. This transition is a preferred excitation wavelength around the scientific community for not having strong temperature dependence as well as a strong intensity. Figure 4.2 shows samples of instantaneous images of reacting flow inside of the combustor at increasing Reynolds numbers conditions from top to bottom. All images shown in this results section present a flow direction of left to right.

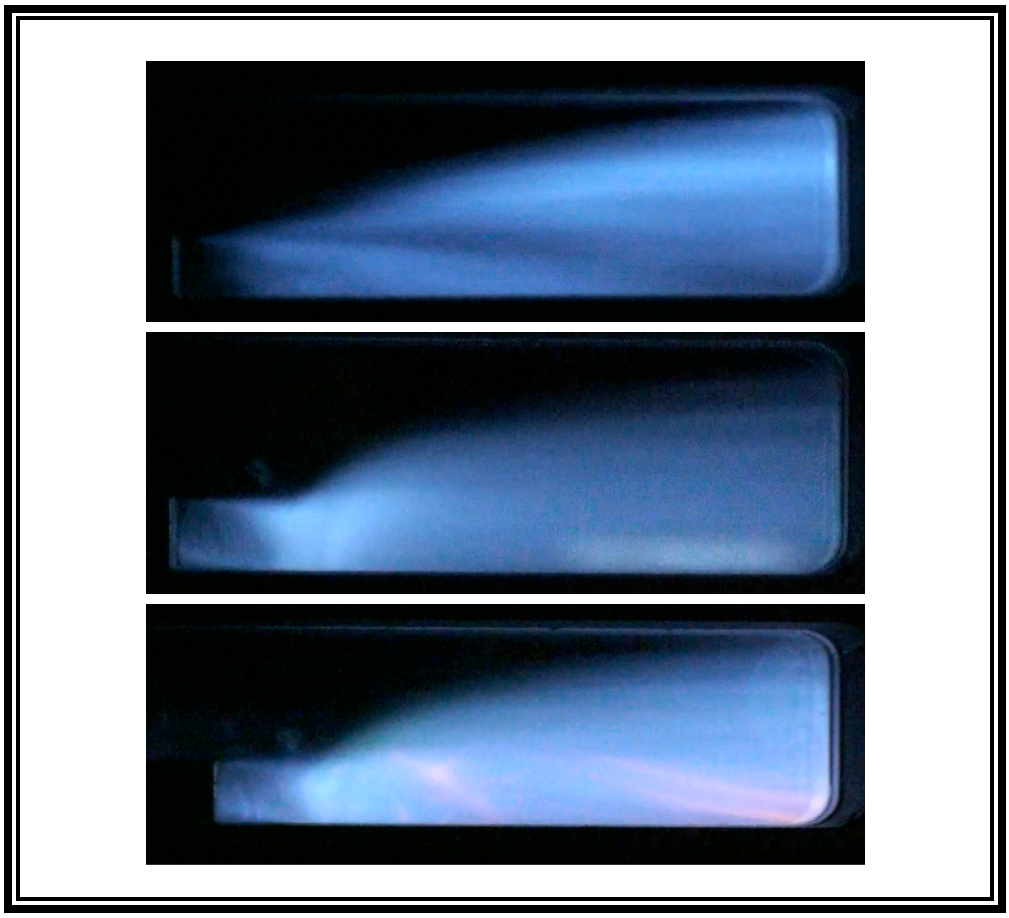

Figure 4.2: Instantaneous images of reacting flow inside combustion chamber. Top to bottom; Re=15000, Re=32000, Re=64000 (flow direction: left to right)

The instantaneous OH-LIF images at the 10kHz trigger rate allow for the visualization of the flame front evolution. Grid 1 – 48% blockage ratio and 1.5 mm hole diameter will be discussed first. At Re=15,000 flame front wrinkling was evident as well as continuous movement of the front up and down the combustor height in a flapping motion. Figure 4.3 presents a set of 9 instantaneous frames for the reacting flow of this grid, showing the progression of the wrinkling of the flame front for 0.9 ms under the following turbulence conditions: U_{bulk}=10 m/s, u'=1.1 m/s, Da=21, Ka=0.8, Re_T=147. These conditions are summarized in Table 4.1.

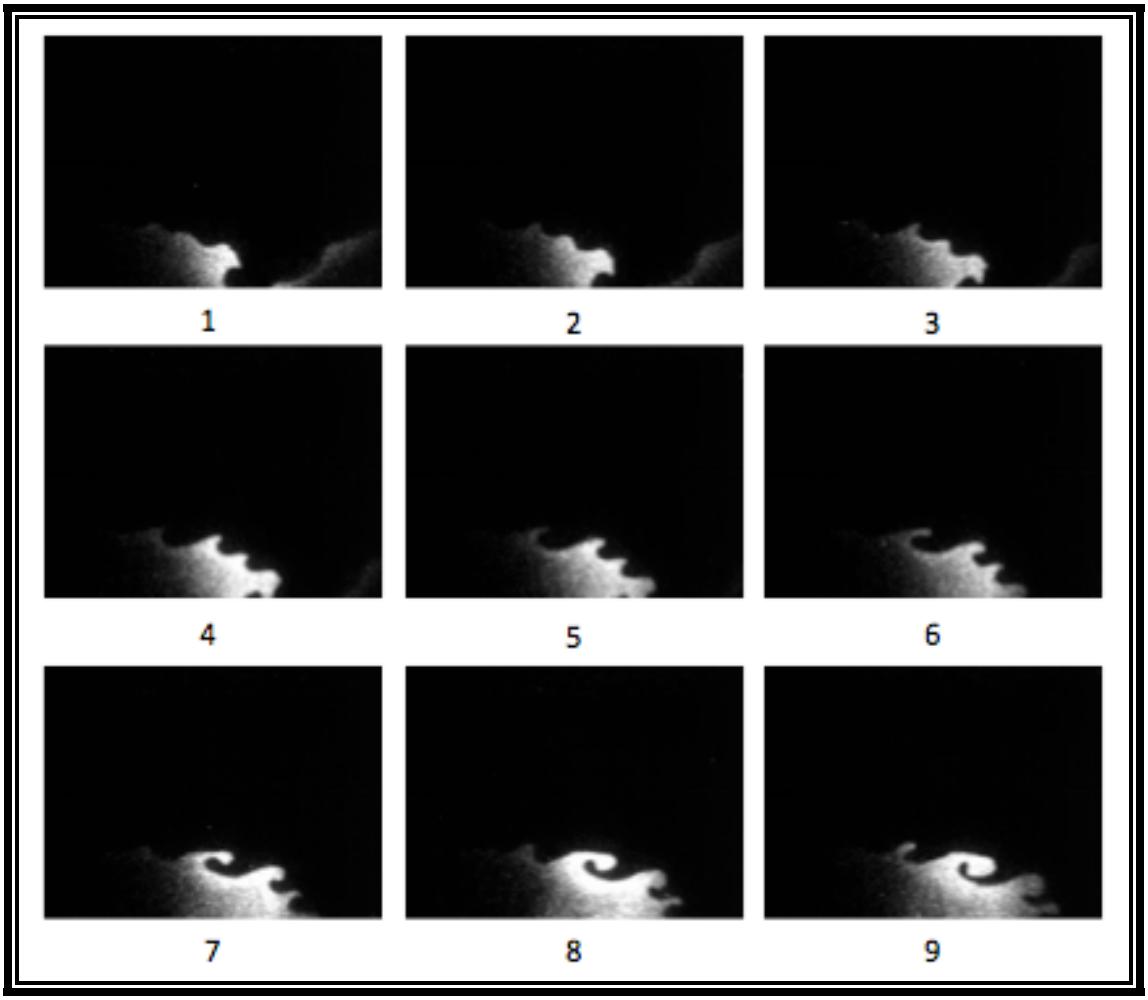

Figure 4.3: Grid 1 Re=15000 instantaneous frames of flame front wrinkling evolution

The black portions of the images represent the unburned gas mixture, while the bright portions of the picture represent the burned products. The flame front is located at the boundary between these two sections. For clarity purposes, frame 8 from Figure 4.3 was selected for further image processing and is presented in Figure 4.4. Switching the image to a binary format allows for a better visualization of the flame front. Once in binary format, it is simpler for the image processing software to recognize the flame front edge and outline it with a contour line. Flame wrinkles develop and begin to elongate along the flame front as a result of the turbulence inside of the combustor. However, turbulence is not high enough to cause these elongated wrinkle separation from the flame front as seen in the image progression. These elongated

wrinkles eventually blend in with the rest of the flame as they travel downstream through the flame front. This is indicative of large scale driven turbulence, since the flame front is wrinkled, yet no evidence of small-scale turbulence may be derived at these conditions form the images recorded.

Figure 4.4: Isolated instantaneous frame, binary image, and flame front outline

As the bulk flow velocity was increased, resulting in a Re=32,100, the turbulence effects are far more evident. The flow conditions were the following: U_{bulk}=25 m/s, u'=3.5 m/s, Da=18, Ka=7, Re_T=458. For the previous case, the flame front and wrinkles had a relatively smooth contour all around. For the case of Re=32,100 a rough flame front and wrinkle contour was seen. As with the previous case, a sequence of nine instantaneous images corresponding to 0.9 ms of combustion demonstrate the flame front wrinkling evolution and is presented in Figure 4.5.

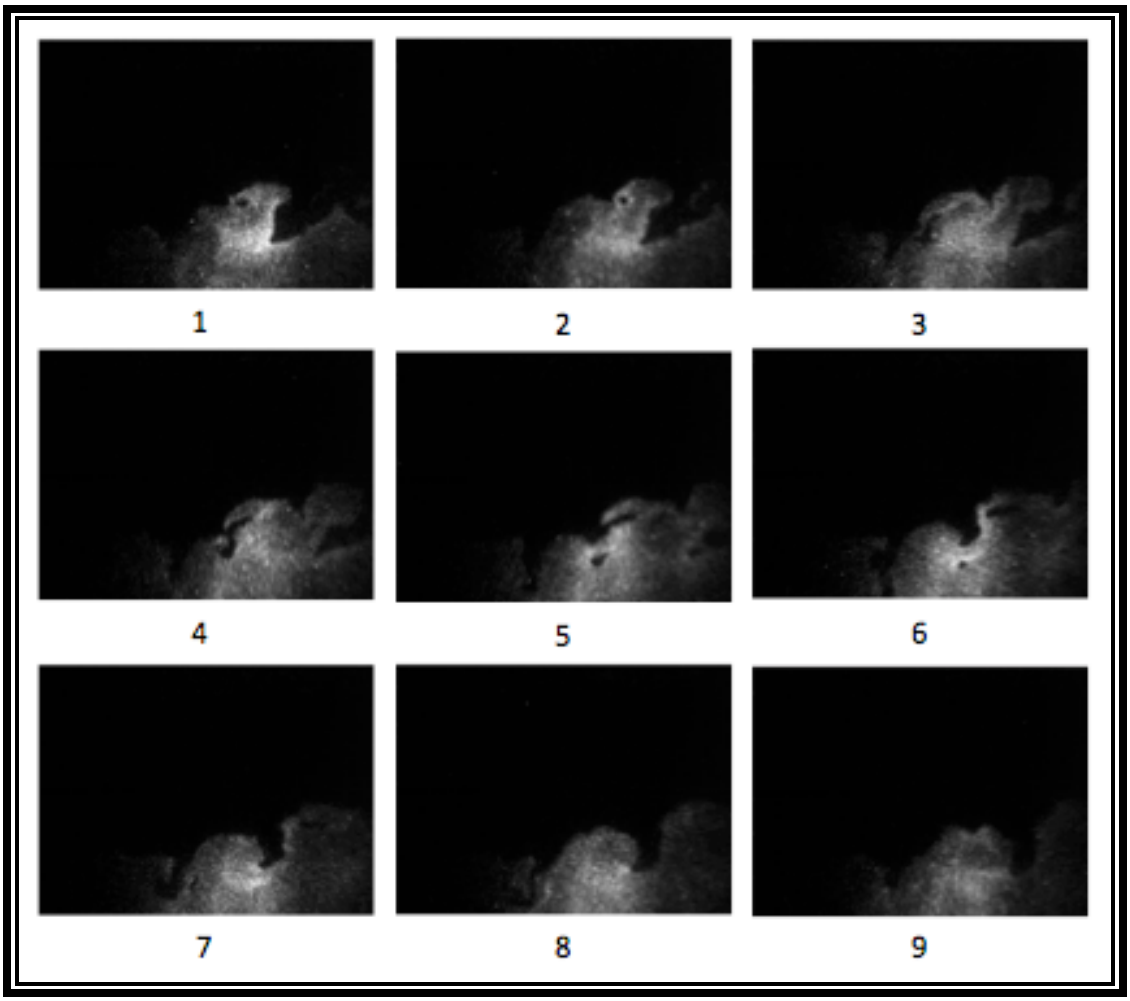

Figure 4.5: Grid 1 Re=32000 instantaneous frames of flame front wrinkling evolution

In this case, the wrinkle formation is quite different than that of the lower bulk velocity. Thick portions of the flame front form large and thick wrinkles as the ones shown in frames 1-2 and 7-9. However much thinner and smaller wrinkles branch off from these as seen in frames 4, 5, and 6. Another interesting finding is that these thinner wrinkles will sometimes seem to capture pockets of unburned gases as shown in frames 1, 2, 5, and 6. The unburned gas pocket travels downstream with the flame front and is eventually leaves the field of view of the camera. Figures 4.6 and 4.7 isolate images 4 and 5 to highlight the characteristics that were just discussed.

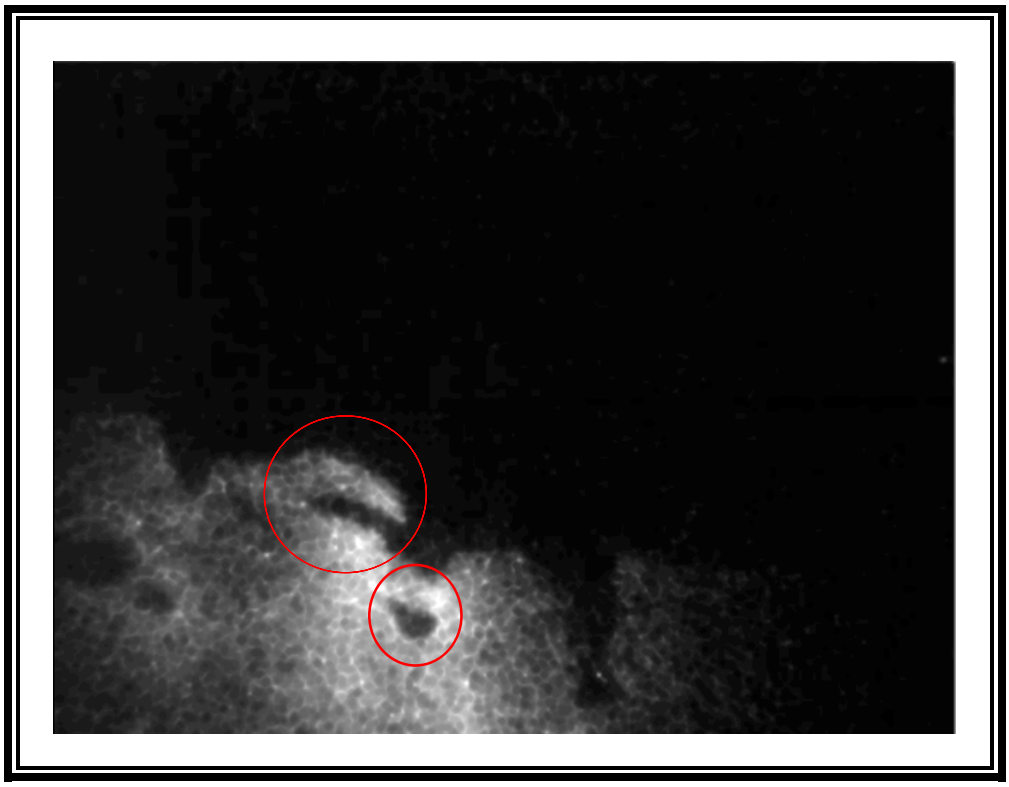

Figure 4.6: Grid 1 Re=32000 Unburned gas pocket and wrinkle branch

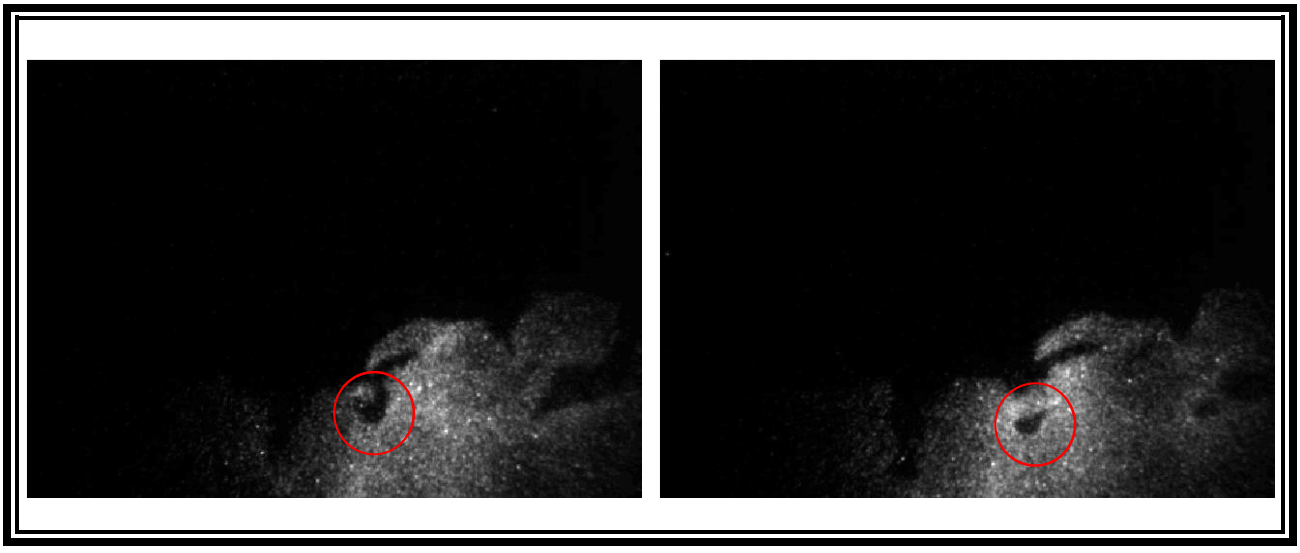

Figure 4.7: Grid 1 Re=32000 Unburned gas pocket formation evolution

During the 0.9 ms interval presented in Figure 4.5, frames 3,4, and 5 show OH zones that are clearly converging upon one another. In Figure 4.7, which isolates frames 4 and 5, one sees

the highlighted region between the two OH-zones is significantly reduced. By the second frame, the two zones have apparently merged into a single flame front, capturing a pocket of unburned gas mixture in the process. These unburned gas pockets trapped inside the burned gas section decrease in size as they move downstream or disappear from the field of view. They are more than likely consumed by the surrounding burned products as they travel downstream.

Another feature noted during these test series for grid 1 was the intermittent appearance of flamelets or separation and re-attachment of burned products form the flame front as seen in Figure 4.8. The flamelet separation begins in the transition between frames 1 and 2. By frame 3, there is clear burned product pocket separation from the flame front and an eventual reattachment as shown in frame 4. Similar behavior was reported by Tanahashi et al [36], who noticed "isolated burned gas in the unburned mixture and isolated unburned mixture in the burned side" for flames tested in corrugated flame regimes bordering thin reaction zones. They attributed these events to a possible 3D behavior of the flames under these flow conditions.

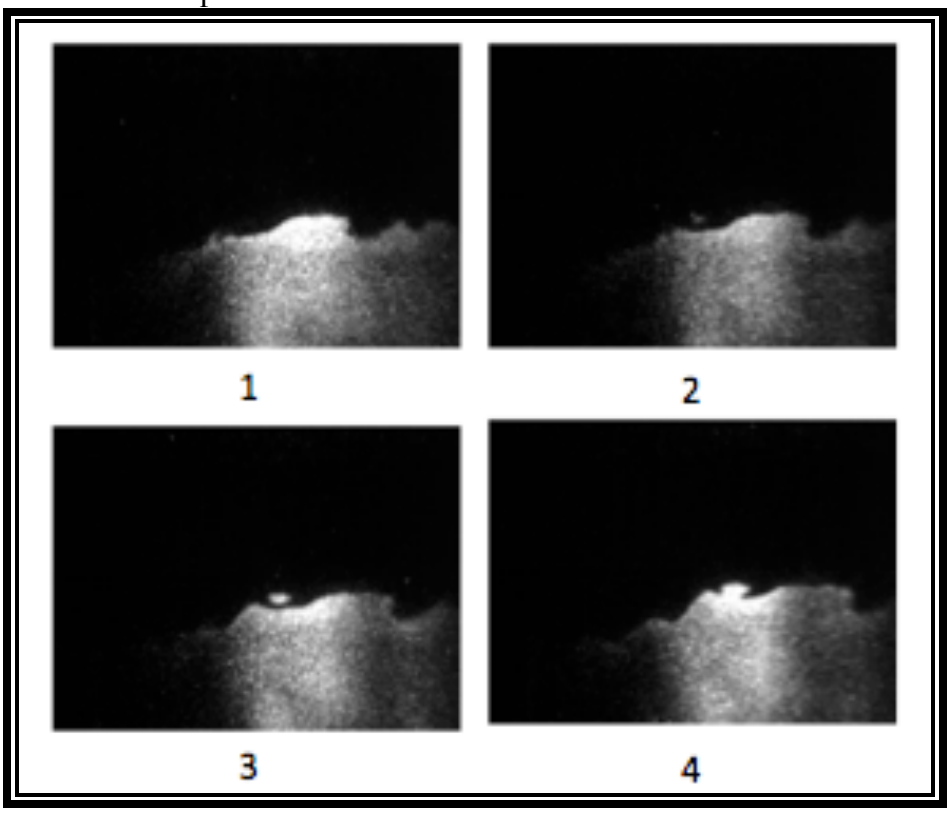

Figure 4.8: Grid 1 Re=32000 Isolated burned gas pocket separation and reattachment

The last test series for Grid 1 at Re=54,000 resulted in the following flame conditions: U_{bulk}=45 m/s, u'=23 m/s, Da=0.9, Ka=70, which represented a significant change in all of turbulent and flame parameters; the most notable being the u' value, which is indicative of a very high turbulence intensity at these flow conditions inside of the combustor. The formation of flamelets or burned gas pockets is far more evident for this case as seen in the image sequence presented in Figure 4.9. The wrinkling and stretching of the flame results in much thinner elongated wrinkles most of which result in separate flamelet or pockets of burned products formation along the flame front.

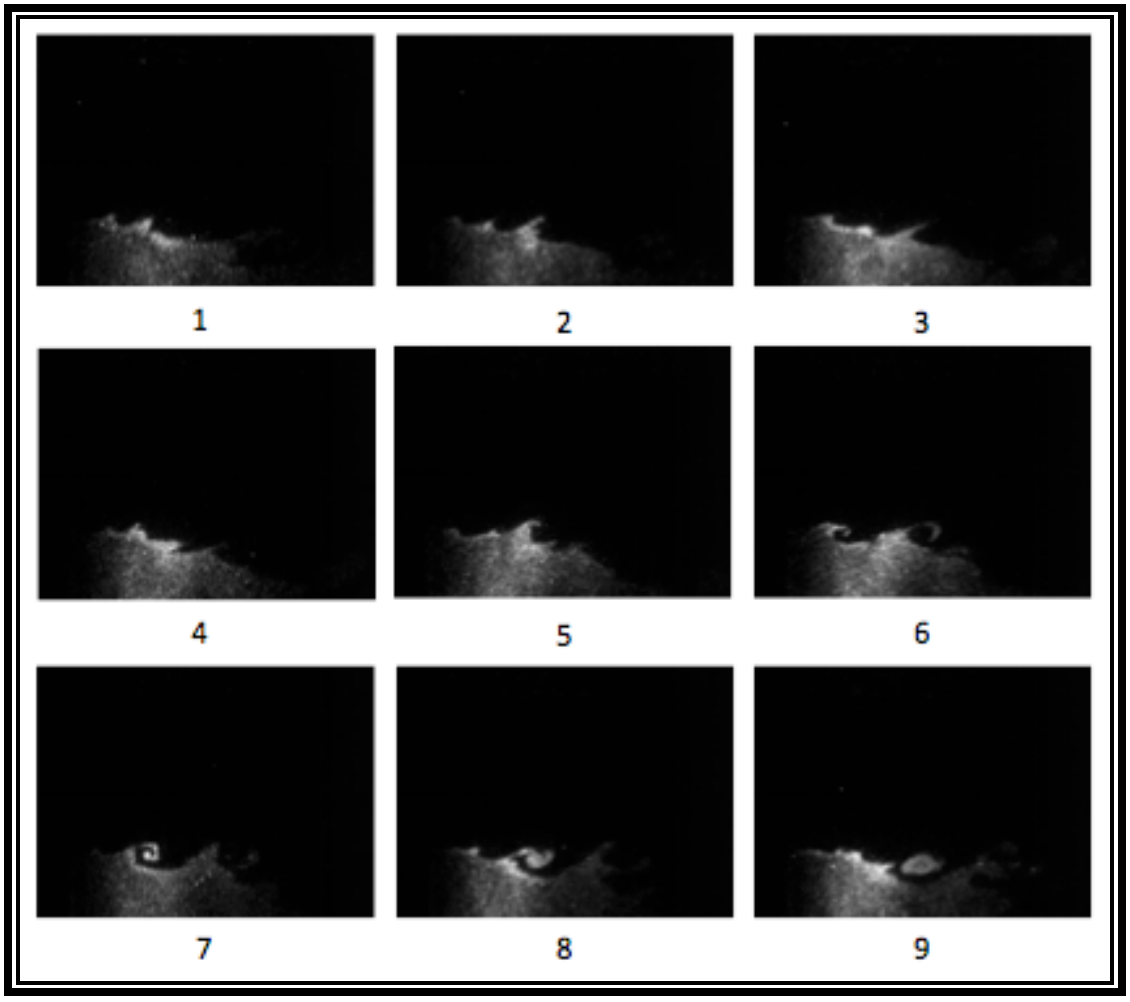

Figure 4.9: Grid 1 Re=64,000 instantaneous frames of flame front wrinkling evolution

Figure 4.10 isolates frames 7 and 8 from Figure 4.9, to show the thinner wrinkle formation along the flame front. The spiral shape of the wrinkle formation in frame 7 suggests eddies capable of creating a recirculation zone of a few pixels; most of these result in the formation of the flamelets as shown in frames 8 and 9. Figure 4.11 and Figure 4.12 isolate instantaneous frames of the flame at these conditions, showing the pocket of burned material separate from the flame front. It may be noted that the size of these flamelets vary as shown in the pictures, where some are only a few pixels in diameter while others can get to be up to ten times in size.

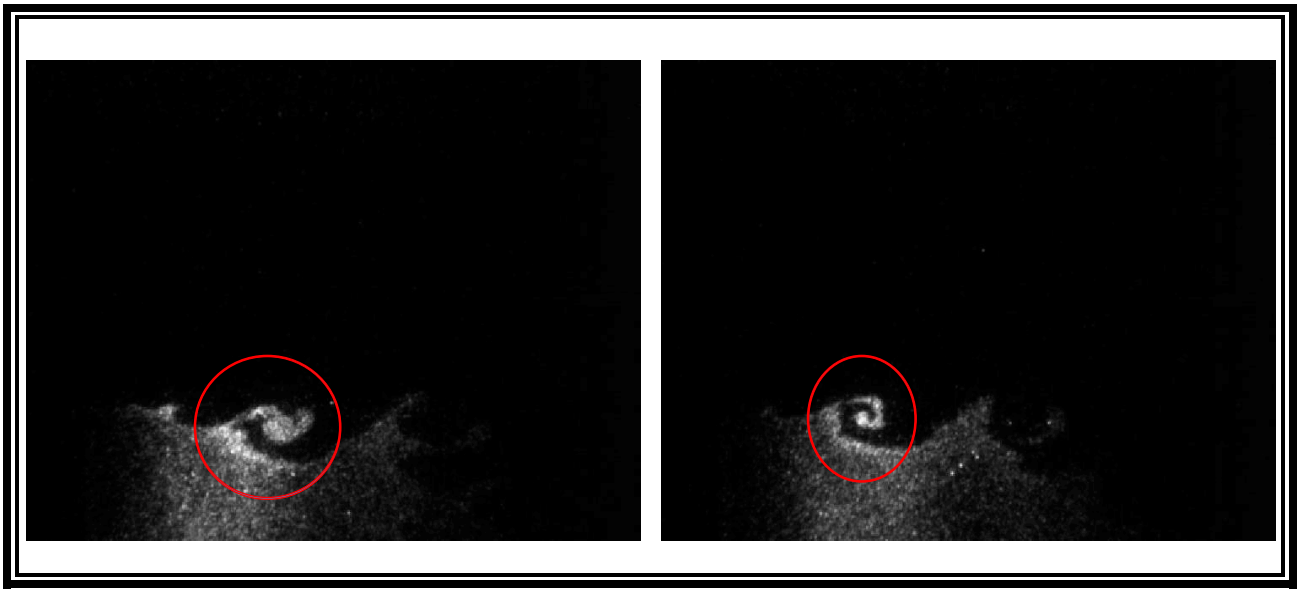

Figure 4.10: Grid 1 Re=64000 Burned gas flamelet formation evolution

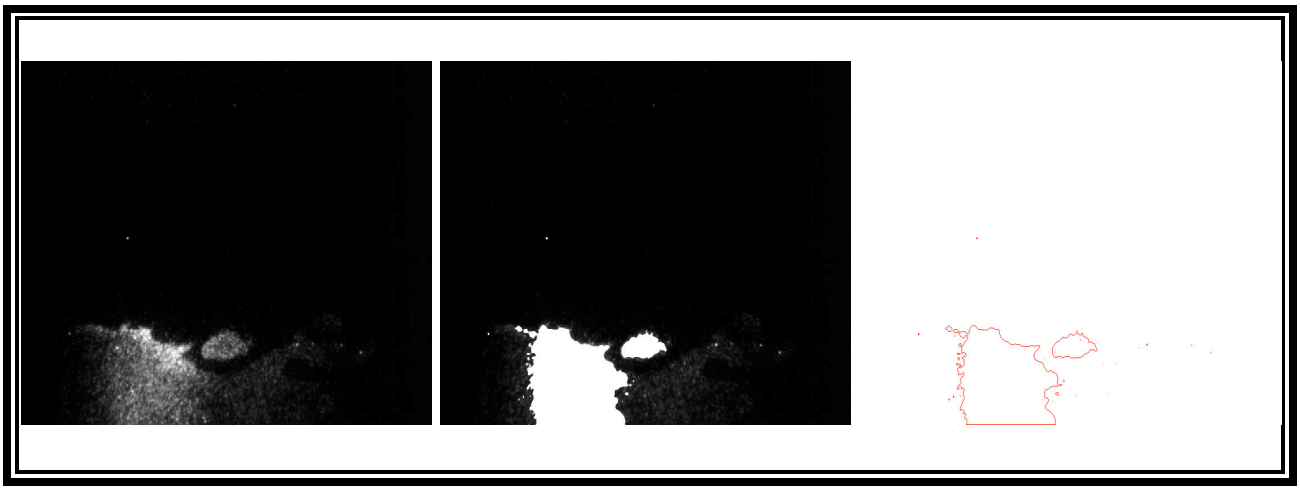

Figure 4.11: Grid 1 Re=64000 Burned gas pocket separation instantaneous frame, binary image, and outline

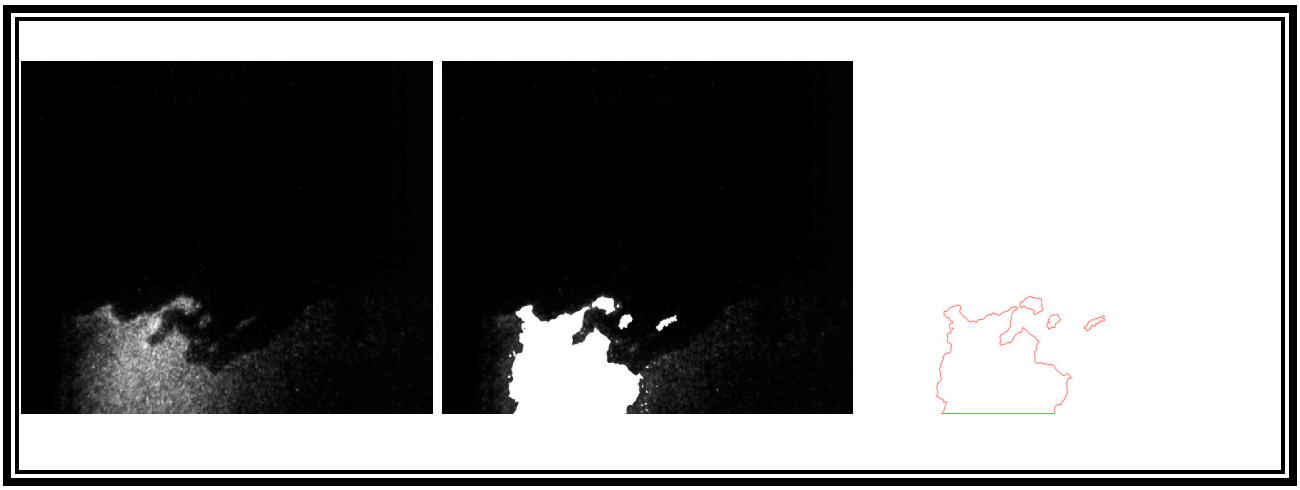

Figure 4.12: Grid 1 Re=64000 flamelet formation instantaneous frame, binary image, and outline

Grid 2 – 48% blockage ratio and 3 mm hole diameter was tested in order to see the effects of changing the flow length scale on the flame front structure. At Re=15000, the behavior is similar to that of Grid 1 where large scale wrinkling is evident with smooth flame front surface along the wrinkles. However, in this case the formation of wrinkles seem to occur faster and they seem to move through the flame front faster than in the previous grid. Flame wrinkling is more evident as the flame moves downstream. The turbulence conditions for this grid were the following: U_{bulk}=10 m/s, u'=1.7 m/s, Da=34, Ka=18, Re_T=234. These values are greater when

compared to those of Grid 1 at the same Reynolds number conditions. This suggests greater turbulence intensity inside the combustor for this flame.

Figure 4.13 shows a progression of instantaneous frames similar to the ones presented before. Overall the flame front becomes more wrinkled than that corresponding to grid 1. The sequence presented, shows three major wrinkles initially, as the flame front evolves the number of wrinkles double as seen in frames 7-9. The other main difference was the flame front flapping, which was not as evident for this grid as it was for the first one. The attenuation of the flame flapping behavior suggests a more stable flame at these conditions. The fact that turbulence levels are higher along with the stable behavior may suggest that the turbulence is well distributed inside the combustor or that it may in fact be contributing to a better mixing of the reactants inside the combustor.

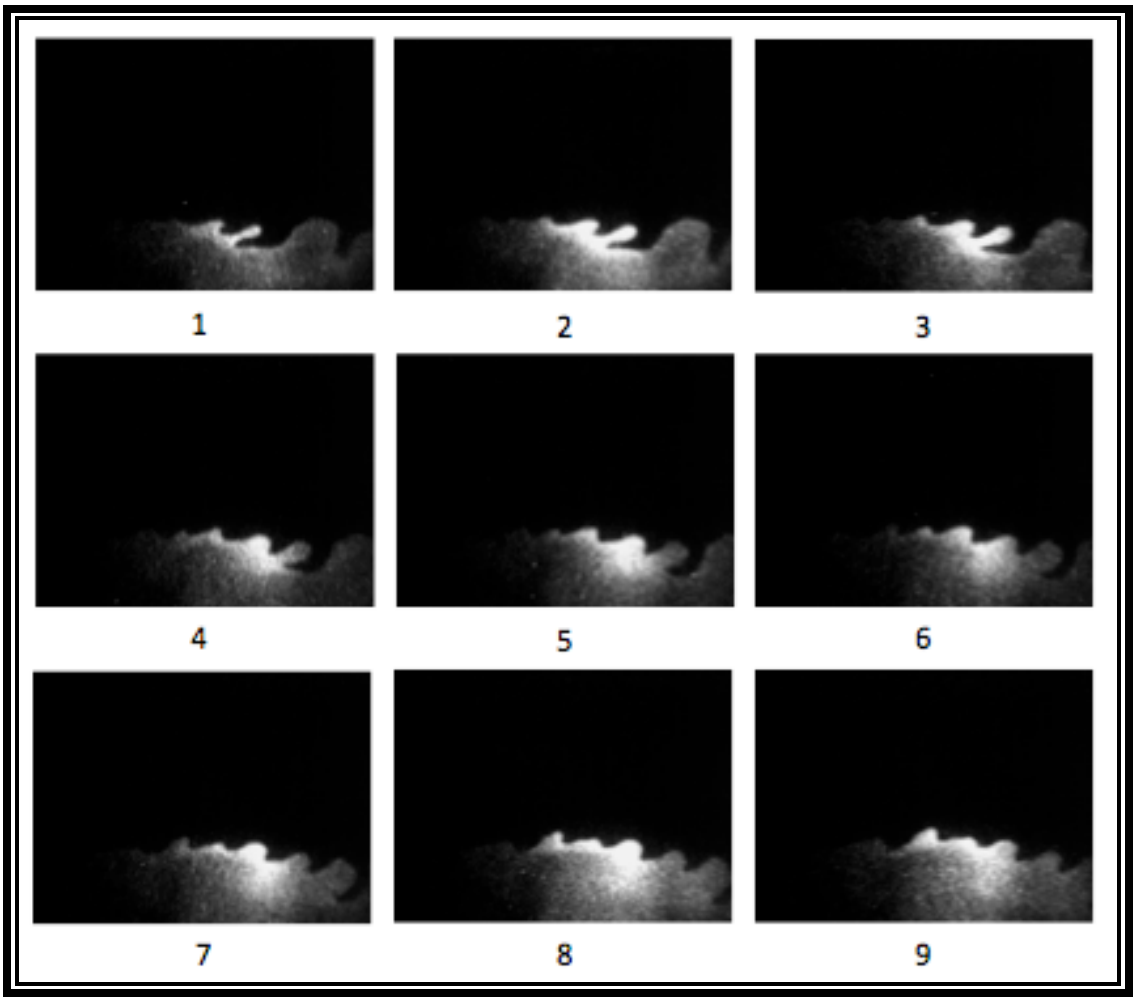

Figure 4.13: Grid 1 Re=15,000 instantaneous frames of flame front wrinkling evolution

An isolated frame with the corresponding binary image and outline is presented in Figure 4.14. One can note the smooth profile along all the wrinkles on the flame front. The wrinkles travel downstream if the combustor faster than those in Grid 1. This might coincide with another property noticed by Tanahashi et al [36] in their work with corrugated flames bordering the thin reaction zones region, where they stated to have noticed that gases may not always show high speed in a relatively high Re premixed flame, which might be the case for the flame at Grid 1. This may also be explained by a slightly higher local inlet velocity and thereby local Re, which leads to a turbulent intensity increases leading to a more wrinkled, flame front. This would

indicate a faster burning rate and more than likely local flame speed for the flames at this Re condition with Grid 2 when compared to those of Grid 1.

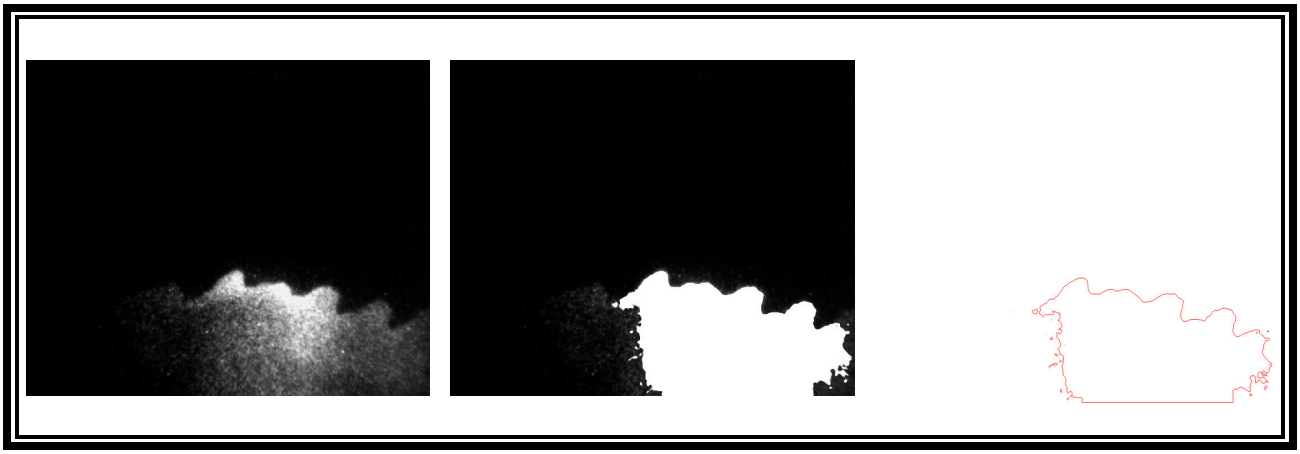

Figure 4.14: Grid 2 Re=15000 flame front instantaneous frame, binary image, and outline

At Re=32000, the conditions encountered were as follows: U_{bulk}=25 m/s, u'=9.8 m/s, Da=2, Ka=18, Re_T=1364. Even though the turbulence intensity was higher, there was no evidence of pockets of unburned gases being trapped by the thinner wrinkle formation as in Grid 1. In fact the wrinkling seem to be more uniform in the sense that there are no elongated structures branching off from the larger wrinkles, only very short wrinkles were noticed on some of these such as the ones seen in frames 6-8 of the sequence presented in Figure 4.15. Similarly to what was seen t Re=15000 with grid 2, the flame front flapping is not as evident as it was with the last grid. This might be an indication of better mixing or more stable combustion with the increased flow length scale. However, the flames at these conditions did not have any other specific feature for discussion.

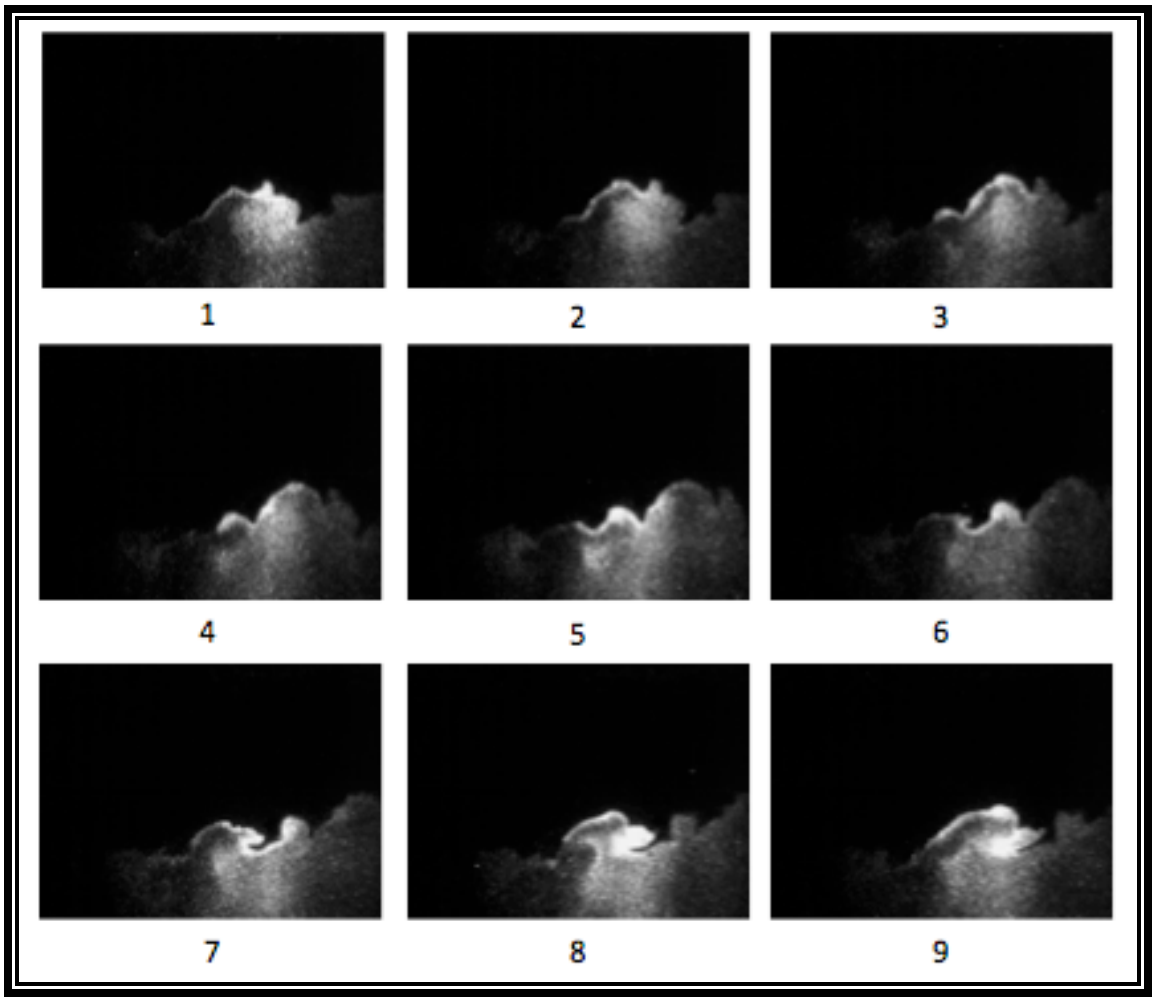

Figure 4.15: Grid 2 Re=32,000 instantaneous frames of flame front wrinkling evolution

The flames at Re=54000 presented a peculiar behavior for this grid. The turbulence parameters were the following: U_{bulk}=45 m/s, u'=18.9 m/s, Da=1.3, Ka=50, Re_T=2647. The turbulence intensity was lower than that for grid 1 at the same Reynolds number conditions. However, grid 2 presented a flame front that shows much more interaction with the turbulence inside the combustor. As shown in Figure 4.16 the instantaneous frame sequence for this flame front wrinkle development shows both the capture of unburned gases due to wrinkle formation and the eventual separation of burned pockets or flamelets from the flame front. In frame 1, one notices a large wrinkle in the center of the image; by frames 2 and 3 this wrinkle has reattached to the main flow and continues to move downstream, while a new wrinkle forms by frame 4.

Similarly to what was seen in the previous grid, the leading edge of the wrinkle bends in a circular fashion eventually capturing and forming a pocket of unburned gases within the burned gas section.

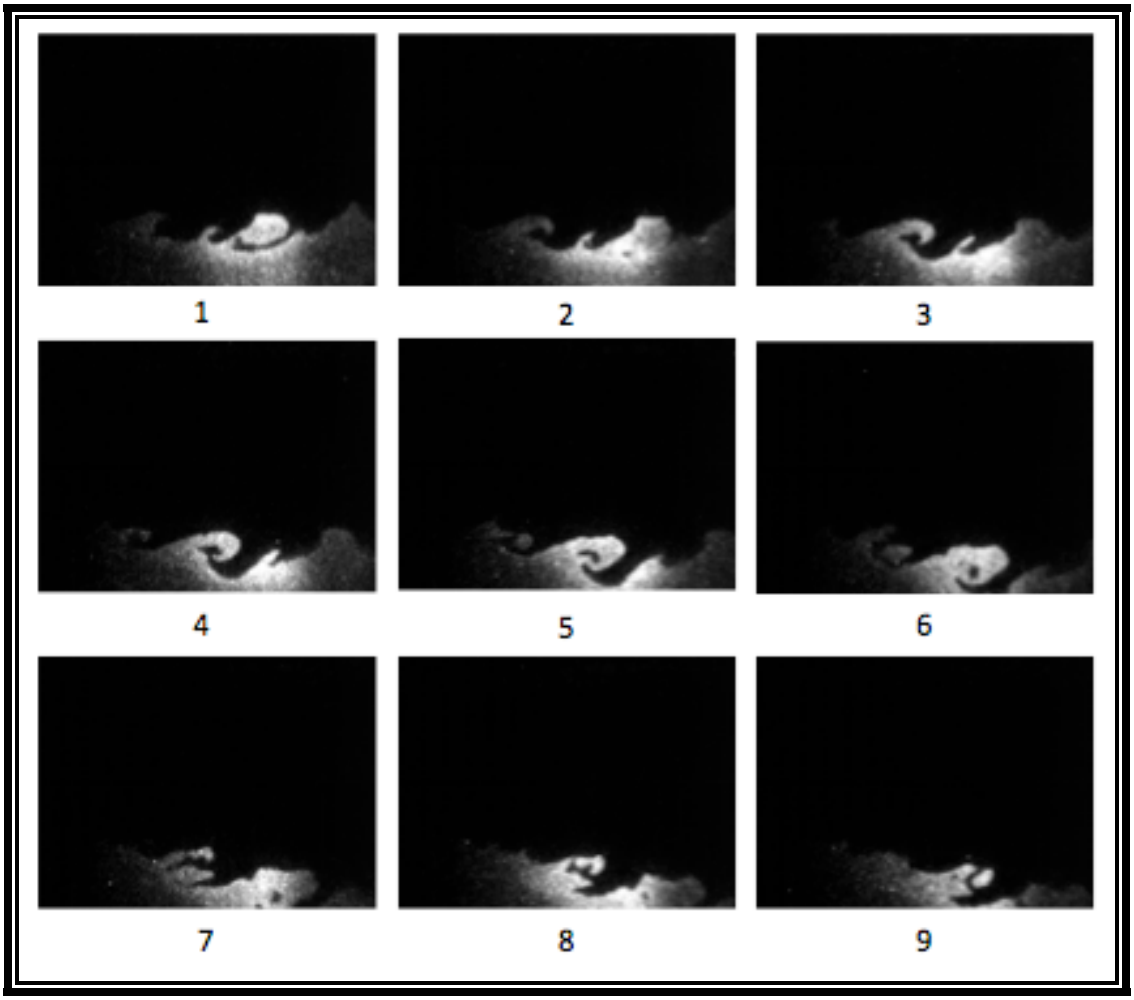

Figure 4.16: Grid 2 Re=64,000 instantaneous frames of flame front wrinkling evolution

The flame front angle change is also evident from the images, which is directly correlated to the bulk velocity of the flow. This angle changes as the flame front flapping occurs. The wrinkling for grid 2 at these conditions is different than that presented for grid 1. Figure 4.17

shows an isolated instantaneous image showing flamelet formation and flame front corrugation at these conditions along with the corresponding binary and outline images.

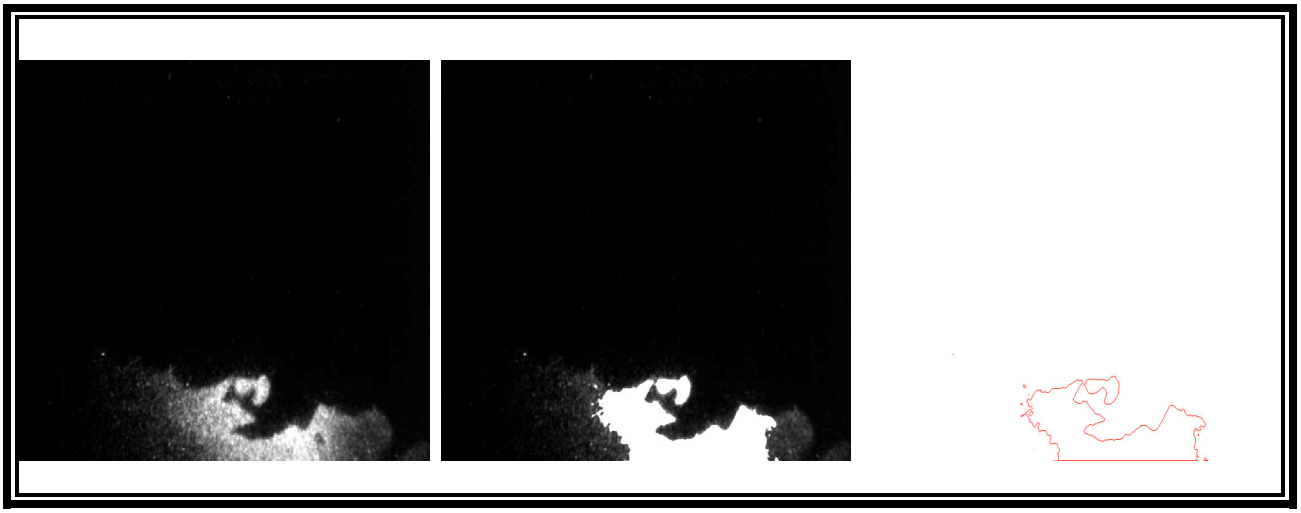

Figure 4.17: Grid 2 Re=64,000 flame front instantaneous frame, binary image, and outline

Taking a closer look at instantaneous frames of the flame front at different times in Figure 4.18, one can see the pockets of unburned gases mentioned before, as well as the burned gas pocket separation from the flame front. Similar to the previous grid, some of this flamelets may eventually rejoin the flame front further downstream while others don't.

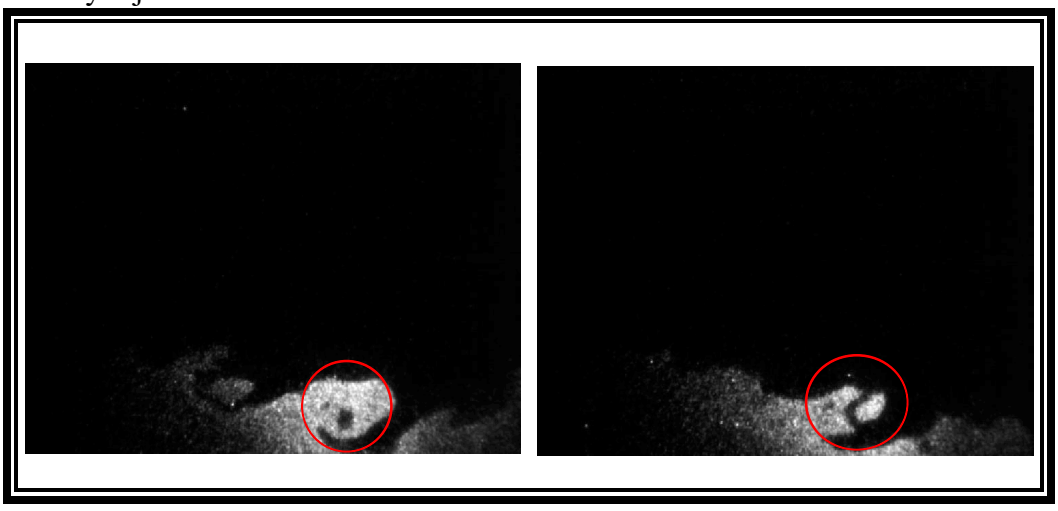

Figure 4.18: Grid 2 Re=64,000 unburned and burned gas pockets along flame front

Grid 3 – 63% blockage ratio and 1.5 mm hole diameter was tested in order to see the effects of changing the blockage ratio at the same hole diameter as grid 1. The behavior of the flame front at the varying Reynolds numbers was different from what was seen in the previous two cases. Velocity fluctuations for grid 3 where 5 and 3 times large than those found in grids 1 and 2 respectively, for this conditions. At Re=15000, flamelet formation was already visible as shown in the instantaneous frame sequence in Figure 4.19.

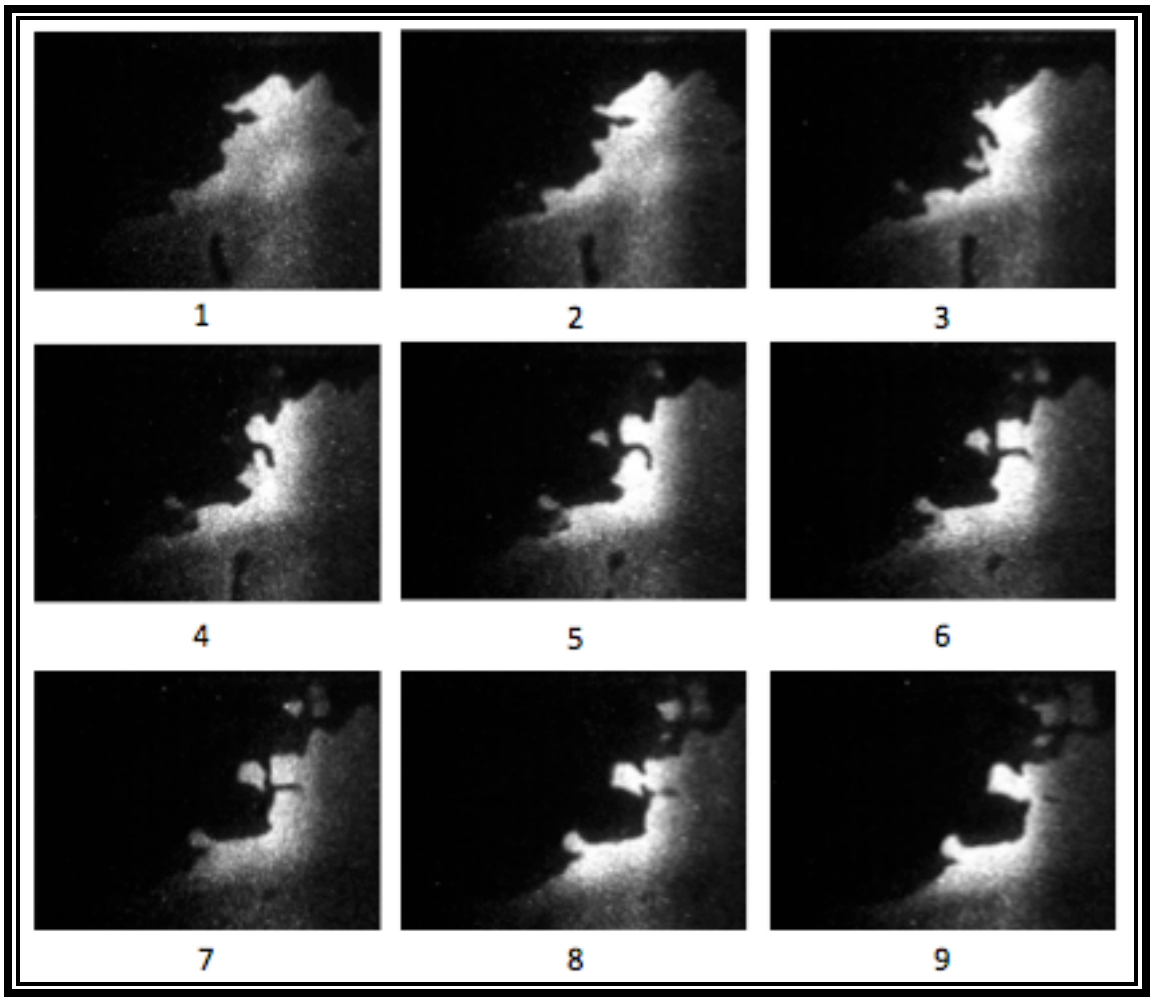

Figure 4.19: Grid 3 Re=15,000 instantaneous frames of flame front wrinkling evolution

Flame front angle changes were constant, leading to the flame front angle with respect to the step edge to change constantly. The turbulence conditions for this grid were the following:

U_{bulk}=10 m/s, u'=5.5 m/s, Da=5.1, Ka=10, Re_T=604. It is important to note how the flamelet appearance occurs at points where the flame front has already "passed through" as it moved further downstream in the combustor. These pockets of burned gases eventually "catch up" to the flame front as seen in frames 7-9 of the figure above. This behavior was not seen in any of the two previous grids. These features are highlighted in Figure 4.20 with red circles. The image on the left shows the pockets of burned gases present behind the flame front, and by the image on the right they blend in the flame front. The sudden formation or apparition of these pockets of burned gas behind the flame front might be attributed to auto-ignition events associated with flammable mixtures near the burned gas region.

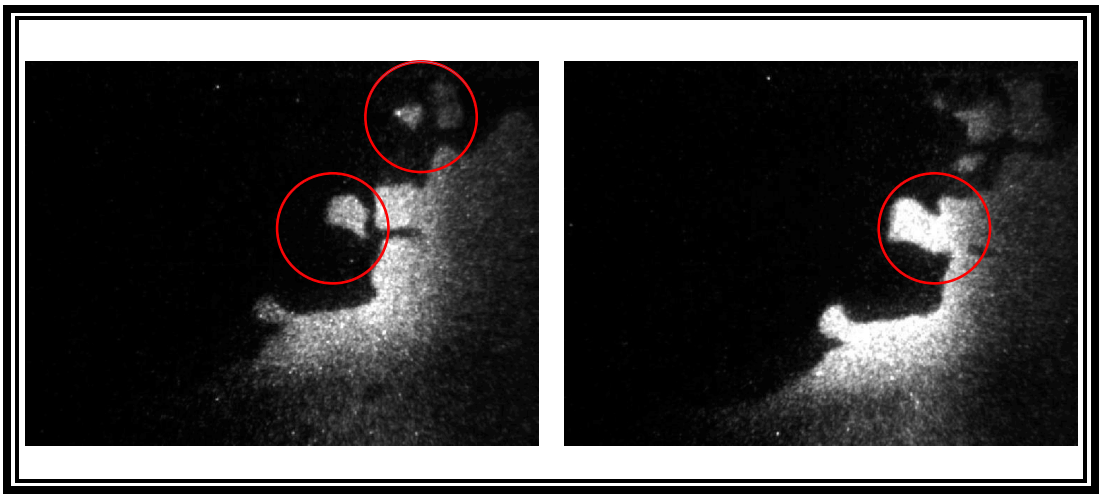

Figure 4.20: Grid 3 Re=15,000 instantaneous frames of burned gas pocket merging

At Re=32000, the conditions encountered were as follows: U_{bulk}=25 m/s, u'=7.5 m/s, Da=4.3, Ka=16.8, Re_T=824. The turbulence intensity was higher than in grid 1. Similar to what was seen at Re=15000, flame flapping is present, changing the flame front angle with respect to the step edge constantly. The flame front progression frame sequence presented in Figure 4.21 for this flame conditions shows the highly turbulent shape of the flame and its burned products branching off from it.

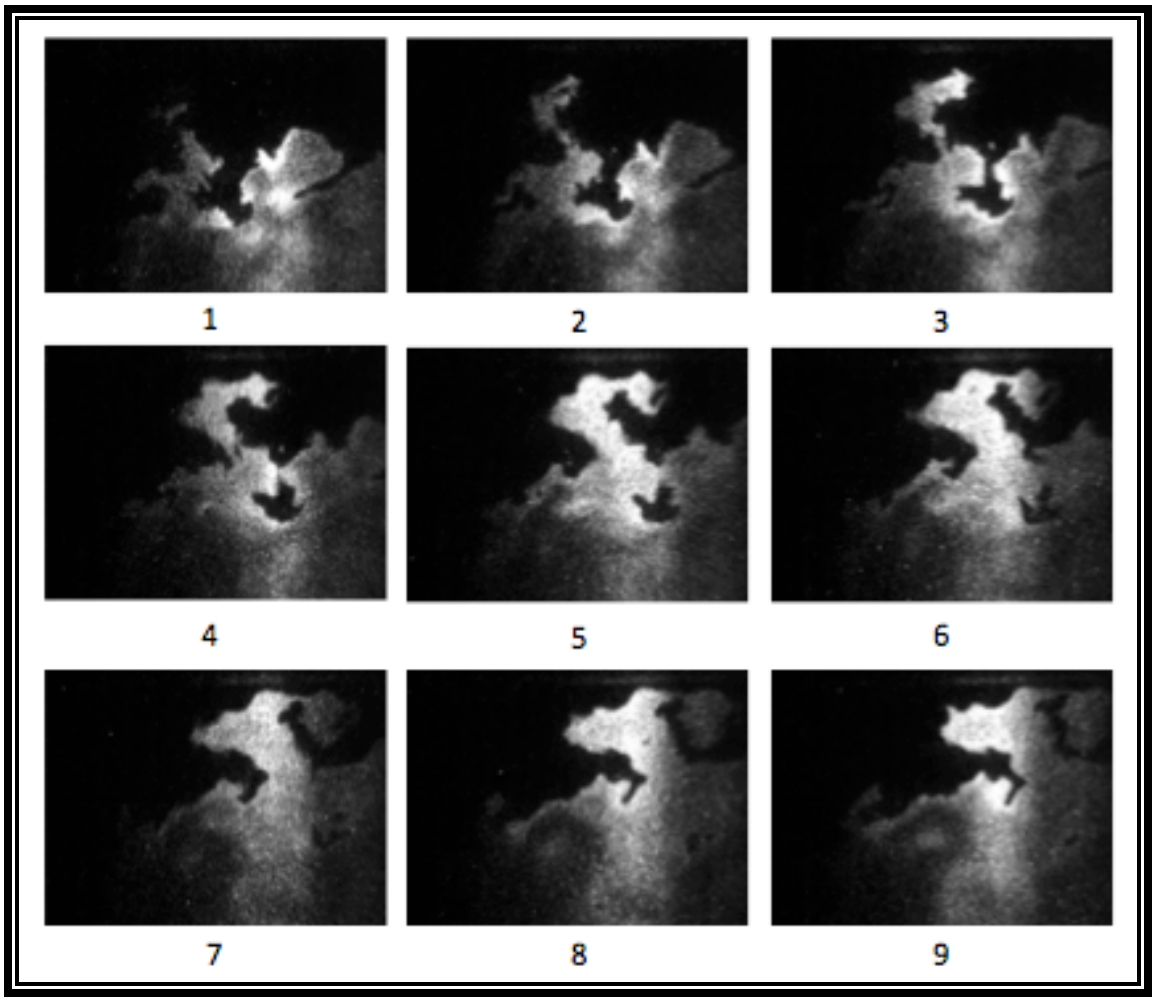

Figure 4.21: Grid 3 Re=32,000 instantaneous frames of flame front wrinkling evolution

In frame 1, we see two main wrinkles separated by a gap in the OH signal due to the presence of unburned mixture. Frames 2 and 3 show the further development of the thinner wrinkle branch and the decrease of unburned gap between the two wrinkles. By frame 4, the gap is closed and the edges of both wrinkles have merged. The pocket of unburned gas retains it shape and gradually reduces its size as we move down frames 5-9. In fact it may be noticed that in frame 7, there is further break up of the unburned gas pocket into two separate pockets of non-symmetrical dimensions, which are then clearly seen in frame 8. This further break up of the unburned gas pocket is an interesting phenomenon, which could indicate an acceleration of the

unburned gas pocket that in turn could be indicative of some sort of local pressure fluctuation happening at that point.

These images show a much more turbulence-influenced flame front as evidenced by the frame sequence. These were perhaps the most turbulent-shaped flame fronts for all the grids and conditions tested. As in previous cases, the time resolution of the study enable the progressive visualization of the formation of pockets of unburned gas trapped by the flame corrugation. These characteristics are isolated and highlighted in Figure 4.22.

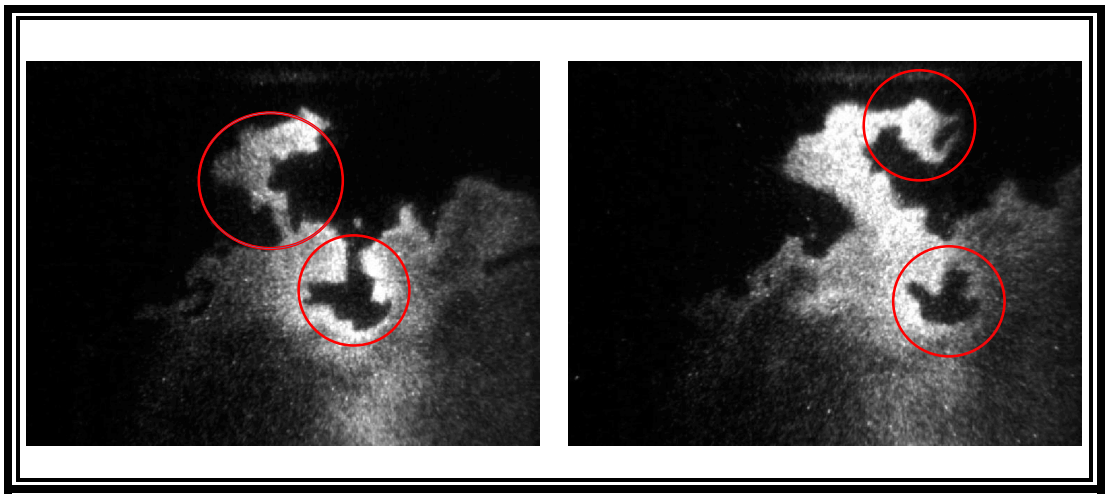

Figure 4.22: Grid 3 Re=32,000 instantaneous frames of unburned gas pocket formation

For reacting flow at Re=64000, the conditions encountered were as follows: U_{bulk}=45 m/s, u'=25.6 m/s, Da=0.9, Ka=90.2, Re_T=2814.. The flame front progression frame sequence presented in Figure 4.23 for this flame conditions shows the highly turbulent shape of the flame as well as the appearance of much smaller separated pockets of burned gas. The number of flamelets around the flame front is significantly higher than those observed for previous grids; the flame front is very irregularly shaped, a result of the flow velocity and turbulence levels. These features are highlighted in Figure 4.24.

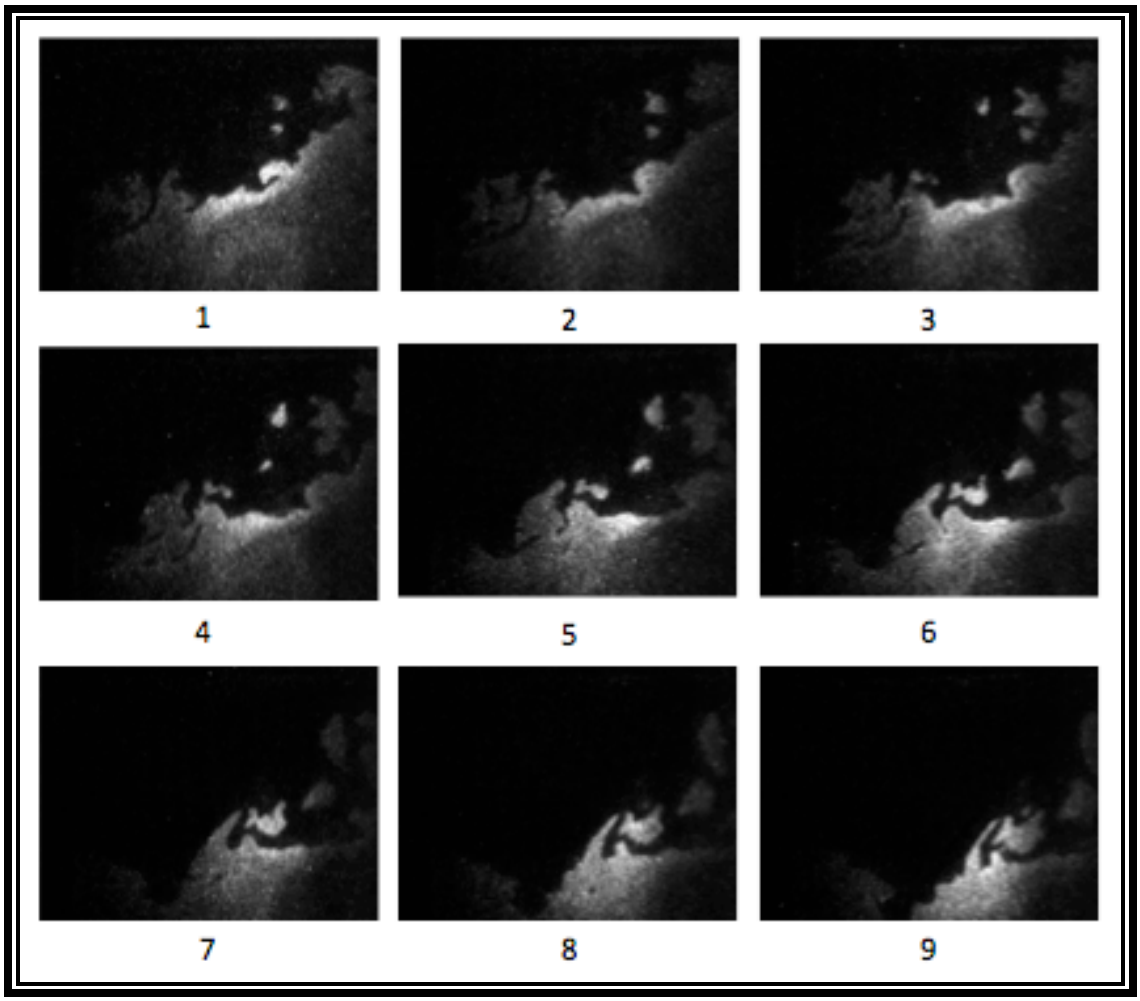

Figure 4.23: Grid 3 Re=64,000 instantaneous frames of flame front wrinkling evolution

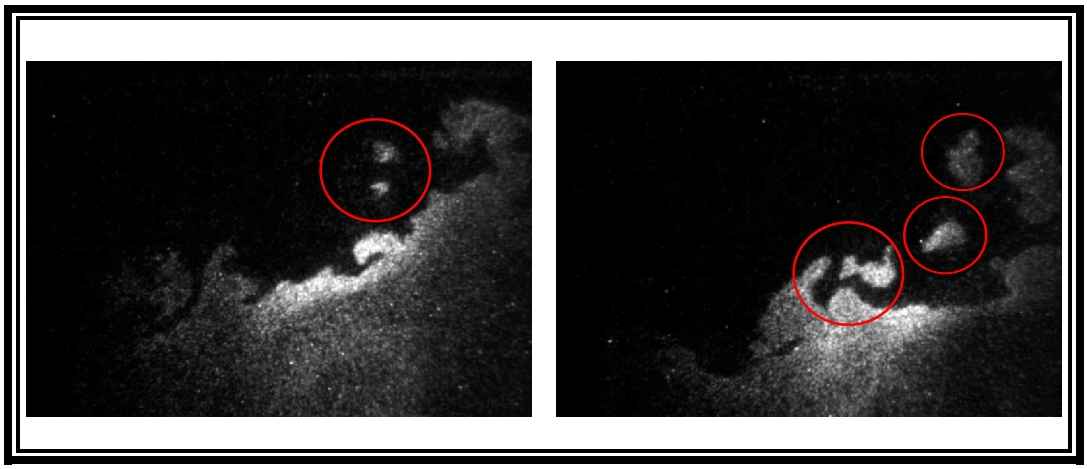

Figure 4.24: Grid 3 Re=64,000 instantaneous frames of burned gas pocket formation

Grid 4 – 63% blockage ratio and 3 mm hole diameter – resulted in the following turbulence conditions for Re=15000: U_{bulk}=10 m/s, u'=2.5 m/s, Da=13.9, Ka=3.4, Re_T=300.5 . It was tested in order to see the effects of changing the blockage ratio at the same hole diameter as Grid 2. The flame front resembles that of Grid 3 instead; suggesting the blockage ratio and thus turbulence intensity u' itself introduces the major characteristics of the flame. In this case, the corrugation of the flame is not as smooth as the one saw in Grid 2. Also, the separation of burned as pockets is visible at this flow conditions, just as it was in Grid 3. These burned gas islands grow in size over time and eventually blend in the flame front as they move downstream. The instantaneous frame sequence presented in Figure 4.25 shows the evolution of these flame characteristics over time, and this flamelet growth is isolated and highlighted in Figure 4.26.

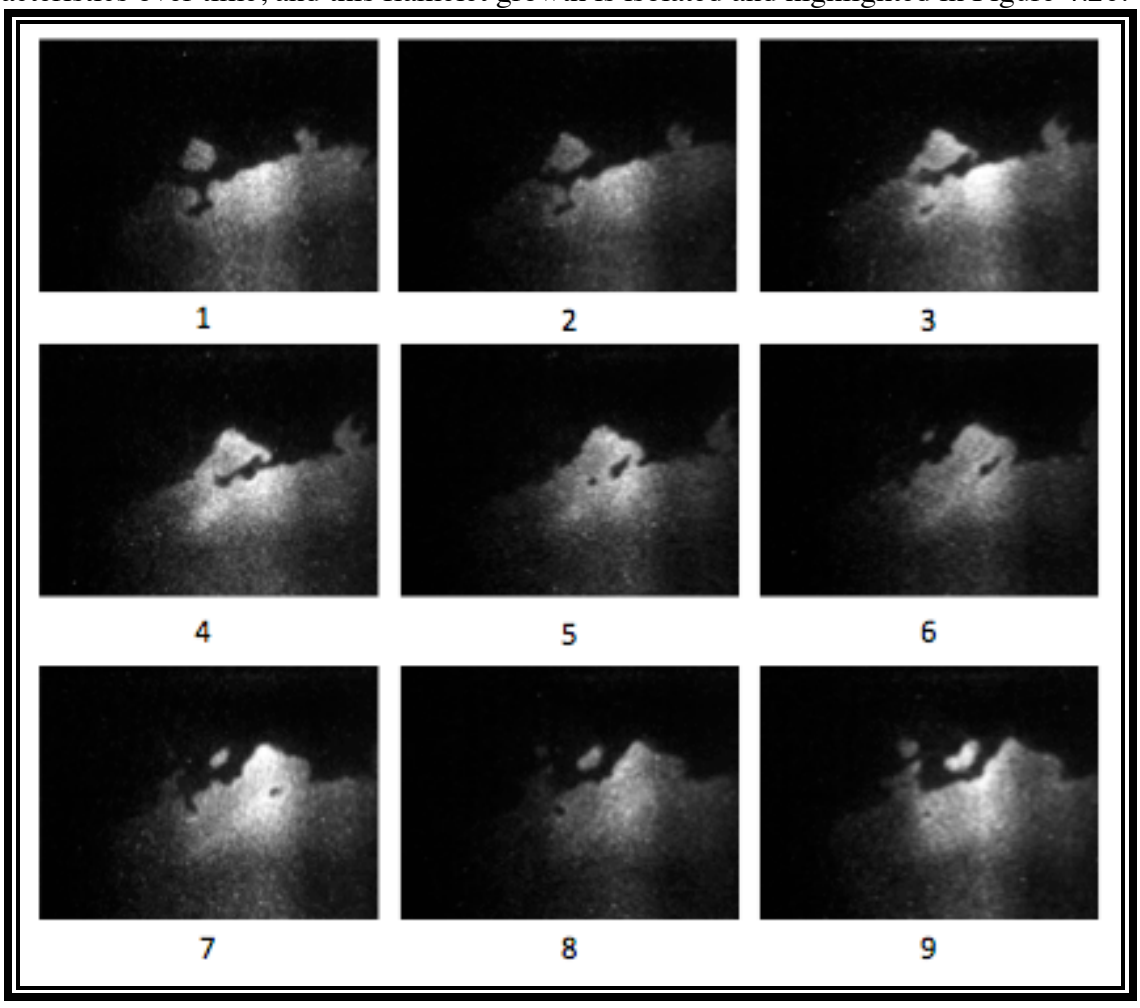

Figure 4.25: Grid 4 Re=15,000 instantaneous frames of flame front wrinkling evolution

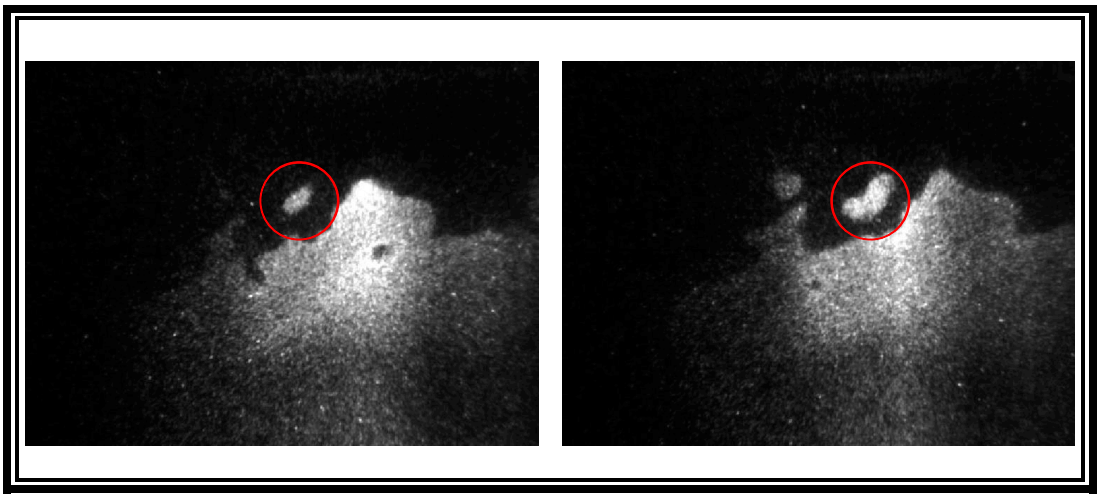

Figure 4.26: Grid 4 Re=15,000 instantaneous frames of burned gas pocket formation

At Re=32000, the conditions encountered were as follows: U_{bulk}=25 m/s, u'=11 m/s, Da=1.8, Ka=24.6, Re_T=1315. This flames had a similar behavior to those in grid 3 in the sense that flamelet appearance was behind the flame front, eventually catching up and blending in further downstream. This flamelet formation is evident in frames 4-9 of the flame front development image sequence presented in Figure 4.27. These flames had an irregular shape as seen in the instantaneous frames. One thing to note here is the peculiar way that the burned pocket presented in the sequence grew over time. From frames 4-6 it seemed to follow the behavior we have been discussing for the rest of the grids. However frames 7-9 show an irregular growth mechanism, where unburned mixture gaps are evident even when the flamelet is growing. This could be indicative of mixing variations present in the flames or local extinction points at these conditions. This would also address the different intensities in the OH signals that are noticeable form frame to frame. Figure 4.28 highlights the flamelet feature that was just discussed.

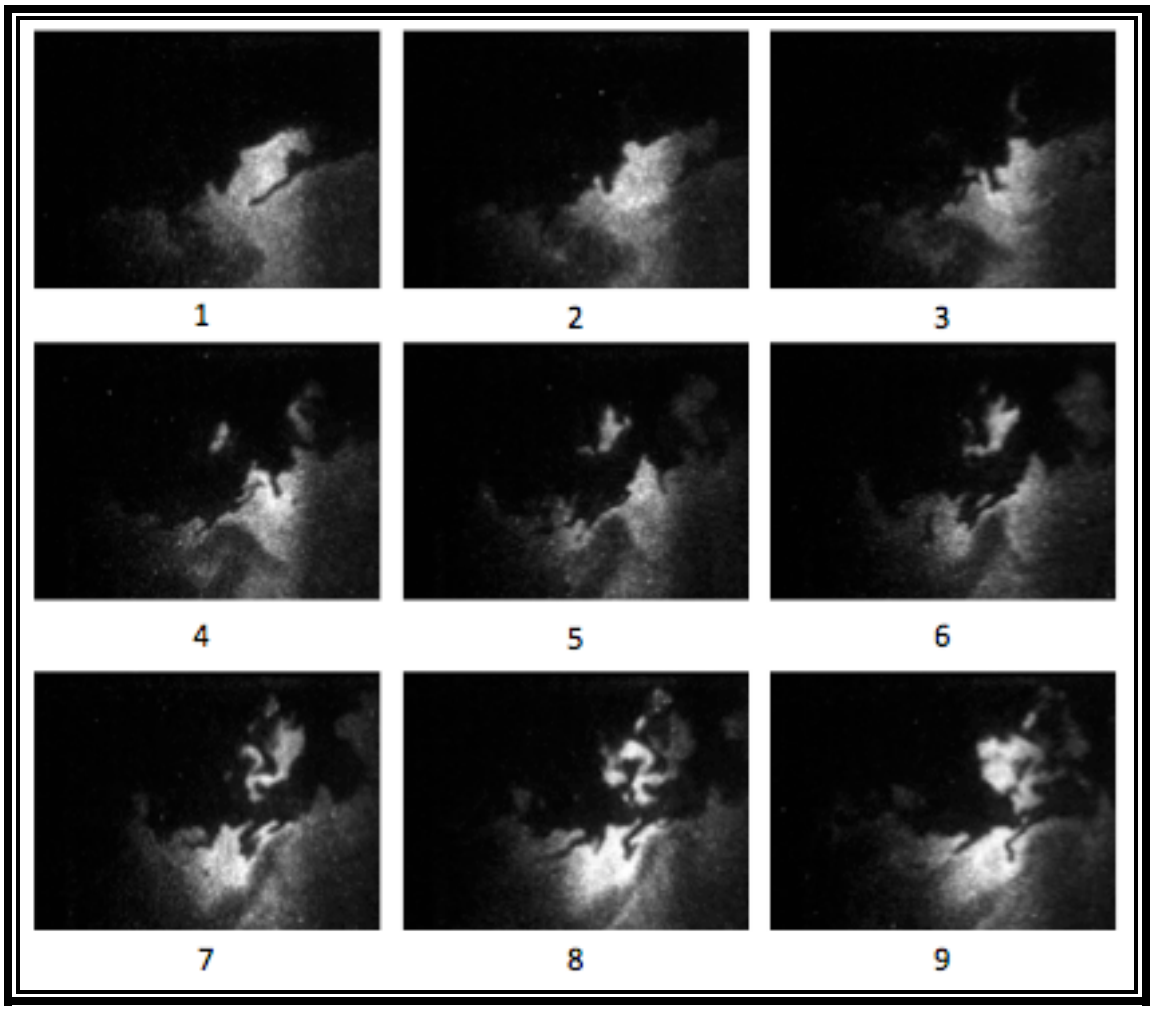

Figure 4.27: Grid 4 Re=32,000 instantaneous frames of flame front wrinkling evolution

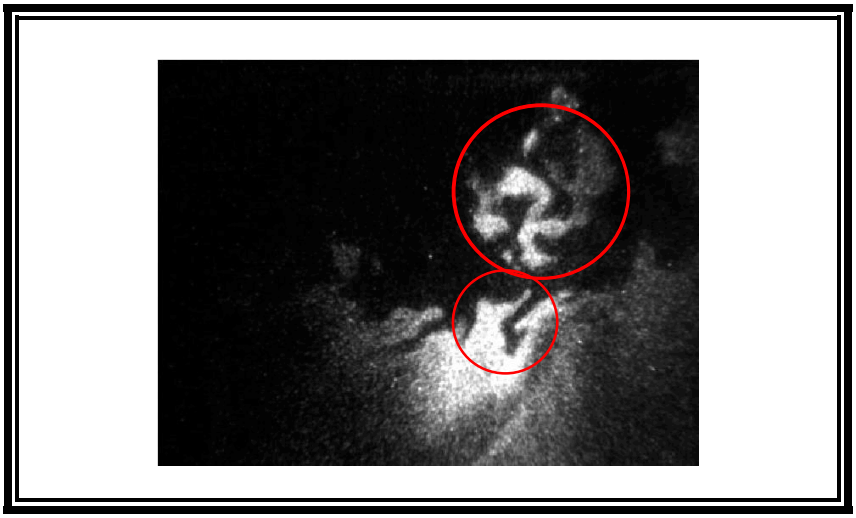

Figure 4.28: Grid 4 Re=32,000 instantaneous frames of burned gas pocket formation

At Re=54000, the conditions encountered were as follows: U_{bulk}=25 m/s, u'=27.6 m/s, Da=0.8, Ka=96, Re_T=3315. An irregular shaped flame front may be seen, with rough edges and contour attributed to local extinction and re-ignition processes. The instantaneous frame sequence presented in Figure 4.29. Burned gas pockets of a couple of pixels in size show up and grow as seen in frames 2, 3, 7, and 8. These small pockets merge with the flame front at some points and create the thin branches on the wrinkles. Entrapment of unburned gasses within the burned gases much smaller in size and more irregular in their shapes than in previous cases as seen in frames 3, 5, and 9. Figure 4.30 highlights these features.

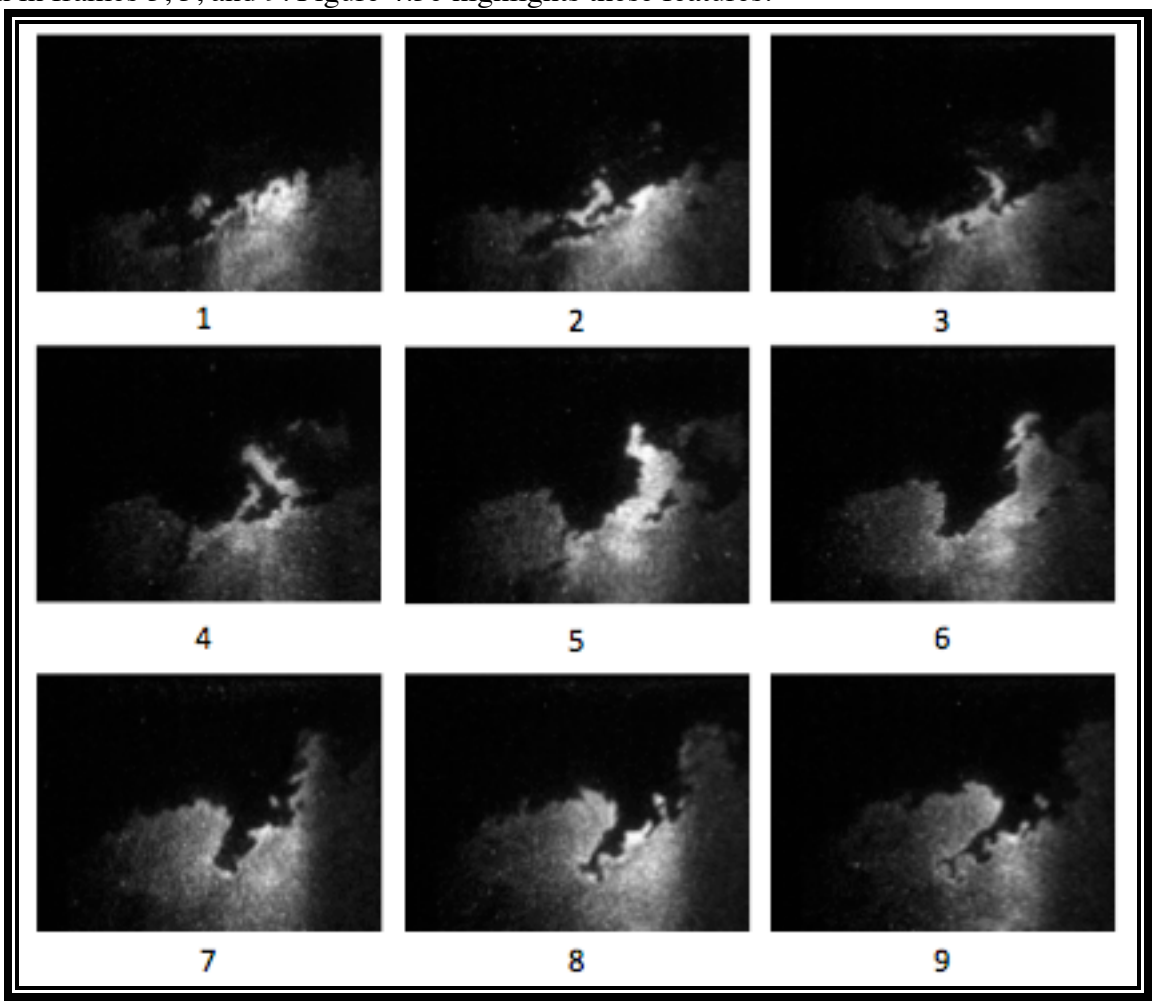

Figure 4.29: Grid 4 Re=54,000 instantaneous frames of flame front wrinkling evolution

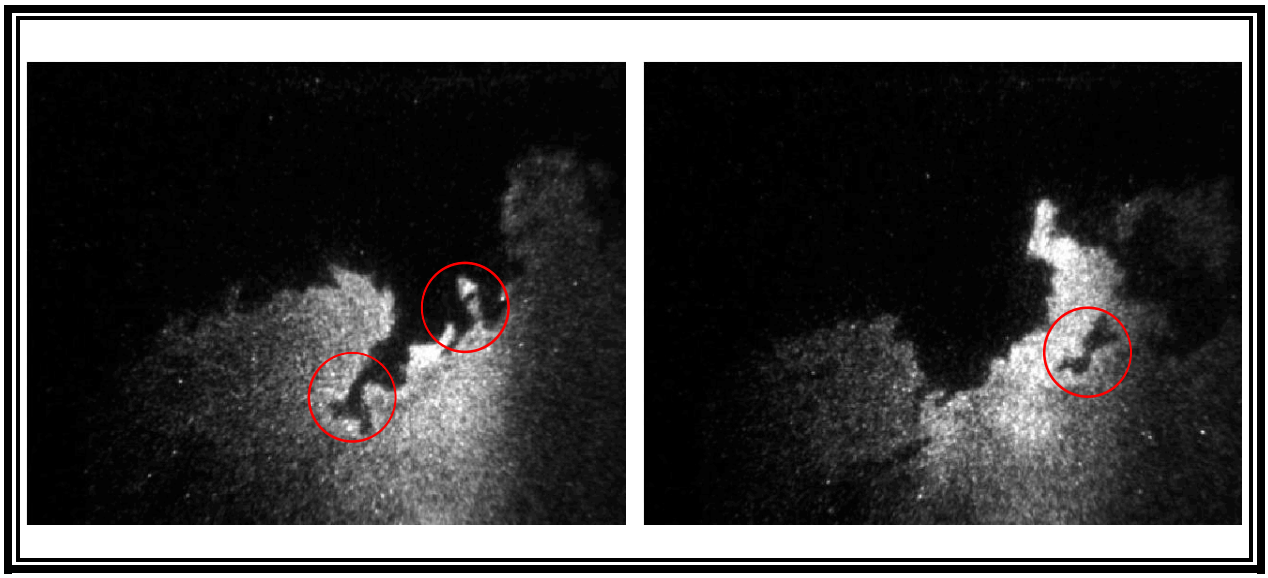

Figure 4.30: Grid 4 Re=64,000 instantaneous frames of burned and unburned gas pocket formation

4.3 CH LIF

In order to have a more accurate location of the flame front position and characteristics, CH-PLIF was attempted with the same pump/dye laser setup used for the OH-PLIF. It has already been established in previous sections that CH has the primary advantage over OH in that its distribution within a flame corresponds well to the region of peak heat release, making it a more suitable flame front tracer than OH. However, CH exists in very low concentrations making it difficult to detect and avoid fluorescence signal interference.

CH-PLIF has generally been conducted using the A-X ~430 nm and B-X ~390 nm excitation wavelengths by different researchers. These wavelengths cannot be reached with a common YAG pump/dye laser setup as the one available in the university. Recently, Carter et al [43] [44] demonstrated the detection of CH in hydrocarbon flames at a rate up to 10kHz using the C-X~314 nm excitation band. This band falls within the tuning range of a YAG pumped dye laser as the ones commonly used for OH detection. Even though this CH band had been reported since the 1950s, it had not been the choice among researchers due to the lower emission energy levels and overlapping with OH excitation bands. Nonetheless, Carter's group reported detection of CH in turbulent flames in a Bunsen burner with energies as low as 0.2 mJ/pulse.

As it was explained in the methodology section, DCM in ethanol with a concentration of 0.5 g/L was used to tune the dye laser to the excitation wavelength at 314.4 nm. When pumped at 532 nm, DCM has a conversion efficiency similar to that of Rhodamine 6G of ~30%, with a tuning range of 607-663 nm and a peak energy at 640nm frequency doubled wavelengths. The grating and other crystal elements of the dye laser yield a tuning range of 367 – 769 nm for the current laser system, hence making it possible to work with DCM to test CH excitation.

The acquisition system consisted of the same setup as for the OH-LIF. Fluorescence was detected with a two-stage intensifier equipped with a Cerco 100-mm *f*/2.8 lens and coupled to a high-speed camera. Given the Nd:YAG pump laser power limitations of 20 W @ 10kHz, the UV pulse power requirements of ≥0.2 mJ/pulse were only met at frequencies <6000 Hz. Several modifications were done trying to increase power conversion efficiency in the oscillator and amplifier of the dye laser in order to achieve higher UV pulse power output, however it was not possible to do so beyond that frequency. Figure 4.31 shows the 314 nm UV output power curve for the laser at different wavelengths. This posed the first obstacle for CH detection with the laser system, by limiting the time resolution of the measurement to 5 kHz.

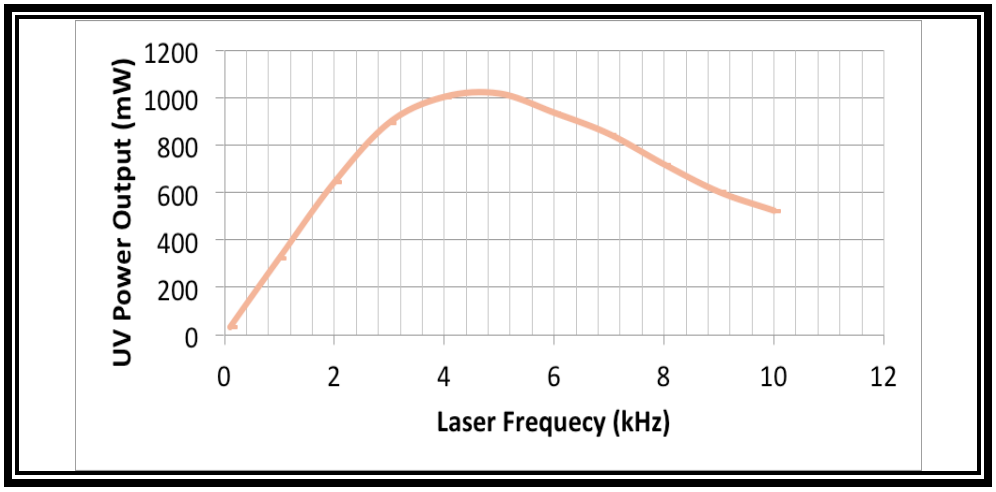

Figure 4.31: Laser UV power output

An initial validation study was conducted by testing the CH detection setup in a laminar flame stabilized in Bunsen burner as reported in literature. Figure 4.32 shows two averaged image samples of images taken at the 5kHz trigger rate mentioned before. These images show both independent excitation of CH at 314.44 nm as well as an overlap of CH-OH at a 314.39 nm excitation wavelength. These results are consistent with the data presented in literature.

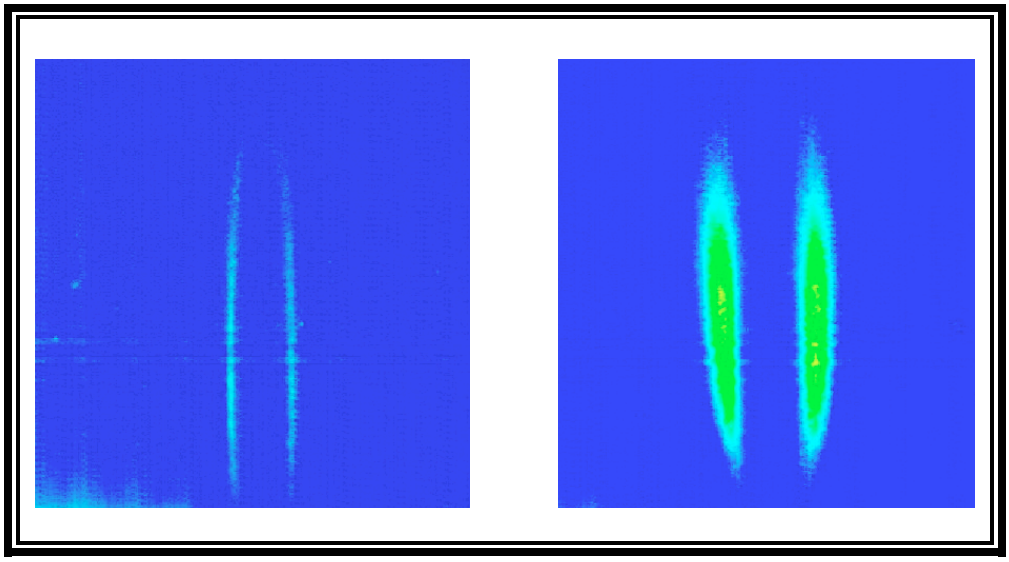

Figure 4.32: CH detection on a Bunsen burner laminar flame at 314.44 nm (left) and 314.39 nm (right)

A wavelength scan was conducted to see which wavelength resulted in the highest CH concentration detection. Once this wavelength was identified with the burner, it was recorded in the dye laser controller so that it could be used during the combustor experiments. Carter et al provided the absorption wavelengths and corresponding signals they acquired, thus these were used as a base for the scan conducted. Figure 4.33 presents samples of the scan conducted, and it may be seen that the absorption at 314.443 nm yielded the highest signal; therefore this was the chosen wavelength for the combustor studies.

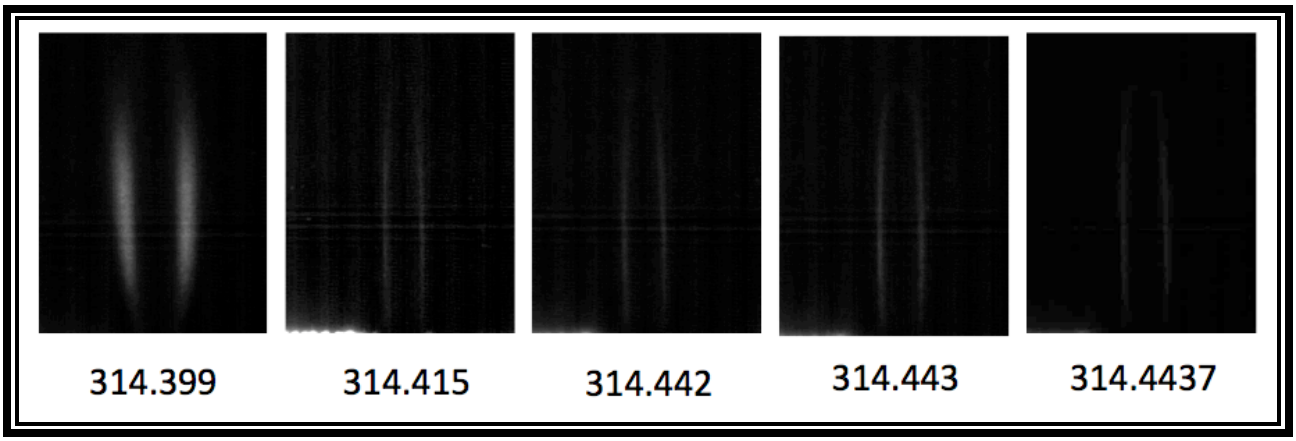

Figure 4.33: Absorption wavelength scan on Bunsen burner

It was previously mentioned that one of the difficulties with the detection of the CH radical at the C-X band is the fact that it is a diagonal band, meaning that the fluorescence is emitted at a wavelength very close to that of the absorption. This poses no major problems in burner settings as any black body in the background may absorb the laser sheet light scattering. The introduction of the laser sheet into the stainless steel combustor however resulted in laser light scattering, which introduced significant noise in the pictures. These pictures were post-processed by removing a sample background image, with the laser on, from the images for the flames, however the noise is still visible as the intensifier magnification effects add noise to the image as well. The other factor affecting the detection scheme in a negative way was the UV power availability at 314 nm, which was limited to 0.2 mJ/pulse at 5kHz. The laser beam path however went through additional losses in optics and the combustor windows. This means the power delivered at the combustion gas location was <0.2 mJ/pulse.

The added noise, which was also attenuated by darkening the combustor surfaces, coupled with the low laser power and low CH signal made the detection difficult even at the lower Re conditions, and practically impossible for Re ≥ 32000. For this reason only the results for the grids at Re=15000 will be presented in this work. The images were post-processed in an effort to remove as much noise as possible, and frames with weaker signals were adjusted to highlight the CH layer. It will obvious from the images that will be presented in this section that,

for the majority, level noises remain high even after the background subtraction. This is attributed to small fluctuations in light intensity, which may be a problem associated with the intensifier hardware.

Figure 4.34 shows a sequence of instantaneous frames for the CH emission during the Re=15000 conditions. This sequence corresponds to a total run time of 1.8 ms at 0.2 ms time intervals. It must be noted that image colors are reversed in this case for clarity purposes, meaning that black represents the CH layer, while the white background represents the unburned gases or burned gases that are not part of the CH layer. The black spots at the bottom of the images are part of the reflection of the light sheet on the combustor floor.

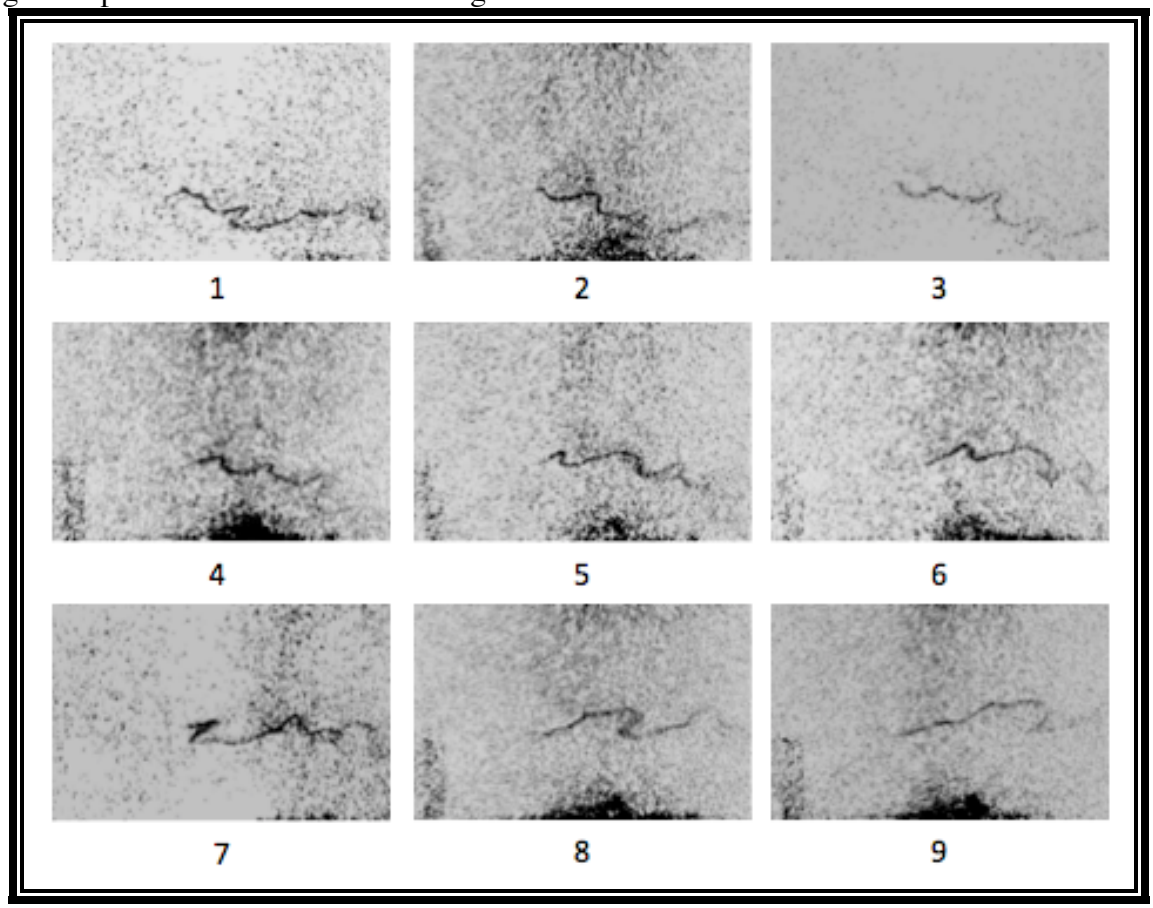

Figure 4.34: Grid 1 Re=15,000 instantaneous CH frames of flame front wrinkling evolution

Even though the CH signal is low, there wrinkling of the flame is still visible in the progression. As with the OH signal for this grid, large scale flame front wrinkling is the

dominating effect as seen from the CH frames. Frames 1,3, and 5 do show some smaller wrinkle formation, however the overall contour of the layer is smooth as it was with OH.

Figure 4.35 shows the instantaneous frame sequence progression for Grid 2 over a span of 1.2 ms. The formation of elongated wrinkles is seen from the CH profiles. The wave-like wrinkles elongate as they travel downstream of the combustor.

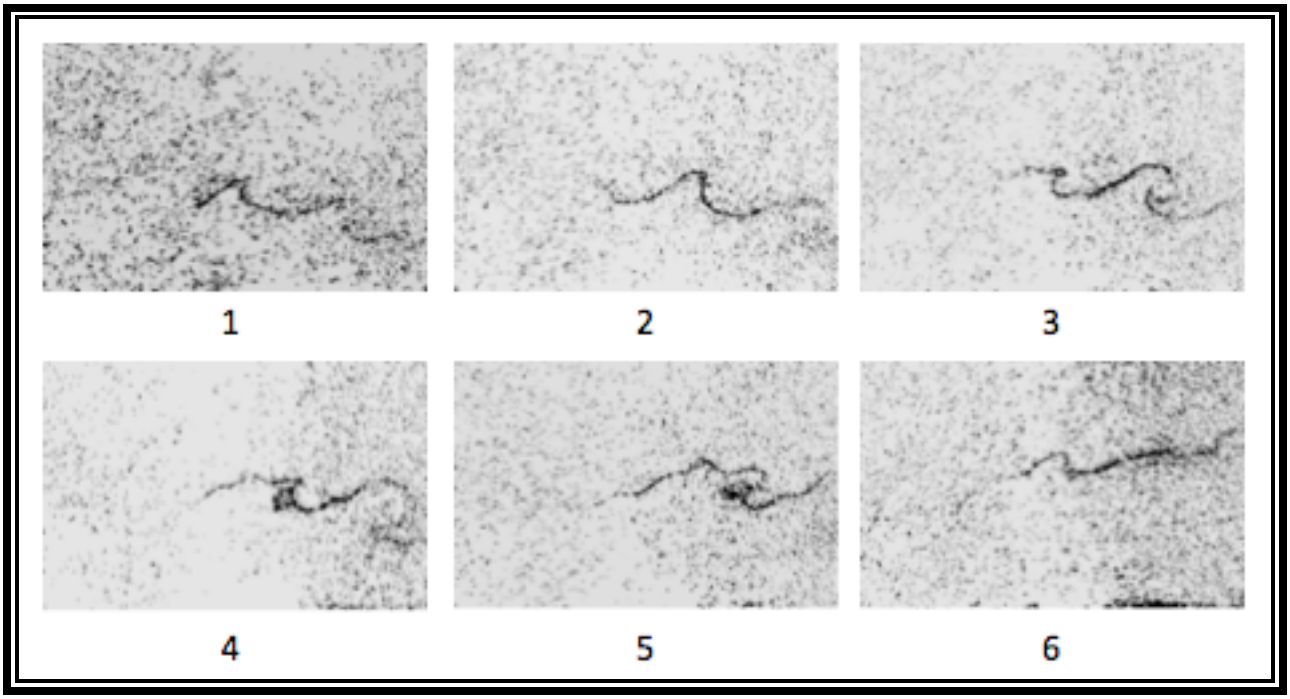

Figure 4.35: Grid 2 Re=15,000 instantaneous CH frames of flame front wrinkling evolution

Figure 4.36 shows the instantaneous frame sequence progression for Grid 3 over a span of 1.8 ms. As it was the case with the OH images, this grid showed the most noticeable effects of turbulence interactions with the flame front. The pockets of burned gases (flamelets) in the unburned mixture show up on the CH profiles as well. Frames 3-5 show the progressive growth of the flamelet, while frame 6 shows the reattachment of the pocket to the flame front.

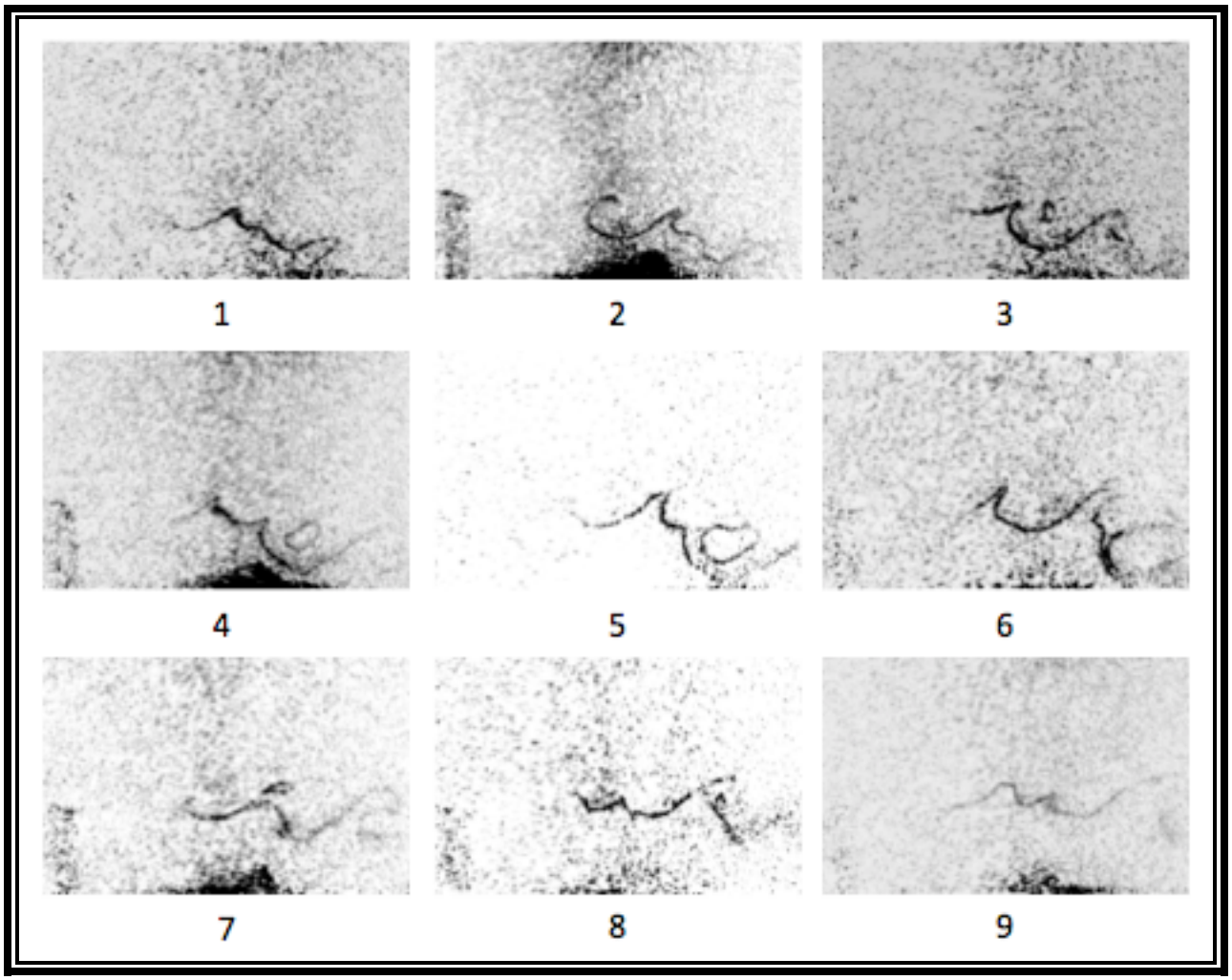

Figure 4.36: Grid 3 Re=15,000 instantaneous CH frames of flame front wrinkling evolution

Grid 4 exhibited the weakest CH emission out of all the grids. However the progression is presented in Figure 4.37. Frames 1-4 show a steady flame front with only minor wrinkling. Frames 6-9 show evidence of wrinkle development similar to those of Grids 1 and 2.

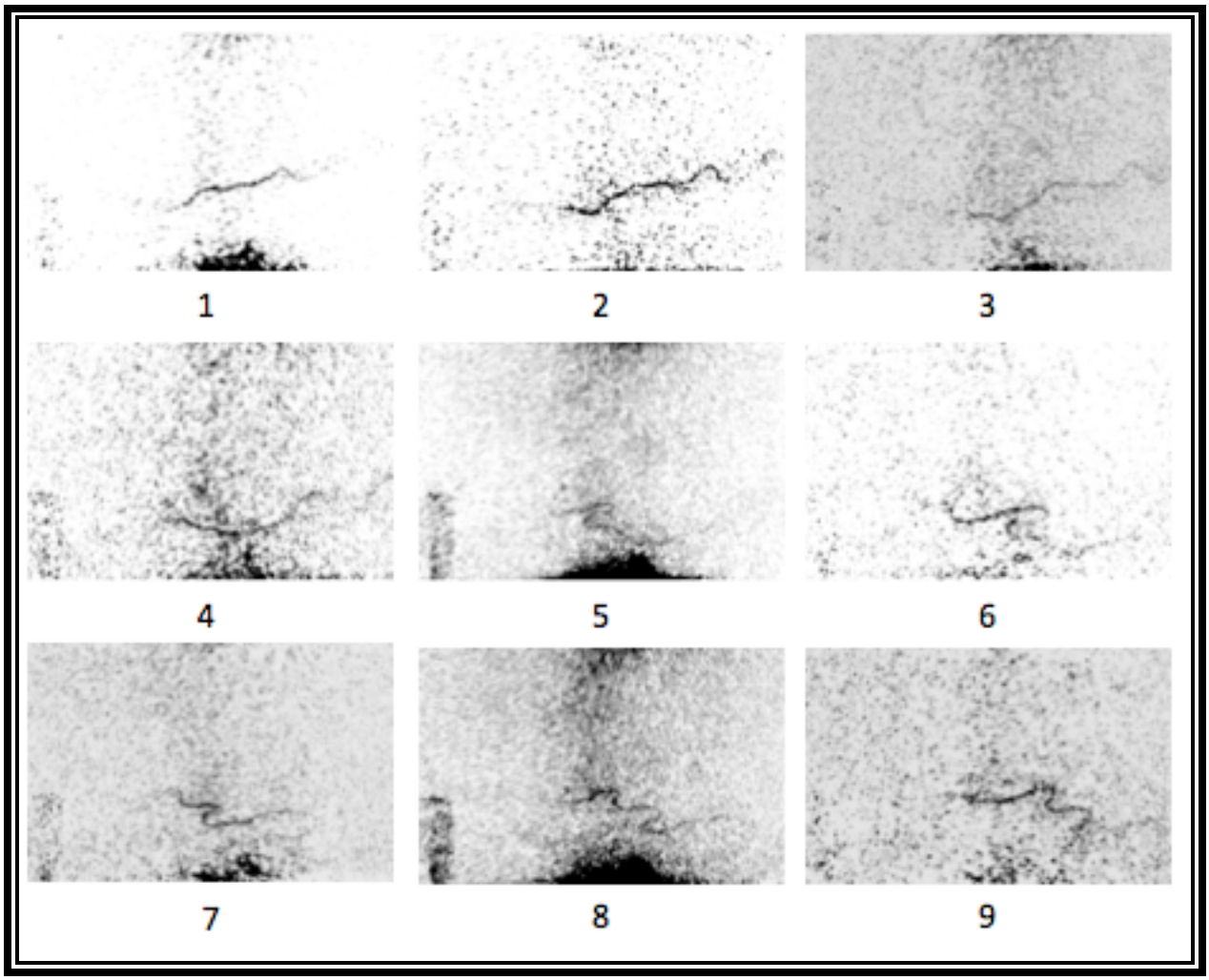

Figure 4.37: Grid 4 Re=15,000 instantaneous CH frames of flame front wrinkling evolution

4.3 Turbulent Flame Speed

Since, the CH acquisition technique needs further refinement, OH images were used for global flame speed estimations for the different conditions. Even though OH-PLIF does not accurately portray the flame front location, several groups have used OH-LIF images for flame speed estimations [18][58][59].

In OH-PLIF there is generally a rise in concentration of CH along the flame front, hence the common methodology used is to locate the locations with highest OH intensity and fit a profile line on these.

In this case, an average image was gathered form the OH data, from which maximum concentration points were detected. Figure 4.35 shows a sample image of an obtained OH average image with the overlaid maximum concentration points. From these points of maximum OH signal, the contour for maximum CH signals may be obtained.

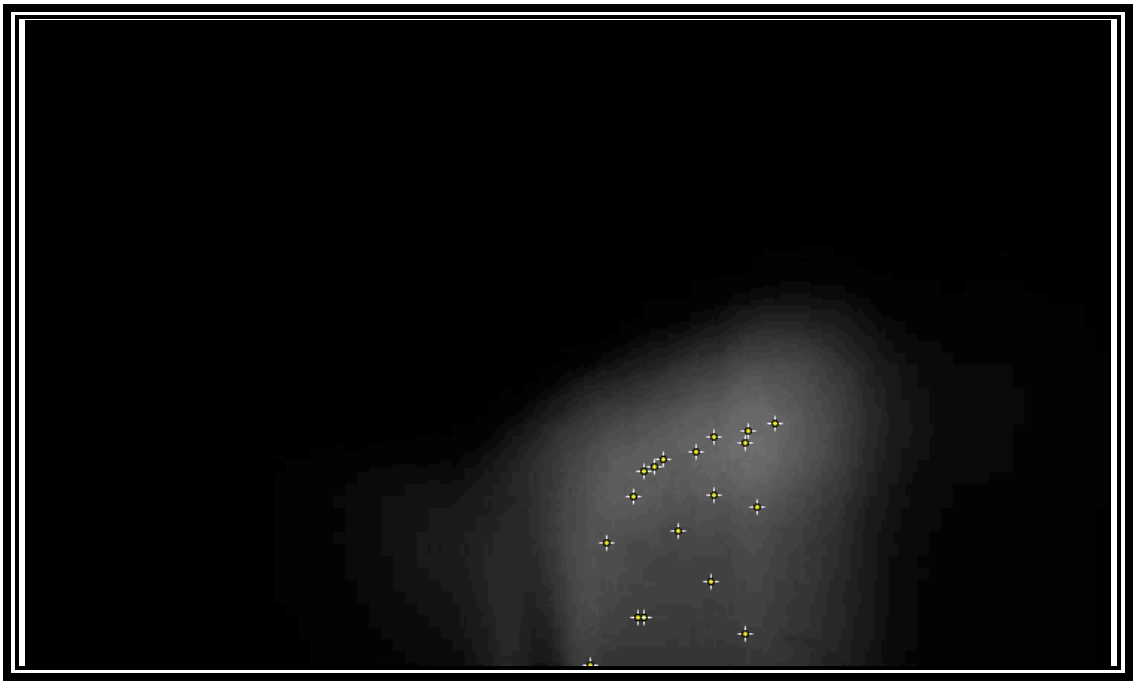

Figure 4.35: OH image mean with maximum intensity points highlighted – location of average flame front area

For this study, turbulent flame speeds were estimated using Damkholer's mass continuity approach [18][61]. This assumes an instantaneous flame front with flame surface area A_T propagating locally with a laminar burning velocity S_L into the unburned mixture. On the other hand there is a mean flame front of surface area A propagating with turbulent velocity S_T. Figure 4.36 shows a typical illustration of the scenario, for which mass conservation and assumption of equal densities leads to [18][61]:

$$\dot{m} = \rho_o A_o u_o = pA_T s_L = pA_T s_L$$

$$\frac{s_T}{s_L} = \frac{A_T}{A}$$

$$s_T = \frac{A_o u_o}{A}$$

where A_o and u_o represent the area and bulk flow velocity at the inlet of the combustor. In this case, the OH concentration profile provided the mean surface area A. It is important to note that this is one of the available methods for flame speed estimation, however other options are available such as the cone angle method or fractal dimension analysis. The continuity method has been proven to provide similar results of the cone angle method [60] and reduces the complexity of the fractal method [18].

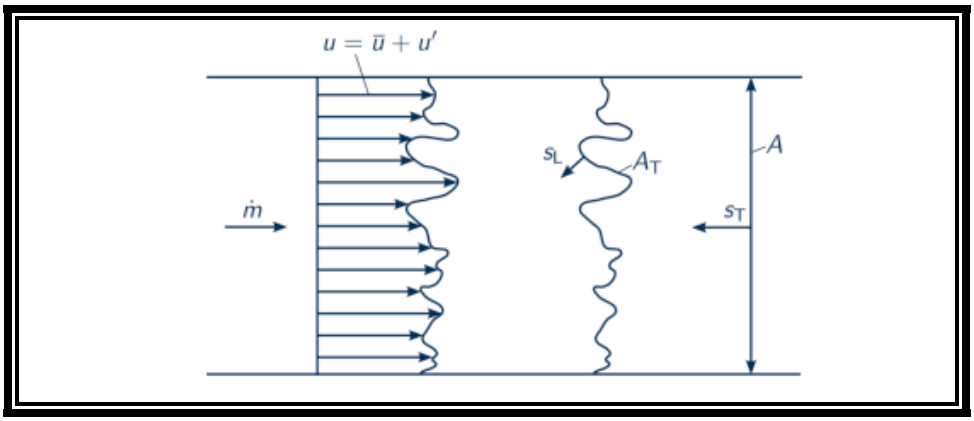

Figure 4.36: Idealized steady premixed flame in a duct. [61]

Based on the resulting turbulent flame speeds, the following trends were observed for the different flames. In general, turbulence effects are presented in the form of s_T/s_L vs u'/s_L. The dimensionless ratio s_T/s_L is a number representative of a percentage increase in burning velocity for a turbulent flame wen compared to a laminar flame. Given the test conditions of constant pressure, temperature, and equivalence ratio, laminar flame speed was maintained constant for all the experiments.

Results graphed in Figure 4.37 shows that the ratio of s_T/s_L increases as the u'/s_L ratio increases. This increasing flame speed rate ratio can therefore be considered a function of Re and

u ‘, which in the case of this study are a direct function of flow rate increase and grid blockage ratio respectively. Increasing the Re has two main effects; it increases the u’ value as shown by the data gathered by the PIV, and increases flow velocity. As it was seen in the OH and CH profiles, the general trend was that higher Re, and thus u’, values resulted in a higher level of flame front wrinkling. Given that flame wrinkling will tend to increase flame front area, a higher turbulent flame speed is expected for increasing Re number conditions. For grids with the same hole diameter, specifically 3 mm, the relationship between flame speed ratios and u'/s_L seems to follow more of a linear relationship (Figure 4.37) as opposed to those grids with 1.5 mm dia holes. The latter show an asymptotic behavior as the value of u'/s_L increases as seen in Figure 4.37

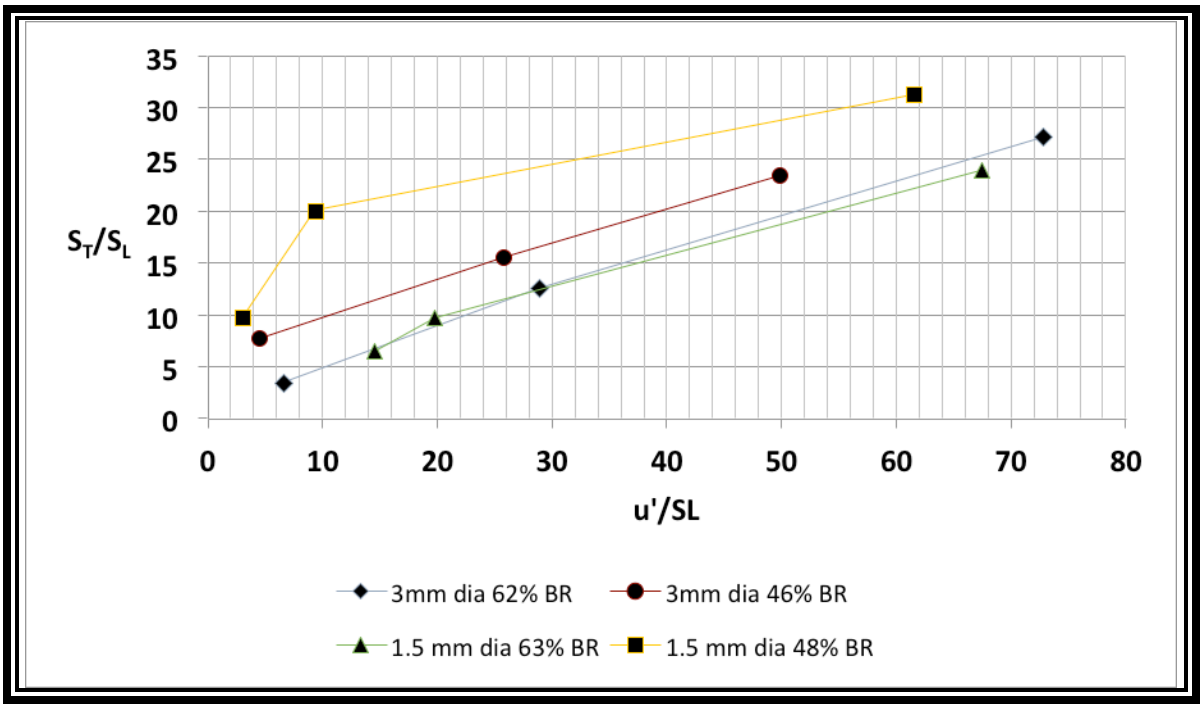

Figure 4.37: Burning velocity diagram for grids with 3 mm dia. holes

This asymptotic behavior has been reported in literature as “bending” [18][60][61] of the curve which is a tendency in the higher u’ $/s_L$ region that has been known and is interpreted as being the effect of factors such as flame stretch in highly turbulent flows [59]. The asymptotic

behavior of the flames at the higher flow rates may offer an explanation to the difficulties of maintaining the flames lit at and beyond Re>64000. The rise of flow velocity (hence u'/S_L) beyond a certain point may lead to local extinctions in the flame, which could cause the combustion to cease. What this means, is that the turbulence stops enhancing the combustion and introduces instabilities in the flame. It is difficult to determine whether pre-existing instability effects in the flame or those introduced by the high turbulence levels are responsible for flame extinction. An intermediate Re number condition between 32000 and 64000 would be useful to understand if this is the trend followed.

Another observation in the data was that the grids with the 46% blockage ratio, which had the larger length scale measurements in the flow, resulted in higher burning ratios for the lower values of u'/s_L <30. While the grids with blockage ratio 63% resulted in higher burning ratios at u'/s_L>30. This could indicate that the larger length scales in the flow aid the combustion process at lower u' values, however as these are increased, smaller scales have a greater effect in increasing the burning velocity.

Chapter 5: Summary, Conclusions, and Future Work

The improvement of optical combustion diagnostics systems has opened new possibilities for researchers to explore combustion processes. This work sought to capture flame front characteristics for flames with a given set of inlet turbulent conditions at a stepped combustor. The intent of the work was to generate time resolved experimental data for potential computational model simulations.

Planar induced fluorescence experiments were conducted to visualize the flame front characteristics of the reacting flows under highly turbulent conditions over a backward facing step combustor. An optically accessible combustion system, which enables the use of the optical laser-based combustion diagnostic techniques, was developed throughout the course of the project. These tests served as combustor operation validation and integration with the laser systems at the Center for Space Exploration Technology Research.

Air-methane reacting flows were tested at atmospheric pressure and temperature, and a constant equivalence ratio of 1. Thus, the project consisted in the variation of flow length scales (L_T) and turbulence velocity fluctuations (u'). Flow length scales were varied through the use of turbulence generating grids of blockage ratios of 46% and 63% and hole diameters of 1.5 and 3 mm. Velocity fluctuations were varied through the grid blockage ratio and the increase of Reynolds numbers based on step height ranging from 15000, 32000, and 64000. Turbulence parameters were measured at the combustor step using Particle Image Velocimetry. These parameters including velocity fluctuations (u') and integral flow length scales (L_T) along with estimated flame parameters resulted in flames that are located well within the thin reaction zones of the Peters-modified Borghi diagram for premixed turbulent combustion. Turbulence parameters were obtained through the data gathered by the PIV system. Flame parameters were calculated, through the use of the CHEMKIN software package and allowed for the determination of Damkholer (Da), Karlovitz (Ka), and turbulent Reynolds numbers (Re_t). In

summary, flames with $0.8 < Da < 34$, $0.8 < Ka < 95$, $3 < u'/SL < 72$, and u' values ranging from 1-27 m/s were tested.

Grid length scale (hole diameter) effects on flame front characteristics were not as marked as one would have thought at the beginning of the study. There were some minor effects such as the rate of development or number of wrinkles and flamelet development and appearance. However, the driving factor for flame front characteristics was the turbulence intensity u', driven mainly by the grid blockage ratio and bulk flow rate. For all grid geometries (blockage ratios and hole diameters) and thus flow length scales L_T, the characteristics were similar at the same Reynolds number conditions with the exception of the aforementioned characteristics. Increasing Reynolds numbers affected the combustor dynamics by increasing the flow rate and the velocity fluctuations u'.

A10 kHz tunable PLIF system with an auto tracking BBO crystal was used to map the flame front characteristics with a high temporal resolution and a spatial resolution of ~100 um/pixel. The high temporal resolution enables the detection of the flame front characteristics in steps as low as 0.1 ms. OH-PLIF images revealed highly turbulent flames under the flow conditions, which were more noticeable with increasing Reynolds numbers.

In general, flame fronts exhibited pockets of burned gases in the unburned gas regions, and vice versa. These types of structures had been reported in literature for flames in the corrugated flame regime close to the border with the thin reaction zones. Some of these pockets of burned gases were interestingly developed in regions "behind" the flame front. The formation of these flamelets might be attributed to local auto ignition events of pockets of flammable gas mixtures near the flame front. 3-D effects could also be another possible explanation for these events in the sense that an out-of-plane part of a 3D flame could have come into the field of view of the camera. This has been explored in literature as a possible explanation for this behavior in lifted flames before. However, there were no suggestions of 3D effects in the data gathered, given the fact that velocity fluctuations in the y-direction were much smaller than those in the x-

direction. Without a third velocity component measurement no conclusion may be reached on this particular topic.

Burned gas pockets were seen to go through different processes including development on their own, separation form the main flame front core or branches of it, and eventual reattachment to the flame front. There was no particular correlation found between the occurrence of these events and grid characteristics or Re. Also of interest was the further breakdown of unburned pockets within the burned gas products. In general these pockets would travel downstream with the burned gases and eventually be absorbed by the surrounding burned products, however in some instances –specifically grid 3 corresponding to a BR=62% and hole dia. 1.5 mm – there was further breakdown of these pockets. This process could be attributed to local pressure fluctuations near the flame front. The source for such fluctuations could come from flame instability itself.

CH-PLIF at 5kHz was attempted by using the same dye laser used for the OH measurements. In order to be able to reach the 314nm C-X CH absorption wavelength the laser was optimized for maximum power output at 314 nm while DCM dye was used. This, to the knowledge of this author, is the first reported used of this band in an optically accessible combustor and flames with such turbulence conditions, which introduces challenges not seen when working with Bunsen burner-type of setups. 10kHz measurements at this CH band had been reported in literature with pulse energies of ~0.2 mJ/pulse. These power levels were only achieved with our current laser system at frequencies <6 kHz, which limited the time resolution to 5kHz.

The CH measurements had excessive noise, which interfered severely with the tracking of the CH layer. Given the diagonal nature of the absorption band at 314 nm, the reflection of laser sheet light in the combustor floor resulted in UV light scattering and hence the introduction of noise in the recorded signal. In addition to the light scattering, weak laser pulse energy, and hence weak CH signal, laser light flickering - which may be attributed to hardware-malfunction that was not solved prior to the experiments – introduced further complexities when post

processing the images. Given the variation in light absorbed by the intensified camera, even after a noise background subtraction it was difficult to extract the CH data. With increasing Re, which led to lower intensities in the signal it was impossible to extract useful CH data, therefore only Re=15000 flames were recorded. The CH images revealed similar trends to those seen with the OH-PLIF images, where pockets of burned gases were seen clearly for the grids with the highest turbulence intensities u' (i.e. higher blockage ratio).

Finally, the OH-PLIF images were used to determine the mean flame front surface area. This area was then used to estimate burning velocity ratios S_T/S_L using Damkholer's continuity method. Results for S_T/S_L ratios vs u'/S_L were presented. These showed that the ratio of s_T/s_L increases with increasing u'/s_L ratio. Given that u' is directly a function of bulk flow rate, velocity and grid blockage ratio, in our experiment, the increasing flame speed rate ratio can therefore be considered a function of these. Also, the general trend observed in the PLIF images was of increased wrinkling of the flame front with increasing Re, which in turn will result in larger flame surface areas. The asymptotic behavior of the data seems to fit what literature reports as curve bending.

Further investigations of flames under highly turbulent conditions are still possible. Future work related to this project would include simultaneous measurement of turbulence parameters and flame front characteristics. This would provide simultaneous turbulence data that could be related to instantaneous flame front events, providing alternative explanations to some of the events noted during the completion of this work. Refinement of the CH detection technique at 314 nm in the combustor could be done. A stronger pump power would solve the issue of the laser pulse power, yielding a stronger CH signal. The eradication of laser light intensity irregularity would also decrease the noise in CH images considerably. With a better CH signal, CH layer thickness analysis could be done at the different turbulent conditions.

References

[1] International Energy Agency, "CO2 Emissions from Fuel Consumption, (2015)

[2] N.Swaminathan, K. Bray, "Turbulent Premixed Flames," Cambridge University Press. 2011

[3] V. Sick, "High Speed Imaging in Fundamental and Applied Combustion Research, "Proceedings of the Combustion Institute 34 (3013) 3509-3530

[4] B.F. Armaly. et al,"Experimental and theoretical investigation of backward-facing step flow," J. Fluid Mech., Vol. 127 (1983): 473–496

[5] Y. S. Lee and L.C. Smith, "Analysis of power-law viscous materials using complex stream, potential and stress functions," Encyclopedia of Fluid Mechanics, Vol. 1, Flow Phenomena and Measurement (1986): 1105–1154.

[6] L. Kaiktsis, G.E. Karniadakis, and S.A. Orszag, "Unsteadiness and convective instabilities in a two- dimensional flow over a backward-facing step," J. Fluid Mech., (1996): 157–187

[7] N. Alleborn,K. Nandakumar, H. Raszillier, and F. Durst, "Further contributions on the two-dimensional flow in a sudden expansion," J. FluidMech., Issue 330 (1997): 169–188.

[8] M. Piirto et al "PIV Measurements in a Square Backward Facing Step," 15th Australian Fluid Mechanics Conference, (2004)

[9] R. W. Pitz and J. W. Daily. "Combustion in a turbulent mixing layer formed at a rearward-facing step", AIAA Journal, Vol. 21, No. 11 (1983), pp. 1565-1570

[10] J. Cohen and T. Anderson. "Experimental investigation of near-blowout instabilities in a lean, premixed step combustor", 34th Aerospace Sciences Meeting and Exhibit, Aerospace Sciences Meetings. (1996) AIAA 96-0819

[11] J. Cohen and J. Bennett, Jr.. "An experimental study of the transient flow over a backward-facing step", 34th Aerospace Sciences Meeting and Exhibit, Aerospace Sciences Meetings, (1996) AIAA 96-0322

[12] J. M. Cohen, Brian E. Wake, and Dochul Choi. "Investigation of Instabilities in a Lean, Premixed Step Combustor", Journal of Propulsion and Power, Vol. 19, No. 1 (2003), pp. 81-88

[13] V. Savelnikov et al, "Thermo-Acoustic Instabilities in a Backward-Facing Step Stabilized Lean-Premixed Flame in High Turbulence Flow," 14th Int. Symp. On Applications of Laser Techniques to Fluid Mechanics, (2008)

[14] S.B. Pope "Turbulent Flow," Cambridge University Press. 2000

[15] F. M. Mahallawy, "Fundamentals and Technology of Combustion," Elsevier. 2002

[16] S. R. Turns, "An Introduction to Combustion – Concepts and Applications," 2nd Edition. McGraw-Hill. (2000)

[17] R. M. Fristorm, "Flame structure and Process," Oxford University Press, New York, 1995

[18] P. Siewert, "Flame Front Characteristics of Turbulent Lean Premixed Methane/Air Flames at High pressure," (2006)

[19] C. K. Law, “A Compilation of Experimental Data on Laminar Burning Velocities, “ Reduced Kinetic Mechanisms for Applications to Combustion Systems. Springer, NY. (1993).

[20] C. M. Vagelopoulos, J. H. Frank, “An Experimental and Numerical Study on the Adequacy of CH as a Flame Maker in Premixed Methane Flames,” Proceedings of the Combustion Institute. (2005)

[21] R. Borghi, “On the structure and Morphology of Turbulent Premixed Flames.” Recent Advances in Aeronautical Science. 1985: Plenum Press, New York.

[22] N. Peters, “The turbulent burning velocity for small-scale and large-scale turbulence.” Journal of Fluid Mechanics, (1999) pp. 107-132.

[23] V. L. Zimont, “Theory of turbulent combustion of a homogeneous fuel mixture at high reynolds numbers,” Combustion, Explosion, and Shockwaves. Volume 15 (1979) pp. 305-311

[24] R. Sankaran et al. “Structure of a spatially developing turbulent lean methane–air Bunsen flame,” Proceedings of the Combustion Institute Volumel 31 (2007) pp. 1291- 1298

[25] F. T. Yuen, O. L. Gulder. “Premixed turbulent flame front structure investigation by Rayleigh scattering in the thin reaction zone regime,” Proceedings of the Combustion Institute. Volume 32 (2009) pp. 1747-1754

[26] P Tamadonfar, O. L. Gulder. “Experimental investigation of the inner structure of premixed turbulent methane/air flmes in the thin reaction zones regime.” Combustion and Flame Volume 162 (2015) pp. 115-128

[27] L.P.H. de Goey et al. “Analysis of the flame thickness of turbulent flamelets in the thin reaction zones regime,” Proceedings of the Combustion Institute Volume 30 (2005) pp. 859-866.

[28] B. Bohm et al. “New Perspectives on Turbulent Combustion: Multi-Parameter High-Speed Planar Laser Diagnostics,” Flow Turbulence and Combustion. Volume 86 (2011) pp. 313-341

[29] B. Thurow et al. “Review of ultra-high repetition rate laser diagnostics for fluid dynamic measurements,” Measurement Science and Technology. Volume 24 (2013).

[30] M. Raffel et al. “Particle image velocimetry: A Practical Guide,” Springer, (1998)

[31] G. Laufer, “Introduction to Optics and Lasers in Engineering,” Cambridge University Press. New York (1996)

[32] M. J. Dyer and D. R. Crosley, "Two-dimensional imaging of OH laser-induced fluorescence in a flame," Opt. Lett. 7, 382-384 (1982)

[33] M. L. Luca, E. Cantu et al. "OH PLIF Visualization of a Premixed Ethylene-fueled Dual-Mode Scramjet Combustor", 54th AIAA Aerospace Sciences Meeting, AIAA SciTech Forum, (AIAA 2016-1763)

[34] R. Wellander, M. Richter, M. Aldén. “Time-resolved (kHz) 3D imaging of OH PLIF in a flame,” Experiments in Fluids (2014) 55: 1764

[35] M. Zhang et al, “ Estimation of 3D flame surface density and global fuel consumption rate from 2D PLIF images of turbulent premixed flame,” Combustion and Flame (2015) pp. 2087-2097

[36] M. Tanahashi, S. Murakami, G. M. Choi, “Simultaneous CH-OH PLIF and stereoscopic PIV measurements of turbulent premixed flames.” Proceedings of the Combustion Institute. Vol 30 (2005) pp. 1665-1672

[37] C. Carter, J. Donbar, J. Driscoll. “Simultaneous CH planar laser-induced fluorescence and particle imaging velocimetry in turbulent nonpremixed flames,” Appl Phys B (1998) 66: 129

[38] Z. S. Li, J. Zetterberg, “Applications of a single-longitudinal-mode alexandrite laser for diagnostics of parameters of combustion interest,” Review of Scientific Instruments (2004)

[39] Z.S. Li, J. Kiefer et al., “Development of improved PLIF CH detection using an Alexandrite laser for single-shot investigation of turbulent and lean flames,” Proceedings of the Combustion Institute 31 (2007) pp. 727–735.

[40] N. Jiang, R.A. Patton, W.R. Lempert, J.A. Sutton, “Development of high-repetition rate CH PLIF imaging in turbulent nonpremixed flames,” Proceedings of the Combustion Institute 33 (2011)pp. 767–774.

[41] J.D. Miller, S.R. Engel, J.W. Tröger, T.R. Meyer, T. Seeger, “A. Leipertz, Characterization of a CH planar laser-induced fluorescence imaging system using a kHz-rate multimode-pumped optical parametric oscillator,” Appl. Opt 51 (2012) pp. 2589–2600.

[42]A. Johchi, Y. Naka, M. Shimura, M. Tanahashi, T. Miyauchi, “Investigation on rapid consumption of fine scale unburned mixture islands in turbulent flame via 10 kHz simultaneous CH–OH PLIF and SPIV,” Proc. Combust. Inst 35 (2015) pp. 3663–3671

[43] C.D. Carter, S. Hammack, T. Lee, “High-speed planar laser-induced fluorescence of the CH radical using the C2 +–X2 (0,0) band,” Appl. Phys. B 116 (2014) pp.515–519.

[44] C. D. Carter, S. Hammack, T. Lee, “High-speed flame front imaging in premixed turbulent flames using planar laser-induced fluorescence of the CH C-X band,” Combustion and Flame 168 (2016) pp. 66-74

[45] C. E. Moore, H. P. Broida,”CH in the Solar Spectrum,” Journal of Research of the National Bureau of Standards - A. Physics and Chemistry Vol. 63A (1959)

[46] M.S. Chou, A. M. Dean, “Excimer laser perturbations of methane flames: High temperature reactions of OH and CH,” The Journal of Chemical Kinetics (1985) pp. 1103-1118

[47] M. Tsujishita et al. “Visualization of the CH Molecule by Exciting $C^2\Sigma^+(v=1)$ State in Turbulent Flames by Planar Laser-Induced Fluorescence,” Japanes Journal of Applied Physics (1993)

[48] J. Jeffries, R. Copeland et al. “Multiple Species Laser-Induced Fluorescence in Flames,” The Combustion Institute (1986) pp. 1709-1718

[49] M. Tanahashi, S. Murakami, G. M. Choi, "Simultaneous CH-OH PLIF and stereoscopic PIV measurements of turbulent premixed flames." Proceedings of the Combustion Institute. Vol 30 (2005) pp. 1665-1672

[50] M. Tanahashi, T. Ueda et al. "Simultaneous dual-plane CH PLIF, single-plane OH PLIF and dual-plane stereoscopic PIV measurements in methane-air turbulent premixed flames," Proceedings of the Combustion Institute Vol. 33 (2011) pp. 775-782

[51] S. Filatyev, M. Thariyan, R. Lucht, J. Gore "Simultaneous SPIV and double pulsed PLIF of turbulent premixed flames," (2007)

[52] J. Sjoholm, J. Rosell, et al. "Simultaneous visualization of OH, CH, CH2O and toluene PIF in a methane jet flame with varying degrees of turbulence" (2013)

[53] I.Boxx, C. Slabaugh, P. Kute, R.P. Lucht, W. Meier, "3 kHz PIV/OH-PLIF measurements in a gas turbine combustor at elevated pressure" (2014)

[54] C.D. Slabaugh et al. "Simultaneous 5kHz OH-PLIF/PIV for the study of turbulent combustion engine conditions," Applied Physics B Volume 118 (2015) pp.109-130

[55] A.M. Elbaz, W.L. Roberts, "Experimental study of the inverse diffusion flame using high repetition rate OH/acetone PLIF and PIV" (2016)

[56[A. Hossain, Design of a High Intensity Turbulent Combustion System," University of Texas at El Paso (2015)

[57] M. Quiroz, "Fluid Flow Characterization Of High Turbulent Intensity Compressible Flow Using Particle Image Velocimetry." University of Texas at El Paso (2015)

[58] I.G. Shepherd, R. K. Cheng, "The Burning Rate of Premixed Flames in Moderate and Intense Turbulence," Combustion and Flame VOl 127. (2001) pp. 2066-2075

[59] J. Driscoll, "Turbulent premixed combustion: Flamelet structure and its effect on turbulent burning velocities," Progress in Energy and Combustion Science Volume 34 (2008) pp. 91–134

[60] Kobayashi Burning velocity correlation of methane/air turbulent premixed flames at high pressure and high temperature]

[61] N. Peters, "Turbulent Combustion," Cambridge University Press. 2000

Vita

Arturo Acosta was born and raised in El Paso, Texas. He attended the University of Texas at El Paso starting the Fall 2008 semester and graduated with a Bachelor of Science degree in Mechanical Engineering in May 2011. He then completed his Master's degree in Mechanical Engineering at UTEP in December 2012. His research interests are in propulsion and combustion technologies. He looks forward to apply his acquired skills and continue his professional development in industry.

Contact Information: aacosta29@miners.utep.edu

This thesis/dissertation was typed by Arturo Acosta.